

Shun Hing Institute of  
Advanced Engineering  
信興高等工程研究所



**Report and Research Highlights**  
2015 - 2017

**July 2017**

香 港 中 文 大 學  
The Chinese University of Hong Kong



蒙民偉工程學大樓

William M. W. Mong  
Engineering Building

# Contents

---

信興高等工程研究所  
Shun Hing Institute of Advanced Engineering

<b>INTRODUCTION OF SHIAE</b> .....	<b>4</b>
<b>ORGANIZATION</b> .....	<b>6</b>
<b>COMPOSITION OF INTERNATIONAL ADVISORY BOARD</b> .....	<b>7</b>
<b>COMPOSITION OF MANAGEMENT COMMITTEE</b> .....	<b>9</b>
<b>SHUN HING VISITING SCHOLARS/ FELLOWS</b> .....	<b>10</b>
<b>FINANCIAL STATUS OF SHIAE</b> .....	<b>11</b>
<b>RESEARCH</b> .....	<b>13</b>
<i>OUTSTANDING RESEARCH HIGHLIGHTS</i> .....	13
<i>ACADEMIC PUBLICATIONS</i> .....	13
<i>RENEWABLE ENERGY TRACK</i> .....	15
<i>Research Reports</i> .....	15
<i>BIOMEDICAL ENGINEERING TRACK</i> .....	37
<i>Research Reports</i> .....	37
<i>Multimedia Technologies Track</i> .....	113
<i>Research Reports</i> .....	113
<b>SHUN HING DISTINGUISHED LECTURE SERIES</b> .....	<b>123</b>

# Introduction of SHIAE

## Mission of SHIAE

The MISSION of the Institute is to spearhead, conduct, promote and co-ordinate research in advanced engineering. There is no end to the list of areas to be explored and the plan is to give priority to research topics that are both exciting and innovative. The Institute also aspires to transferring its research results to industry for practical application and to put across to the community at large the role of engineering as a driving force for human development through educational activities.

As a pioneering institute exploring the forefront of the engineering science, The Shun Hing Institute of Advanced Engineering will

- spearhead state-of-the-art advanced engineering research
- create and sustain synergy with world-class researchers
- develop with and transfer to industries cutting edge technologies
- promote appreciation of engineering in society through educational programmes

The Shun Hing Education and Charity Fund was founded by Dr. William Mong Man Wai with the aim of enhancing educational opportunities for the younger generations. The Fund has already sponsored numerous educational and research programmes in Hong Kong, the Mainland, and overseas educational institutions. Himself an engineer and a firm believer in advancing the quality of life through the development of science and technology, Dr. Mong had been there to support the establishment and growth of this Institute from the beginning.

## Centre of Excellence at CUHK

The Chinese University of Hong Kong is an internationally renowned institution of higher learning devoted to quality teaching and both academic and applied research. The University has established 29 research institutes and a number of research centres with a view to pursuing up-front research endeavours with focused goals and objectives. The Shun Hing Institute of Advanced Engineering plays a crucial part in the research infrastructure of the Chinese University which is committed to exciting research programmes in advanced engineering areas.

As a strategic centre of excellence at The Chinese University of Hong Kong, the Institute supports greater regional and international research collaborations, and strives to attract talent from the world over to achieve greater internationalization, a vision strongly advocated by every member of the University.

## Commitment of the Faculty of Engineering

The Faculty of Engineering was founded in 1991 and was built upon existing strengths with added talent from all over the world. The Faculty has been able to attract some of the best minds. Many received their training in leading universities in North America, Great Britain and Australia. Most of them have extensive experience in industry and many are leaders in their fields. This team of top-notch talent is gathered to nurture local talent through educational programmes, and break new frontiers in research through innovative and exciting research endeavours.

The positioning of The Shun Hing Institute of Advanced Engineering in the William M.W. Mong Engineering Building is deliberate as a key nucleating point to integrate research endeavours in the Engineering Faculty and its neighbours. Our members join hands with their counterparts from the Faculties of Science and Medicine in many interesting research collaborations. It is the ambitious goal of the Faculty of Engineering that the Institute should become a lighthouse for the local technology landscape to herald the migration towards high value-added technology and an information economy.

The mission of the Institute is to spearhead, conduct, promote and co-ordinate research in advanced engineering. There is no end to the list of areas to be explored and the plan is to give priority to research topics that are both exciting and innovative. The Institute also aspires to transferring its research results to industry for practical application and to put across to the community at large the role of engineering as a driving force for human development through educational activities.

## Building on Strength and The Way Ahead

Many of the Institute's research projects are built upon areas in which the Faculty has already achieved outstanding performance. These are areas that have great potential for further technological advancement and in line with industrial development in Hong Kong. The Institute provides a vibrant R&D environment to spur new discoveries and speed up their translation into applications. Since 2012, we have expanded our scope to cover new frontiers in Renewable Energy striving to answer tomorrow's energy challenges. This year, we further expand the research scope in Multimedia Technologies to include AI , big data, as top tier of Media Technology.

## Technology Transfer

Synergy with industry is the ultimate goal of research and development in Hong Kong. External experts have been brought in to the Institute to lead research projects that could benefit the industrial sector.

The technology transfer arm of the Faculty of Engineering plays an important role in the traffic between the Institute and industry. The Institute houses an array of top-notch research and development activities encompassing contract research, spin-off companies, and consultancies.

## Contribution to Society

The Institute has been making contributions to the progress of Hong Kong through a wide range of educational activities like training courses, seminars, symposiums which disseminate the latest technologies to promote appreciation of engineering in society and arouse interest of the younger generations in engineering.

# Organization of SHIAE

**International Advisory Board**

**SHIAE Management Committee**

**Multimedia  
Technologies  
Research  
(MMT)**

– since 2005 –

**Biomedical  
Engineering  
Research  
(BME)**

– since 2005 –

**Renewable  
Energy  
Research  
(RNE)**

– since 2012 –

We also provide support and sponsorship to the Faculty of Engineering in organizing prestigious academic conference in Hong Kong so as to raise our international profile.

# Composition of International Advisory Board

(with effect from August 1, 2016)

Chairman:

**Dr. David T.Y. MONG** 蒙德揚先生

*Chairman & Group CEO  
Shun Hing Electronic Holdings Limited  
Hong Kong*



Members:

**Professor Victor ZUE**

*Delta Electronics Professor of Electrical Engineering and Computer  
Science  
Massachusetts Institute of Technology  
U.S.A*



**Dr. Harry SHUM** 沈向洋博士

*Executive Vice President, Technology and Research  
Microsoft Corporation  
U.S.A.*



**Professor Yongmin KIM**

*Affiliate Professor  
University of Washington  
U.S.A.*



**Professor Chih-Ming HO** 何志明教授

*Ben Rich-Lockheed Martin Professor in School of Engineering  
University of California, Los Angeles  
U.S.A.  
(until July 2016)*



**Professor C.C. Jay KUO**

*Professor of Electrical Engineering and Computer Science  
University of Southern California  
U.S.A.*



**Professor Paul, Kit-lai YU**

*Provost, Revelle College, Jacobs School of Engineering  
University of California, San Diego  
U.S.A.*



**Professor Tai Fai FOK 霍泰輝教授**

*Pro-Vice-Chancellor  
The Chinese University of Hong Kong  
Hong Kong*



**Professor Wing-shing WONG 黃永成教授**

*Choh-Ming Li Professor of Information Engineering  
The Chinese University of Hong Kong  
Hong Kong*



**Professor Ching Ping WONG 汪正平教授**

*Dean of Engineering  
The Chinese University of Hong Kong  
Hong Kong*



**Professor Pak Chung CHING 程伯中教授**

*Director of Shun Hing Institute of Advanced Engineering  
Choh-Ming Li Professor of Electronic Engineering  
The Chinese University of Hong Kong  
Hong Kong*



# Composition of Management Committee

*(with effect from August 1, 2017)*

Chairman: **Professor Pak Chung CHING** (*ex-officio*)  
*Director of SHIAE, and Choh-Ming Li Professor of Electronic Engineering*

Members: **Professor Ching Ping WONG** (*ex-officio*)  
*Dean of Faculty of Engineering*

**Mr. Terrence CHAN**  
*Managing Director of Shun Hing Electronic Holdings, Limited  
Hong Kong*

**Professor Jianwei HUANG**  
*Department of Information Engineering*

**Professor Tan LEE**  
*Department of Electronic Engineering*

**Professor Wei-Hsin LIAO**  
*Department of Mechanical and Automation Engineering*

**Professor Dennis Y.M. LO**  
*Department of Chemical Pathology*

**Professor Anthony Man-cho SO**  
*Department of Systems Engineering & Engineering Management*

**Professor Raymond Kai-yu TONG**  
*Department of Biomedical Engineering*

**Professor Kwong-sak LEUNG**  
*Department of Computer Science and Engineering*  
*(until July 2017)*

**Professor Helen M.L. MENG**  
*Chairman, Department of Systems Engineering & Engineering Management*  
*(until July 2017)*

**Professor Max Qing Hu MENG**  
*Chairman, Department of Electronic Engineering*  
*(until July 2017)*

**Professor Wing-shing WONG**  
*Choh-Ming Li Professor of Information Engineering*  
*(until July 2017)*

Member and Secretary: **Professor John C.S. LUI**  
*Choh-Ming Li Professor of Computer Science and Engineering*

## Shun Hing Visiting Scholars/ Fellows

The Institute has launched a Shun Hing Distinguished Scholar Program with an aim to attract distinguished scholars to pursue research collaboration with our faculty and to strengthen our research profile. The following scholars visited to work either on a short term or on a longer term engagement with the Institute between 2015 and 2017.

### **Shun Hing Fellows and Research Associate:**

*(in alphabetical order)*

<b>Dr. ABBASNEJAD Ghasem</b> <i>National Univesrity of Singapore</i>	2016 - 2017
<b>Dr CHEN Zhong</b> <i>The Sun Yat-sen University, China</i>	2014 - 2016
<b>Dr. GU Chenglin</b> <i>Tian Jin University, China</i>	2016
<b>Dr. LEE Chinghuan</b> <i>National Chung Kung Univesrity, Taiwan</i>	2016 - 2018
<b>Dr LI Jinming</b> <i>Nanyang Technological University, Singapore</i>	2014 - 2016
<b>Dr. LOU Yishan</b> <i>The Chinese University of Hong Kong</i>	2015
<b>Dr SHANG Fanhua</b> <i>The Chinese University of Hong Kong</i>	2015
<b>Dr. WALKER Steven L.</b> <i>Johns Hopkins School of Medicine, Baltimore, USA</i>	2014 - 2015
<b>Dr WEI Kongchang</b> <i>The Chinese University of Hong Kong</i>	2014 - 2016
<b>Dr. XU Jianbin</b> <i>Nankai University, China</i>	2015 - 2016
<b>Dr. ZHANG Jing</b> <i>The University of Hong Kong</i>	2015 - 2016
<b>Mr. Satwinder Singh SAINI</b> <i>Indian Institute of Technology, Chandigarh, India</i>	2016 - 2017

# Financial Status of SHIAE

As at 30 June 2017  
HK\$

## INCOME

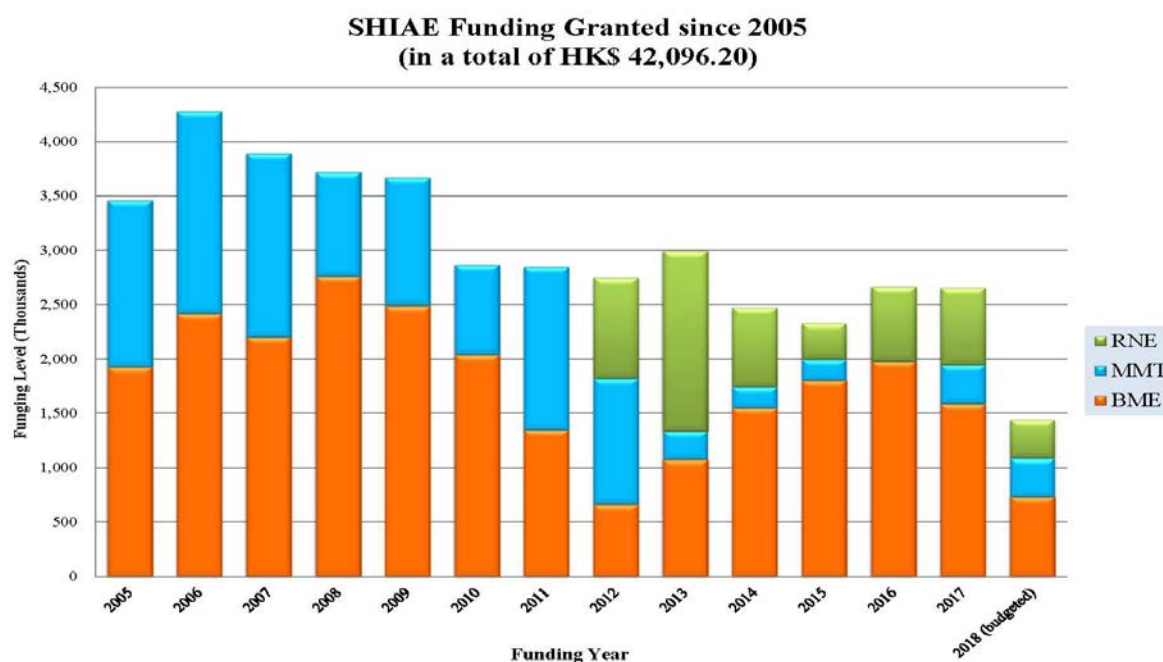
Start Up Seed Fund	34,500,000
New Funding patched in Dec 2016	10,000,000
Interest and investment income	7,006,559
Sub-total:	51,506,559

## EXPENDITURE

Research funding granted since 2005-2017	(1)	40,649,200
Committed Research Budget in 2018	(2)	1,447,000
Unspent remaining fund from all completed projects		-3,078,436
Committed staff cost		790,898
Operating cost		4,499,379
Sub-total:		44,308,041

**BALANCE as at 30 June 2017** **7,198,518**

## (1) Annualized Research Funding to each research areas granted since 2005



This figure shows the distribution of the SHIAE funding granted to each track of research projects, namely Biomedical Engineering (BME), Multimedia Technology (MMT) and Renewable Energy (RNE) annually.

(2) Detail funding level on each batch of projects (in HK\$ '000)

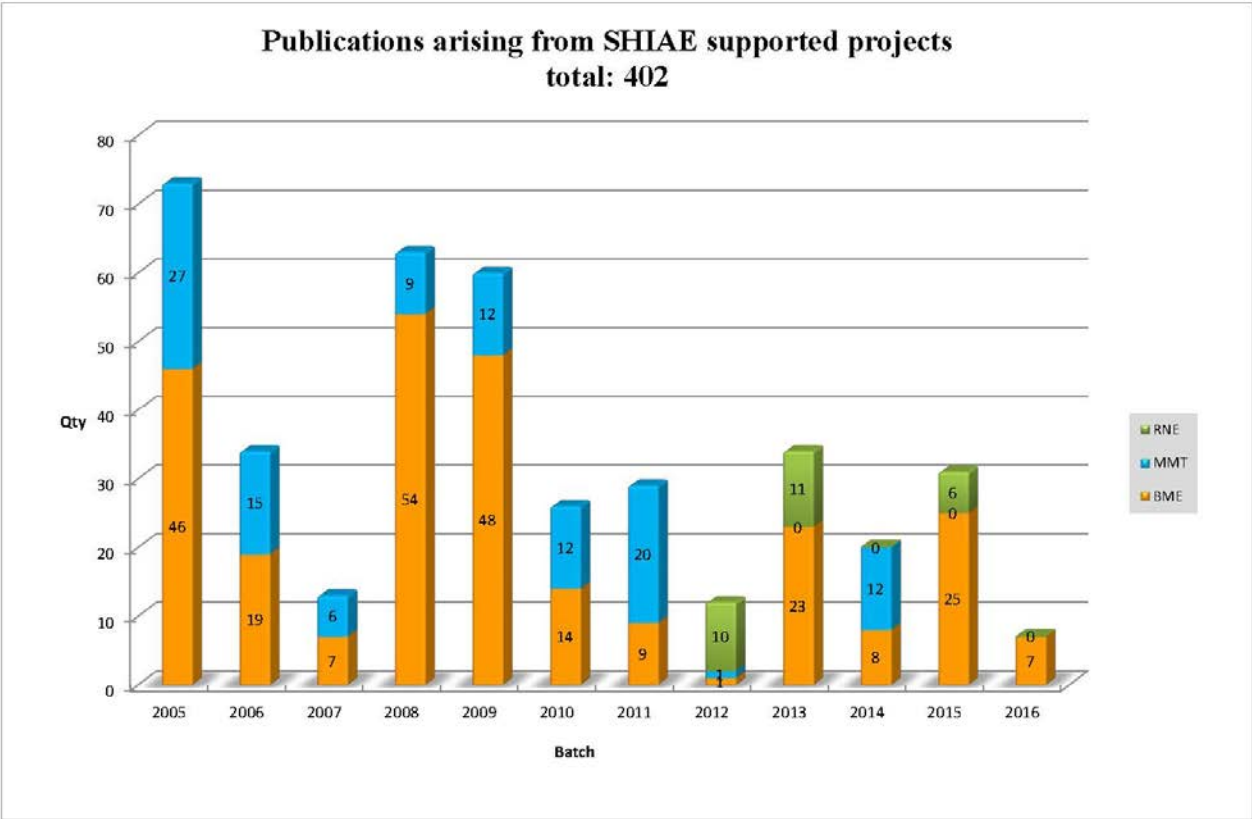
Funding Year/ No. of projects	<u>2018</u> (budgeted)	<u>2017</u>	<u>2016</u>	<u>2015</u>	<u>2014</u>	<u>2013</u>	<u>2012</u>	<u>2011</u>	<u>2010</u>	<u>2009</u>	<u>2008</u>	<u>2005 to 2007</u>
Year 2007 Batch (7 Projects)	-	-	-	-	-	-	-	-	-	200	1,792	11,637
Year 2008 Batch (4 Projects)	-	-	-	-	-	-	-	-	-	1,848	1,928	-
Year 2009 Batch (5 Projects)	-	-	-	-	-	-	-	268	1,414	1,624	-	-
Year 2010 Batch (5 Projects)	-	-	-	-	-	-	-	1,334.6	1454.6	-	-	-
Year 2011 Batch (4 Projects)	-	-	-	-	-	-	1,228	1,248	-	-	-	-
Year 2012 Batch (5 Projects)	-	-	-	-	-	1,520	1,520	-	-	-	-	-
Year 2013 Batch (4 Projects)	-	-	-	-	1,474	1,474	-	-	-	-	-	-
Year 2014 Batch (3 Projects)	-	-	-	1,002	1,002	-	-	-	-	-	-	-
Year 2015 Batch (4 Projects)	-	-	1,328	1,328	-	-	-	-	-	-	-	-
Year 2016 Batch (4 Projects)	-	1,213	1,340	-	-	-	-	-	-	-	-	-
Year 2017 Batch (4 Projects)	1,447	1,447	-	-	-	-	-	-	-	-	-	-
WOSP2007 Workshop	-	-	-	-	-	-	-	-	-	-	-	25
Annualized total:	1,447	2,660	2,668	2,330	2,476	2,994	2,748	2,850.6	2,868.6	3,672	3,720	11,662
<b>Accumulated Total</b>	<b>HK\$42,096.20</b>											

This table shows the detail amount of SHIAE funding granted to each batch of research projects. The subtotal amount of **1.447 million** budgeted for 2018 is committed to support research projects in July 2018.

# Research - Outstanding Research Highlights

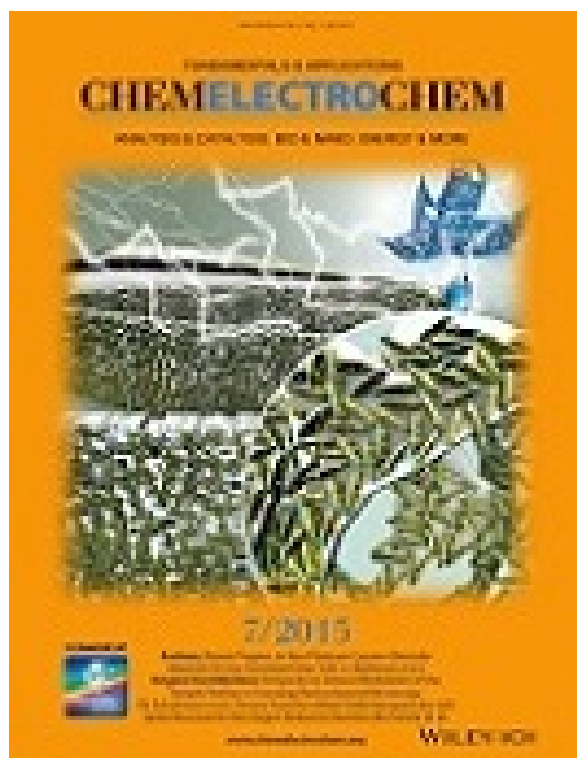
## Academic Publications

So far **48 projects** have been successfully completed and **402 articles** arising from the results of these research projects have been published in international conference proceedings and journals. The other **12 on-going projects** are also progressing well with encouraging results produced. All publications generated by each individual projects are kept in the archive of SHIAE office. The chart below shows the number of academic publications produced each year.

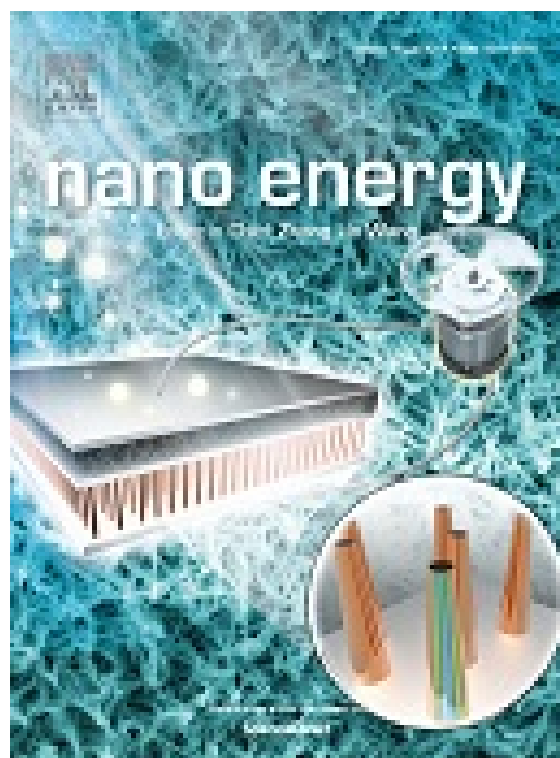


The list of publications can also be downloaded from the webpage of SHIAE at [www.shiae.cuhk.edu.hk/research.htm](http://www.shiae.cuhk.edu.hk/research.htm)

### Journal cover highlights



J[3]



J[5]

## *Renewable Energy Track*

# Research Reports In Renewable Energy

### **Newly Funded Projects**

(2017-2019)

\* Tunable spindle using self-excited vibration for high efficiency renewable electric generators

### **Continuing Projects**

(2016-2018)

\* Robust NiMo–yttria stabilized zirconia (NiMo–YSZ) anode materials for solid oxide fuel cells

(2015-2017)

\* Experimental and modeling study of biodiesel combustion

### **Completed Projects**

(2013-2015)

\* Earth-Abundant Metal/Metal Oxide Nanostructures for Rechargeable Li-Air Batteries: Catalyst Design and Mechanistic Investigation

\* Graphene-based asymmetric supercapacitors with high energy density for clean energy storage systems

---

The following reports are enclosed in “Research Highlights” printed in July 2015.

**Completed Projects**

(2012) \* Vibration Energy Harvesting Utilizing Multifunctional  
Phononic Meta-Materials and Structures

**Completed Projects**

(2012) \* Understanding Electron and Phonon Transport in Boron  
Carbide Nanowires for Thermoelectric Energy Conversion

\* Ternary Hybrid Polymer/Nanocrystal Bulk Heterojunction  
Solar Cells with Cascade Energy-Level Alignmen

*(Funded Year)*

## TUNABLE SPINDLE USING SELF-EXCITED VIBRATION FOR HIGH EFFICIENCY RENEWABLE ELECTRIC GENERATORS

Principal Investigator: Professor Ping GUO  
*Department of Mechanical & Automation Engineering*  
*CUHK*



**Project Start Date: 1 July 2017**

### ABSTRACT

Considering the world population growth, diminishing of fossil fuel sources, and environmental pollution, the use of renewable resources, such as hydroelectric, nuclear, and wind energy, has been emerging as an important form of clean energy. The core functional part in these renewal energy technologies is an electric generator. One critical issue determining the efficiency and reliability of renewable electric generators lies in the interaction between the spindle shaft and bearing surfaces. The friction coefficient largely influences the power generation efficiency while the contact condition determines the wear rate of the shaft and bearings. This project proposes a novel spindle design for renewable electric generators, which utilizes high frequency vibration for improved tribological performance, higher energy efficiency, and reduced wear. The proposed design is supported by three major innovations: (1) vibration-induced friction reduction; (2) self-excited vibration without any extra power supply; and (3) a tunable spindle structure for a wide operation range. The proposed design has a high potential for commercialization due to its much improved performance without major increase in cost and design complexity. This project, if successful, will not only help the development of fundamental research but also the application of renewable electric generators.

### INNOVATION AND PRACTICAL SIGNIFICANCE:

This project proposes a novel spindle design for renewable electric generators, which utilizes high frequency vibration for improved tribological performance, higher energy efficiency, and reduced wear. The proposed design is supported by three major innovations: (1) vibration-induced friction reduction; (2) self-excited vibration without any extra power supply; and (3) a tunable spindle structure for a wide operation range. This project, if successful, will significantly improve the performance of traditional renewable electric generators in terms of efficiency and lifetime, which have play an ever increasing role in the era of clean energy.

### PROJECT OBJECTIVES:

1. Propose a low friction bearing method by the principle of vibration-induced friction reduction to prolong the lifetime of high-load bearings and increase the power efficiency in rotating-spindle-type electric generators.
2. Establish a self-tunable vibration generating device without extra electric power supply or piezoelectric elements, which reduces the extra cost for vibration system and simplifies the overall structure.
3. Realize a self-excited vibration spindle system, which is capable of changing the resonant frequency of the spindle for a better friction reduction effect when the self-excited vibration frequency is in accordance with the resonant one.

# ROBUST NICKEL-MOLYBDENUM–YTTRIA STABILIZED ZIRCONIA (NIMO–YSZ) ANODE MATERIALS FOR SOLID OXIDE FUEL CELLS

Principal Investigator: Professor Yongsheng CHEN  
*Department of Mechanical & Automation Engineering*  
*CUHK*



Research Team Members:

Dr. Chinghuan Lee (postdoctoral fellow)<sup>(1)</sup>,  
 Mr. Jiazheng Ren (graduate student)<sup>(1)</sup>

<sup>(1)</sup> Dept. of Mechanical and Automation Engineering, CUHK

**Reporting Period: 01 August 2016 – 30 April 2017**

## ABSTRACT

This proposal aims to develop new anode materials to improve durability of the state-of-the-art solid oxide fuel cells (SOFCs). SOFCs are electrochemical devices that convert chemical energy of a fuel (commonly hydrogen, more importantly, fuels derived from *renewable* sources, such as biomass and municipal wastes) and oxidant directly into electrical energy. They are energy efficient and environmentally benign, and their large scale applications in electricity production may address the environmental, climate change, and water concerns that we are facing today.

There are major technical barriers that have to be overcome before SOFCs can be commercialized and widely used for power generation. Among them is anode degradation. For the state-of-the-art Ni–YSZ anodes, carbon deposition (or coking) on and sulfur poisoning of the anode are responsible for the performance loss due to the presence of impurities in carbonaceous fuels, a price that comes with the SOFC’s fuel flexibility. These problems are usually dealt with separately. We will design new NiMo-YSZ anode materials to mitigate carbon deposition and sulfur poisoning simultaneously with the PI having several years’ experience in studying these phenomena in steam reforming reactions. If successful, this project will promote the final commercialization of SOFC technology for power generation.

## 1. OBJECTIVES AND SIGNIFICANCE

Solid oxide fuel cells (SOFC) are electrochemical devices that convert chemical energy of a fuel (commonly hydrogen) and oxidant directly into electrical energy. They are much more energy efficient and environmentally benign than conventional electric power generation processes. Their large scale applications in electricity production may one day replace the current heat engine based electric power generation and address the environmental, climate change, and water concerns that face us today.

Major parts of a SOFC include anode, cathode, and electrolyte. Anode and cathode are the places where H<sub>2</sub> oxidation and O<sub>2</sub> reduction take place while electrolyte provides a separation for the gases and a tunnel for ions (O<sup>2-</sup> or H<sup>+</sup>). Materials-wise, state of the art electrolyte, anode and cathode are yttria-stabilized zirconia (YSZ), Ni–YSZ and lanthanum strontium manganite-YSZ (LSM-YSZ) composite, respectively. Compared to other fuel cell types, one advantage of SOFCs is its fuel-flexibility. They can operate not only on hydrogen, but also on hydrocarbon fuels from various sources, for example, natural gas (CH<sub>4</sub>) and fuels derived from *renewable* sources, such as biomass and municipal wastes. This flexibility is due to the SOFC operation conditions, which dictate that SOFC is also a steam reformer and the anode serves as a *catalyst* (i.e., a functional material that promotes a chemical reaction). Inside a SOFC, hydrocarbons react with steam to produce hydrogen and carbon monoxide (termed “steam reforming”).

There are major technical barriers to be overcome before SOFCs can be commercialized and widely used for power generation. Among them is anode degradation. For Ni–YSZ anodes, degradation may fall in three categories: (1) material transport mechanism; (2) deactivation and passivation mechanism, and (3) thermo-mechanical mechanism. Deactivation and passivation mechanism is responsible for the performance loss due to the presence of impurities in carbonaceous fuels, a price that comes with SOFC's fuel flexibility. It involves carbon deposition and sulfur poisoning. This proposal aims to tackle the anode degradation by carbon deposition and sulfur poisoning, and if successful, will greatly promote the commercialization of the SCFC technology.

The project objectives include the following: (1) find the optimal composition of NiMo–YSZ anode materials for minimal degradation; (2) determine the proper formation of NiMo; (3) determine the optimal H<sub>2</sub>S content and other reaction conditions for minimal coking and sulfur poisoning; (4) perform multiple characterization techniques to determine the degradation mechanism in NiMo–YSZ anode materials.

## 2. RESEARCH METHODOLOGY

We will develop nickel-molybdenum–yttria stabilized zirconia (NiMo–YSZ) anode materials. In our design, Ni and Mo will be metal nano-particles, either in separate phases or in alloy form. The Mo oxide layers on Mo surface are active for aromatization reaction (producing benzene from CH<sub>4</sub> or CO and H<sub>2</sub>). The proposed research includes two tasks: (1) catalyst synthesis and steam reforming and (2) anode deactivation mechanisms. In other words, we will design bifunctional NiMo–YSZ catalyst, test them under reaction conditions relevant to real SOFC operation conditions, and use materials characterization techniques to study their deactivation mechanism. A catalyst testing system has been installed in Room 112 of the William M.W. Mong Engineering Building. The system is configured to carry out multiple reactions including steam reforming as shown in Figure 1. Different gases can be delivered to the system at prescribed flow rates controlled by a computer. More importantly, a controlled evaporation and mixing (CEM) device is installed to ensure stable steam delivery to the system. Gas analysis is carried out simultaneously by online IR spectrometer and gas chromatography (GC).



**Figure 1** The catalyst testing system. Left: reactor, gas manifold and steam generator; right: IR spectrometer with 2-m gas cell for gas detection and quantification.

Among a few other things, one promising development in this project is to establish a catalyst evaluation method that has the potential to revolutionize the way how scientists and engineers test steam reforming catalysts. It is well known that carbon deposition and sulfur poisoning are two major catalyst deactivation mechanisms in steam reforming. Our previous work has shown that a major contribution of sulfur poisoning is enhanced carbon deposition. However, due to technical difficulty, carbon deposition kinetics has never been measured experimentally. Moreover, the typical method for gas analysis is GC, which has two disadvantages: 1) low time resolution as GC usually samples every 20 minutes or so; and 2)

complexity in experimental setup and data analysis. Because GC columns usually cannot endure too much moisture, so the gas effluent from the reactor needs to pass through a cold trap to remove steam before being analyzed by a GC, this is a loss of important information as steam is a major reactant. Another problem is that GC measures only concentrations of different gases, however, to determine catalyst conversion and selectivity, gas flow rates leaving the reactor are needed. This is a challenge for GC-based analysis. In this project, we use a IR spectrometer to measure the concentrations of polar gases present in the effluent. By taking advantage of the intrinsic relationship between flow rates and concentrations and the general mass balance, we are developing a method to measure the flow rates of major reactants and products including H<sub>2</sub>O and H<sub>2</sub> as well as carbon deposition rate. The data sampling rate is 12 sec/point. Thus, this new method is going to make a breakthrough in steam reforming catalyst evaluation, a manuscript on this topic is in preparation.

Experimental parameters are chosen to reflect real reaction conditions relevant to SOFC operation. The steam-to-carbon ratios in the feed will be between 1~2.5 and the temperature is set at 800 °C; Some N<sub>2</sub> is co-fed to dilute the reactants achieving high conversion rate of CH<sub>4</sub>. Three NiO catalysts will be prepared by oxidation of commercially available Ni nano-powders with average sizes of 20, 40 and 50 nm. The oxidized temperatures of Ni will be 600~1000 °C for pre-sintering and forming solid solutions with YSZ. Two nanosized Molybdenum sources have been ordered. They are 1) metal Mo with a particle size of 40 nm and 2) MoO<sub>3</sub> with a particle size of 13-80 nm. The raw materials will be mechanically mixed by planetary ball milling technique. The atomic ratios of Ni/Mo will be fixed among the different sources. The powder mixtures for catalyst tests will be prepared in the Ni/Mo atomic ratios of 160, 20, 10, 3, and so forth. A gas mixture of 10 ppm H<sub>2</sub>S balanced by CH<sub>4</sub> will be used to conduct sulfur poisoning tests. Various materials characterization techniques will be used to study anode deactivation mechanism.

### 3. RESULTS ACHIEVED SO FAR

#### a. Modeling of SMR reactions:

$$\text{The total inlet molar flow rate: } F_i = F_{i,CH_4} + F_{i,H_2O} + F_{N_2}, \quad (1)$$

where  $F_{i,CH_4}$ ,  $F_{i,H_2O}$  and  $F_{N_2}$  stand for the inlet flow rates of CH<sub>4</sub>, H<sub>2</sub>O and N<sub>2</sub>, respectively. It is well recognized that there are four major chemical reactions under the reaction conditions: SMR, water gas shift reaction (WGS), methane decomposition (MD) and Boudouard reaction (BR).

The chemical reaction rates of SMR, RWGS, MD and BR are defined as the molar consumption rates of CH<sub>4</sub>, CO, CH<sub>4</sub> and the molar generation rate of CO<sub>2</sub>, respectively. Based on the stoichiometry of the four chemical reactions, the total molar flow rate of the effluents is:

$$F_o = F_i + 2F_{SMR} + F_{MD} - F_{BR}, \quad (2)$$

where  $F_{DRM}$ ,  $F_{MD}$  and  $F_{BR}$  stand for the chemical reaction rates of SMR, MD and BR, respectively. Based on the stoichiometric relationships, after the reactions, the molar flow rates of CH<sub>4</sub>, H<sub>2</sub>O, CO<sub>2</sub>, and CO in the effluents are:

$$F_{o,CH_4} = F_{i,CH_4} - F_{SMR} - F_{MD} \quad (3)$$

$$F_{o,H_2O} = F_{i,H_2O} - F_{SMR} - F_{WGS} \quad (4)$$

$$F_{o,CO_2} = F_{WGS} + F_{BR} \quad (5)$$

$$F_{o,CO} = F_{SMR} - F_{WGS} - 2F_{BR}, \quad (6)$$

where  $F_{o,CH_4}$ ,  $F_{o,H_2O}$ ,  $F_{o,CO_2}$  and  $F_{o,CO}$  are the outlet molar flow rates of CH<sub>4</sub>, H<sub>2</sub>O, CO<sub>2</sub> and CO, and  $F_{WGS}$ , the chemical reaction rate of WGS. After reactions, the molar concentrations of CH<sub>4</sub>, CO<sub>2</sub>, CO, and H<sub>2</sub>O in the outlet were analyzed by FTIR. Basically, the concentrations of these components can be expressed:

$$C_{CH_4} = (F_{o,CH_4}) / F_o \quad (7)$$

$$C_{H_2O} = (F_{o,H_2O}) / F_o \quad (8)$$

$$C_{CO_2} = (F_{o,CO_2}) / F_o \quad (9)$$

$$C_{CO} = (F_{o,CO}) / F_o \quad (10)$$

Substituting Equations 1 - 6 for these related factors in Equations (7), (8), (9) and (10), the four equations above form a linear nonhomogeneous equation set in which  $F_{SRM}$ ,  $F_{WGS}$ ,  $F_{MD}$  and  $F_{BR}$  are the unknowns:

$$(2C_{CH_4} + 1) * F_{SRM} + (C_{CH_4} + 1) * F_{MD} - C_{CH_4} * F_{BR} = (1 - C_{CH_4})F_{i,CH_4} - C_{CH_4} * (F_{i,H_2O} + F_{N_2})$$

$$(2C_{H_2O} + 1) * F_{SRM} + F_{WGS} + C_{H_2O} * F_{MD} - C_{H_2O} * F_{BR} = (1 - C_{H_2O}) * F_{i,H_2O} - C_{H_2O} * (F_{i,CH_4} + F_{i,N_2})$$

$$2C_{CO_2} * F_{SRM} - F_{WGS} + C_{CO_2} * F_{MD} - (C_{CO_2} + 1) * F_{BR} = -(F_{i,CH_4} + F_{i,H_2O} + F_{i,N_2})$$

$$(2C_{CO}-1) * F_{SRM} + F_{WGS} + C_{CO} * F_{MD} + (2 - C_{CO}) * F_{BR} = -(F_{i,CH_4} + F_{i,CO_2} + F_{i,N_2}) * C_{CO}$$

Solving these equations, the important flow rates related to the reaction are obtained in terms of concentrations measurable by IR. For example, the production rate of H<sub>2</sub>, which is  $3 * F_{SRM} + F_{WGS} + 2 * F_{MD}$ , and the carbon formation rate,  $F_{MD} + F_{BR}$ , can be expressed in  $C_{CH_4}$ ,  $C_{H_2O}$ ,  $C_{CO_2}$ , and  $C_{CO}$ .

b. Initial experimental test of the SMR modelling: A 10% Ni supported on  $\gamma$ -Al<sub>2</sub>O<sub>3</sub> (Ni/Al<sub>2</sub>O<sub>3</sub>) was prepared by impregnation method and is used as a reference. During 10 hours of reaction under different steam carbon ratio, the concentrations of the major reactants and productions, CH<sub>4</sub>, H<sub>2</sub>O, CO, and CO<sub>2</sub> were measured by IR and are shown in Fig. 2. There are three stages in the process as detailed in the caption.

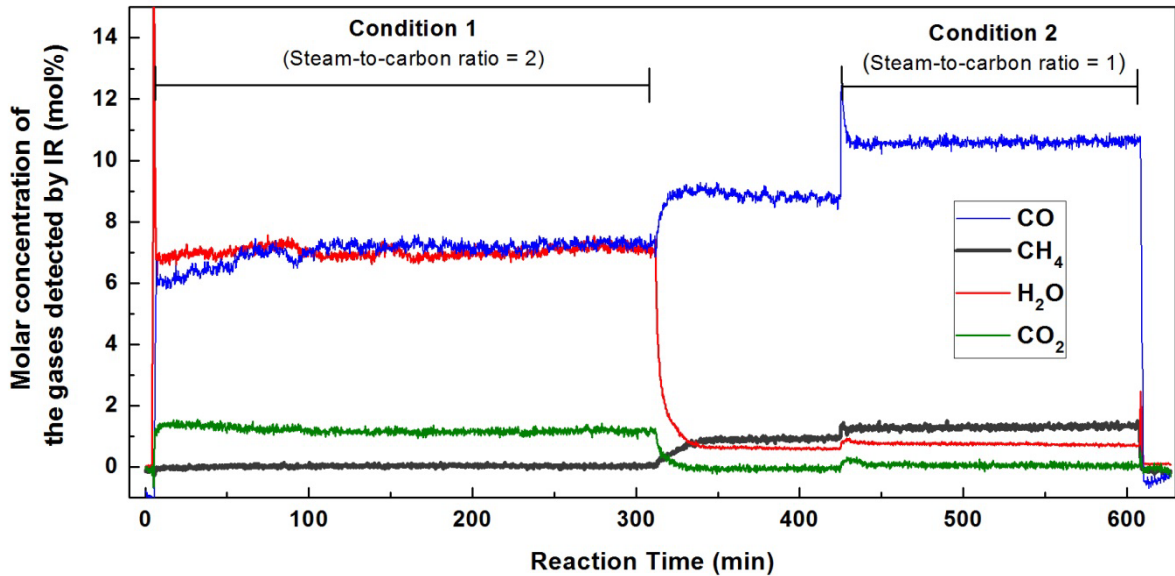
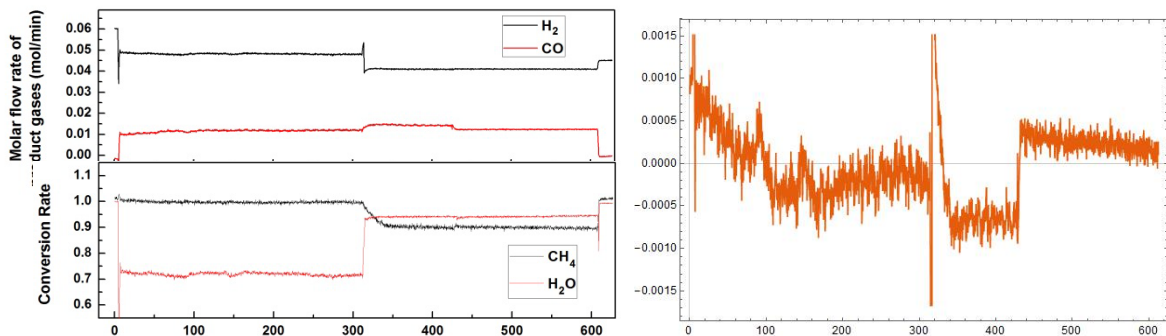


**Figure 2** Molar concentrations of the important effluent gases as a function of reaction time during SMR operations measured by IR spectrometer. Note that between 0 – 430 minutes, the effluent is diluted by extra N<sub>2</sub> gas.

By applying the method developed previously, the H<sub>2</sub> and CO production rates are determined as shown in Fig. 3. Both production rates are stable during the test. Changes are observed when the steam to carbon ratio (S/C ratio) changes from 2 to 1 resulting in lower H<sub>2</sub> and a little bit higher CO production rates. Also shown in Fig. 3 are the CH<sub>4</sub> and H<sub>2</sub>O conversion rates. At 2:1 S/C ratio, CH<sub>4</sub> is completely converted while at 1:1 S/C ratio the CH<sub>4</sub> conversion rate is lower at about 90%. Contrary to the featureless profiles of the conversion rates and H<sub>2</sub> and CO production rates, the carbon deposition rate is really dynamic. It is believed that some of the features are artifacts due to current experimental errors which can be significantly minimized upon optimization; nevertheless, it may mark the start of a new era



when we can experimentally observed carbon deposition kinetics in real time.

**Figure 3** Catalytic performance of a 10%Ni/Al<sub>2</sub>O<sub>3</sub> catalyst in the steam reforming reactions shown in Fig. 2. Left top: H<sub>2</sub> and CO production rates; left bottom: CH<sub>4</sub> and H<sub>2</sub>O conversion rates; and right: carbon deposition rate.

#### **4. PUBLICATION AND AWARDS**

The postdoctoral researcher, Dr. Chinghuan Lee, applied for Research Fellowship Scheme 2016-17 based on this SHIAE project and received about HK\$190,000 additional funding from the Faculty of Engineering and Office of Research and Knowledge Transfer. This frees up some of the Staff costs; hopefully we can reallocate some of the funds for general expenses. So far, we have not published journal papers from the research, but we are confident that 2~3 manuscripts will be submitted in the following months.

# EXPERIMENTAL AND MODELING STUDY OF BIODIESEL COMBUSTION

---

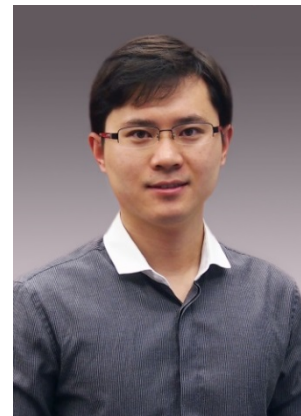
---

Principal Investigator: Professor Wei REN  
*Department of Mechanical & Automation Engineering*  
*CUHK*

Co-Investigator (if any): Enoch Dames<sup>(2)</sup>  
Research Team Members: Zhili Li<sup>(1)</sup>, Zhen Wang<sup>(1)</sup>,

<sup>(1)</sup> Dept. of Mechanical and Automation Engineering, CUHK

<sup>(2)</sup> Department of Chemical Engineering, MIT, USA



**Reporting Period: 01 July 2015 – 30 April 2016**

## ABSTRACT

Liquid fossil fuels such as gasoline, diesel, and kerosene are the most popular choices for transportation. However, the burning of fossil fuels has led to serious environmental issues of air pollution and global warming. Biofuels offer an attractive alternative to fossil fuels and can contribute significantly to sustainable development in terms of economic and environmental concerns. Biodiesel, with its numerous desirable fuel properties, is among the best candidates to replace diesel fuel in engine systems. Considerable effort is currently being devoted to the development of quantitatively predictive mechanisms for biodiesel combustion, which are required by the design of new engines and fuel blends. However, the detailed biodiesel combustion chemistry is still far from completion. This research aims to enlarge the experimental shock tube database of biodiesel surrogate and component combustion measurements. In order to accomplish this, a novel aerosol shock tube technique is designed to allow measurements of the very-low-vapor-pressure biofuels. Ignition delay times, species time-histories, and elementary reaction rate constants will be measured to understand the fundamental chemical kinetics of biodiesel surrogates. The proposed study will result in new and valuable information to improve the existing understanding of biodiesel combustion.

## 1. OBJECTIVES AND SIGNIFICANCE

- 1). *To develop and test the new method of laser diagnostics and shock tube for studying combustion chemical kinetics of biofuels with very low vapor pressure.* The large fatty acid methyl esters (FAMES) composing biodiesel have so low vapor pressures (sub-Torr) that obtaining sufficient gas-phase fuel molecules in a shock tube is virtually impossible. We propose a novel design of Laval nozzle to be used in the CUHK shock tube to generate uniform fuel aerosol, making it suitable to study biodiesel combustion. Additional laser diagnostics will be developed to detect the intermediate/product species during the combustion process. This new experimental capability can be extended for studying chemical kinetics of all types of biofuels.
- 2). *To investigate the influence of alkyl chain length and C=C bond on the combustion kinetics of small methyl esters.* Most of the previous biodiesel combustion research focused on the short-chain methyl esters containing <5 carbon atoms. Moreover, FAMES in biodiesel are mostly unsaturated containing C=C double bonds, while considerably less work has been reported on unsaturated methyl esters. We will systematically investigate the chemical kinetics of methyl esters with varied alkyl chain lengths and the existence of C=C bond in the molecular structure.
- 3). *To measure the ignition delay times, species time-histories, and elementary reaction rate constants during the oxidation of large methyl esters.* The biodiesel blends are usually composed of five FAMES with methyl oleate (MO, C<sub>19</sub>H<sub>36</sub>O<sub>2</sub>) the largest constituent. The kinetic properties of MO is not yet well-understood, and especially no experimental data for MO currently exist in the literature. With the advanced aerosol shock tube/laser diagnostics technique, our research can provide such valuable shock tube data for the validation of reduced/detailed kinetic mechanisms for biodiesel fuels.

## 2. RESEARCH METHODOLOGY

We divide the work into the following three tasks to achieve the goal of this research project.

### **Task 1: to develop the advanced shock tube/laser diagnostics for the low-vapor-pressure biofuel combustion.**

The next generation of shock tube is under-construction and will be installed in the Laser Diagnostics and Combustion Laboratory at CUHK. A novel design of Laval nozzle used in this shock tube makes it suitable to study fuels with very low-vapor-pressure (sub-Torr) such as the real biodiesel. In the current work, the fuel aerosol/gas mixtures being studied undergo two subsequent shock heatings and compressions. First the incident shock (500-800 K) can evaporate any distillate liquid fuel. A visible laser at 665 nm will be used to check the complete vaporization of all fuel droplets before the arrival of the reflected shock wave by monitoring the droplet-induced laser extinction. Then the reflected shock will bring the purely gas-phase mixtures to combustion-relevant temperatures (1000-2000 K) where the chemistry can be observed. The large inner dimension of our shock tube (ID: 12 cm) ensures negligible non-ideal effects caused by the boundary layer.

Fuel chemistry and chemical kinetics are then studied in the shock tube with the aid of advanced laser diagnostics and pressure sensors. Laser-absorption diagnostics are widely used for shock tube chemical kinetics studies, due to their species-specific and non-intrusive properties with fast time response (microsecond). Commercial quantum cascade lasers (QCLs) at the wavelengths of 4.3  $\mu\text{m}$ , and 4.6  $\mu\text{m}$ , and 5.2  $\mu\text{m}$  will be used for the sensitive detection of CO, CO<sub>2</sub> and NO. Interband cascade lasers (ICLs) at 2.5  $\mu\text{m}$  and 3.6  $\mu\text{m}$  will be implemented for H<sub>2</sub>O and CH<sub>2</sub>O diagnostics. These absorption sensors will be integrated with the shock tube via five optical windows to achieve simultaneous multi-species detection.

### **Task 2: to understand the combustion chemical kinetics of biodiesel surrogates.**

Chemical kinetic mechanisms are developed and validated using a combination of complex computer-aided computations and experimental data obtained under carefully controlled conditions. These mechanisms are built to understand the precise reaction pathways undertaken during fuel oxidation that transform fuel into CO<sub>2</sub> and H<sub>2</sub>O while producing heat. We start the biodiesel study with its surrogates processing relatively small molecular size for the validation of previous mechanisms. We expect several elementary reaction rate constants controlling the surrogate consumption pathways, such as the initial unimolecular decomposition and hydrogen atom abstraction reactions, to be measured using the shock tube/laser absorption technique.

### **Task 3: to perform experimental and modeling study of the chemical kinetics of biodiesel component.**

Methyl oleate (C<sub>19</sub>H<sub>36</sub>O<sub>2</sub>), the major component of the current biodiesel in use, is selected in this work for the fundamental study of its combustion kinetics. First, ignition delay time will be measured during the oxidation of MO at varied temperatures, pressures, and equivalence ratio. Ignition delay time is defined as the time between the arrival of the reflected shock wave (marked by the 50%-rise point of the pressure) at the observation port and the extrapolation of the maximum slope of the emission signal (here OH\* emission) to the baseline. We will extend these measurements to lower and higher pressures to cover wider experimental conditions (1-40 atm) using our advanced shock tube facility. All these data will test the ability of a mechanism to simulate the overall combustion reaction of fuel and oxygen combining to form products and release heat. Second, the mole fractions of individual molecules (fuel, products, or intermediates) can be measured throughout the reaction process using the species-specific laser-absorption diagnostics as developed in Task 1. Such time-histories primarily test the subset of the mechanism that includes reactions relating to the measured species. These measurements enable us to follow the time sequence of events occurring in a complex combustion system, from initial fuel breakdown, the formation of intermediates, radical build-up, and finally to the formation of the combustion products. Detailed kinetic modeling will be performed to interpret the measured species time-history data.

### 3. RESULTS ACHIEVED SO FAR

#### 1). Developed the advanced shock tube and laser diagnostics for time-resolved species detection.

We have developed a novel shock tube suitable to study fuels with very low-vapor-pressure (sub-Torr) such as the real biodiesel. The details can be found in Fig. 1. Compared to Stanford's method of aerosol generation using a supersonic nebulizer, our method can generate more uniform fuel aerosol with known fuel concentration and equivalence ratio. The fuel aerosol/gas mixtures being studied undergo two subsequent shock heatings and compressions.

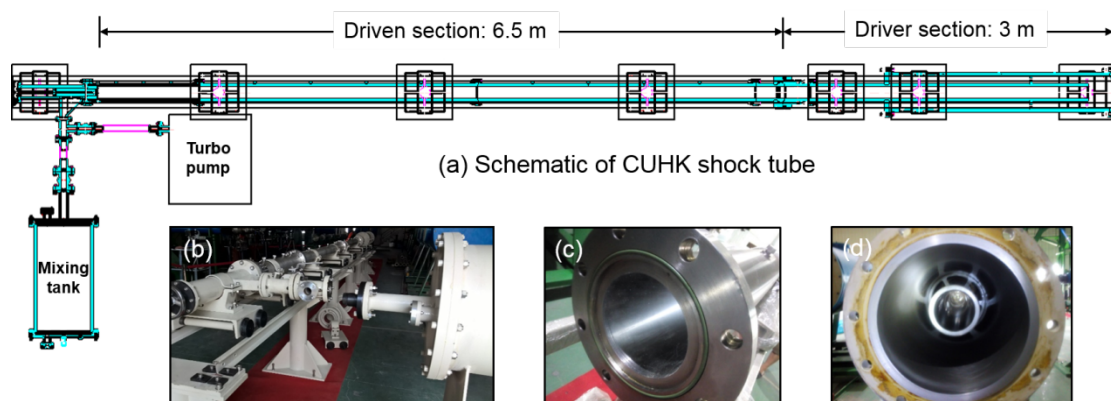


Fig. 1. (a) The stainless-steel, 10-m long shock tube recently built for high temperature chemical kinetics study. (b) The polished driven section with six pairs of optical windows. (c) The driver section with insert to achieve uniform shock conditions.

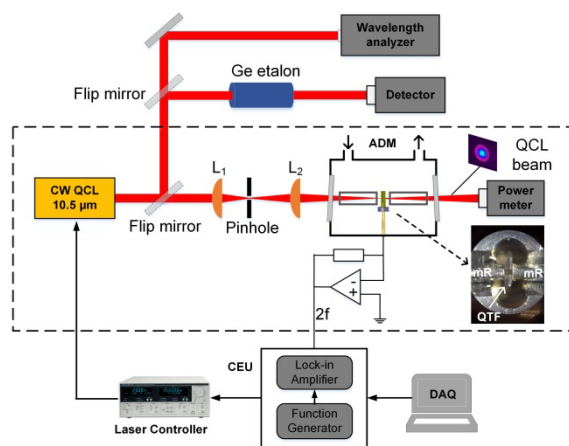


Fig. 2. Schematic and photo of the QEPAS sensor setup for  $C_2H_4$  detection.  $L_1$ ,  $L_2$ : plano-convex lens; ADM, acoustic detection module; QTF, quartz tuning fork; mR, micro-resonator; CEU, control electronics unit; DAQ, data acquisition.

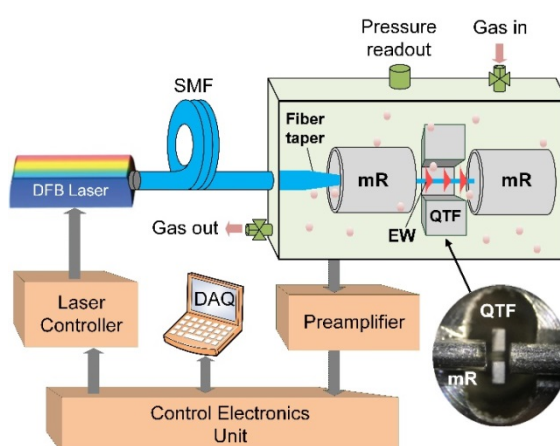


Fig. 3. Schematic of the EW-QEPAS setup. SMF, single mode fiber; mR, micro-resonator; QTF, quartz tuning fork; EW, evanescent wave.

Time-resolved laser diagnostics are required to monitor the species concentration time-histories during the pyrolysis or combustion of biofuels. We developed several different types of optical sensors for the sensitive detection of  $C_2H_4$  using a quantum cascade laser near  $10.5 \mu m$ , and CO using a distributed feedback laser near  $2.3 \mu m$ . These optical sensors achieve a detection sensitivity on ppm level that can be later applied in the combustion diagnostics during biodiesel combustion. Figure 2 and 3 depict the basic experimental setup for  $C_2H_4$  and CO, respectively. Parts of the results were published in the journal of *Optics Express* [J1] and *Applied Physics B* [J2].

## 2). *Improved the understanding of the combustion chemical kinetics of biodiesel surrogates.*

We performed shock tube study of the thermal decomposition of methyl butanoate (MB) using recently developed tunable diode laser absorption diagnostics. This paper extends the previous work by Farooq et al. of MB pyrolysis by taking advantages of new advancements in laser absorption sensors. Shock tube experimental conditions covered a temperature range of 1259–1521 K and pressure of ~1.5 atm. A much lower reactant concentration of 0.2% was used instead of 2–3% by Farooq et al. [1] to eliminate large uncertainties in absorption cross-sections during the endothermic pyrolysis process. In the current study, new discoveries of CO<sub>2</sub> and CO yields were observed during MB pyrolysis. Reaction pathway and sensitivity analyses were performed according to the current CO<sub>2</sub>/CO measurements and detailed kinetic modeling. These results were reported in the *The 10<sup>th</sup> Asia-Pacific Conference on Combustion* [C1] and *The 1<sup>st</sup> National Combustion Chemistry Meeting* [C2].

## 3). *Future work.*

In phase two of this project, we will mainly focus on the experimental and modeling study of the large methyl esters and biodiesel component. It includes the ignition delay time measurement of methyl decanoate (C<sub>11</sub>H<sub>22</sub>O<sub>2</sub>), methyl-5-decenoate (C<sub>11</sub>H<sub>20</sub>O<sub>2</sub>) and methyl oleate (C<sub>19</sub>H<sub>36</sub>O<sub>2</sub>). All these data will test the ability of a mechanism to simulate the overall combustion reaction of fuel and oxygen combining to form products and release heat. Meantime, we will quantitatively detect the major species (i.e., CO<sub>2</sub>, CO, H<sub>2</sub>O, C<sub>2</sub>H<sub>4</sub>) throughout the reaction process using the species-specific laser-absorption diagnostics. Such time-histories primarily test the subset of the mechanism that includes reactions relating to the measured species. Detailed kinetic modeling will be performed to interpret the measured species time-history data.

## 4. PUBLICATION AND AWARDS

J[1] Z. Wang, Z. Li, and W. Ren, “Quartz-enhanced photoacoustic detection of ethylene using a 10.5 μm quantum cascade laser,” *Optics Express*, OSA Publishing, USA, 24 (pp. 4143-4154), 2016.

J[2] Z. Li, Z. Wang, C. Wang, W. Ren, “Optical fiber tip-based quartz-enhanced photoacoustic sensor for trace gas detection,” *Applied Physics B*, Springer, Germany, in press, 2016.

C[1] W. Ren, D.F. Davidson and R.K. Hanson, “Methyl butanoate thermal decomposition: an improved shock tube study,” *The 10<sup>th</sup> Asia-Pacific Conference on Combustion*, The Combustion Institute, Beijing, China, 2015.

C[2] W. Ren, “Experimental and modeling study of methyl butanoate in a shock tube,” *The 1<sup>st</sup> National Combustion Chemistry Meeting*, Chinese Chemistry Society, Chengdu, China, 2015

COMPLETED

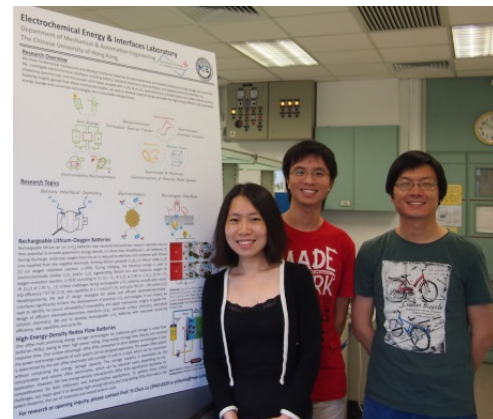
# EARTH-ABUNDANT METAL/METAL OXIDE NANOSTRUCTURES FOR RECHARGEABLE LI-AIR BATTERIES: CATALYST DESIGN AND MECHANISTIC INVESTIGATION

Principal Investigator: Professor Yi-Chun LU  
*Department of Mechanical & Automation Engineering  
CUHK*

Research Team Members: Yulin CAO, Research Assistant <sup>(1)</sup>,  
Zhuojian LIANG, Junior Research Assistant <sup>(1)</sup>,  
Yu Wang, Junior Research Assistant <sup>(1)</sup>

<sup>(1)</sup> Dept. of Mechanical & Automation Engineering, CUHK

**Project Start Date: 1 August 2013**  
**Completion Date: 31 July 2015**



## ABSTRACT

Electrical storage technologies are of vital importance to enable effective utilization of intermittent renewable energy sources and the creation of sustainable electric transportation. Lithium-air (or Li-O<sub>2</sub>) batteries have received extraordinary research attention owing to their potential to provide gravimetric energy density 3-5 times that of the conventional Li-ion batteries. However, the lack of fundamental understanding of the reaction mechanisms and materials design strategies has led to numerous critical challenges including poor round-trip efficiency, low rate capability, and poor cycle life. Here, we propose to develop earth-abundant metal/metal oxide nanostructures including nanoporous metal foams and mesoporous metal oxides as electrode materials to promote the rate capability, round-trip efficiency and cycle life of rechargeable Li-O<sub>2</sub> batteries. In addition, we will investigate the Li-O<sub>2</sub> interfacial chemistry and electrode reactivity via spectroscopic characterization techniques coupled with in situ and ex situ electrochemical characterizations. We seek to identify the source of instability/irreversibility and apply mechanistic insights to guide the design of efficient electrode-electrolyte interfaces (e.g., electrode surface chemistry, electrolyte solution chemistry). We intend to demonstrate rechargeable Li-O<sub>2</sub> batteries with improved round-trip efficiency, rate capability, and cycle life with minimum capacity loss.

## 1. OBJECTIVES AND SIGNIFICANCE

We aim to (1) develop earth-abundant nanostructured metal/metal oxide electrode materials to promote the rate capability and round-trip efficiency of rechargeable Li-O<sub>2</sub> batteries; (2) develop stable electrode-electrolyte interfaces to improve the cycle life of rechargeable Li-O<sub>2</sub> batteries; (3) unravel Li-O<sub>2</sub> reaction mechanisms, identify key processes that limit battery performance and develop design guidelines for stable and efficient electrode-electrolyte interfaces. These objectives will directly address the most critical challenges of rechargeable Li-O<sub>2</sub> batteries and are expected to enable transformative advances in rechargeable Li-air technology

## 2. RESEARCH METHODOLOGY

To improve the round-trip efficiency, rate capability and cycle life of rechargeable Li-O<sub>2</sub> batteries, we propose to (1) develop earth-abundant nanostructured metal/metal oxide electrode materials and (2) investigate Li-O<sub>2</sub> interfacial chemistry and identify battery degradation mechanism to guide the design of stable electrode-electrolyte interfaces. In addition to Li-O<sub>2</sub> batteries, we will apply materials investigated in this project to flow battery, aiming to find synergies of these two systems. The overview of the proposed research plans is summarized in Fig.1.

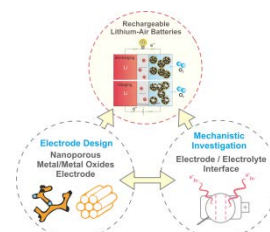


Fig.1. Overview of the research plans

### 2.1. Synthesis of nanostructured indium tin oxide/chromium oxide nano-composite

Indium tin oxide (ITO) is one of the most promising conducting oxides for electrochemical application and has been shown stable during Li-O<sub>2</sub> cycling environment by Li et al.<sup>1</sup> However, noble metal ruthenium (Ru) was used in the work of Li et al.<sup>1</sup> as a catalyst to facilitate the Li-O<sub>2</sub> reactions due to the low catalytic activity of ITO. One of the PI's studies has revealed that chromium-containing oxide exhibit superior charging activity compared to carbon and exhibit similar catalytic activity as noble metals. Therefore, we here exploit chromium oxide (Cr<sub>2</sub>O<sub>3</sub>)/ITO nano-composite as cathode materials for rechargeable Li-O<sub>2</sub> batteries. Here we use a surfactant assisting method followed by a low-temperature heat treatment. 50 mg ITO is firstly dispersed in 50 ml distilled water by ultrasonication for 15 min. Then 250 mg triblock copolymer (HO(CH<sub>2</sub>CH<sub>2</sub>O)<sub>106</sub>(CH<sub>2</sub>CH(CH<sub>3</sub>)O)<sub>70</sub>(CH<sub>2</sub>CH<sub>2</sub>O)<sub>106</sub>H) Pluronic® F127 is added under vigorous stirring for 24 h. Then 2 ml of K<sub>2</sub>CrO<sub>4</sub> (10 mg/ml H<sub>2</sub>O) is added to the above suspension under vigorous stirring for another 24 h. The resulting mixture is aged in air at 50 °C for 48 h in a Petri dish and then calcinated by heat treated at 500 °C for 1.5 h under H<sub>2</sub>/Ar atmosphere.

### 2.2. Synthesis of nanostructured titanium carbide

Titanium carbide (TiC) has been recently reported to demonstrate superior cycling stability in rechargeable Li-O<sub>2</sub> batteries.<sup>2</sup> However, the TiC used in the reported literature only exhibits limited specific surface area (~15 m<sup>2</sup>/g),<sup>2</sup> which significantly limit the specific capacity of the Li-O<sub>2</sub> batteries. Here we aim to synthesize high surface area TiC using C<sub>3</sub>N<sub>4</sub> as carbon source.<sup>3</sup> Bulk C<sub>3</sub>N<sub>4</sub> can be synthesized using melamine as precursor.<sup>4</sup> We design a solid-state reaction assisted by carbothermal reduction process to synthesize fine TiC nanoparticles. The C<sub>3</sub>N<sub>4</sub> acts as a precursor to react with another oxide TiO<sub>2</sub> at 1100-1200 °C. The C<sub>3</sub>N<sub>4</sub> was firstly prepared by reaction of melamine under air at 500-600 °C according to the literature.<sup>4</sup> For the fabrication of TiC, the as-synthesized C<sub>3</sub>N<sub>4</sub> and oxide TiO<sub>2</sub> are mixed together. The mixed powder are then put on an alumina boat and inserted into a tube furnace. The furnace is evacuated to 10<sup>-2</sup> mbar. And then the furnace is heated to 1100-1200 °C at the rate of 5 °C/min and kept at high temperature for 1-2 hours. Finally, black powder sample is obtained and cooled down naturally to room temperature.

### 2.3 Synthesis of porous silicon nanowires

Porous materials have been used as supports for catalysts because of their large number of pores, large surface area, and ease of recycling compared with other nanomaterials. Porous Si nanowires (Si NWs) have high surface areas, good electrical conductivity and fine chemical stability, which make Si NWs interesting candidate as cathode materials for rechargeable Li-O<sub>2</sub> batteries. We synthesize Si NWs via a method involving the deposition of silver particles on the surface of bare Si substrates followed by wet chemical etching.<sup>5</sup> Briefly, pieces of commercially available highly doped p-type Si(100) wafers are used as starting materials. The Si wafers are cleaned by sonication in DI water, acetone and isopropanol and dried by nitrogen blowing. The cleaned Si wafers are immersed on a buffered oxide etchant (BOE) for 2 minutes to remove the native oxide layer and then immersed in a solution containing 0.01-0.04 M AgNO<sub>3</sub> and 5 M HF for 1 minute at room temperature. The colorful surface of Si wafer indicates that Ag nanoparticles have been formed on Si surface. The Ag-deposited Si wafers are cleaned with DI water to remove the extra Ag<sup>+</sup> ions and then immersed on the solution containing 4.8 M HF and 0.3 M H<sub>2</sub>O<sub>2</sub> for different time. Finally the Ag particles are removed by immersing the Si wafers in the concentrated H<sub>3</sub>NO<sub>3</sub> for one hour. The as-etched products are inspected with a scanning electron microscope (SEM) at 10 kV of electron acceleration voltage.

### 2.4 Synthesis of sulfur/carbon composite

We prepare sulfur/carbon (S/C) as a flow electrode material.<sup>6</sup> Sulphur and KB were mixed with a mass ratio 22:1 in DME followed by sonication with SLPt Cell Disruptor (Branson, USA) for 30 min. The sulphur and KB mixture was first air-dried at 25 °C for 2 hours to remove most of the solvent followed by heat treatment at 155 °C for 6 hours for sulphur impregnation. The chemical composition of the S/C composite was determined to be 93.1 wt.% sulphur and 6.9 wt.% KB by thermogravimetric analysis (TGA) (Fig. 2).

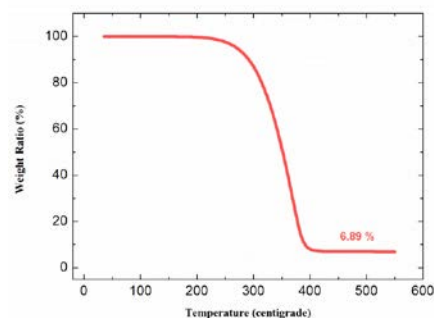


Fig. 2. TGA analysis of S/C composite. (25 – 550 °C at 10 °C/min).

## 2.5. Lithium-air cell design and assembly

We have designed and fabricated an electrochemical Li-O<sub>2</sub> testing apparatus or Li-O<sub>2</sub> cells, as shown in Fig. 3. The cell design is modified upon on a model proposed by the PI in a previous work.<sup>7-8</sup> Basic function of the cell is to enclose battery components and active material and protect them from exposing to the ambient environment. The cell composes mainly of stainless steel and polytetrafluoroethylene (PTFE). The cell is assembled by placing a lithium metal foil, a polymer separator (Celgard 2325), a cathode and a current collector in the center of the bottom plate, between two of which 100uL of electrolyte (0.1 M lithium perchlorate (LiClO<sub>4</sub>) in dimethyl sulfoxide (DMSO)) is added, followed by installing bolts that hold the top plate, spacer and bottom plate together. Gas (i.e., pure O<sub>2</sub>) is then purged through the valves and the gauge will be used to indicate quality of the hermetic sealing. We have conducted a leakage test that successfully proved that the cell can be well-sealed. Therefore the fabricated cell is suitable for our future work on battery materials.

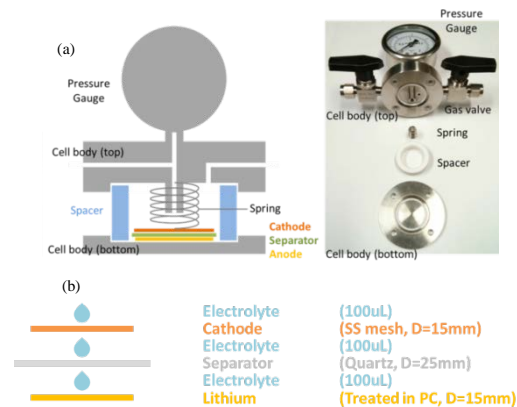


Fig. 3. (a) Illustration of the Li-O<sub>2</sub> cell; (b) Assembling of Li-O<sub>2</sub> cells

## 3. RESULTS ACHIEVED

### 3.1. Materials characterization of as-synthesized Cr<sub>2</sub>O<sub>3</sub>/ITO cathode material.

Cathode materials consisting Cr<sub>2</sub>O<sub>3</sub> nanoparticles supported on ITO were synthesized by a soft template method followed by low temperature heat treatment. Fig. 4 shows the schematic of the synthesis process, SEM and energy-dispersive X-ray spectroscopy (EDS) of the as-synthesized Cr<sub>2</sub>O<sub>3</sub>/ITO. It is interesting to note that the original color of ITO was yellow and after the coating of Cr<sub>2</sub>O<sub>3</sub>, the final Cr<sub>2</sub>O<sub>3</sub>/ITO product is dark color, which might indicate improved electronic conductivity. The EDS result shows the major composition consists of In, Sn, and Cr. The atomic ratios of Cr and In elements are 19.08% and 54.12%, respectively.

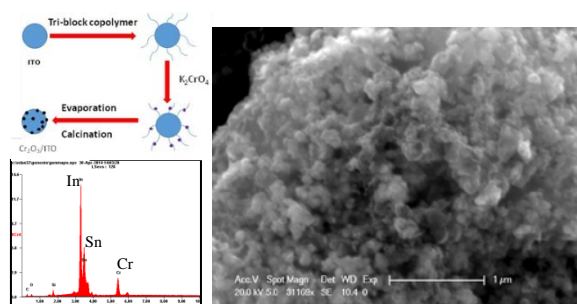


Fig. 4. Synthesis process of Cr<sub>2</sub>O<sub>3</sub>/ITO; SEM and EDS spectrum of the as-synthesized Cr<sub>2</sub>O<sub>3</sub>/ITO

### 3.2. Materials characterization of as-synthesized TiC cathode material.

Fig. 5 shows the SEM images and the XRD pattern of as-synthesized black product by the solid-state reaction assisted by carbothermal reduction method described earlier. SEM images show that the obtained product composed of irregular nanoparticles. The EDS spectrum (not shown here) shows that the as-synthesized product contains the Ti, O, and C elements. And the atomic ratios of Ti and C elements are 17.07% and 14.93%, respectively. The atomic ratio of Ti/C is close to 1:1.

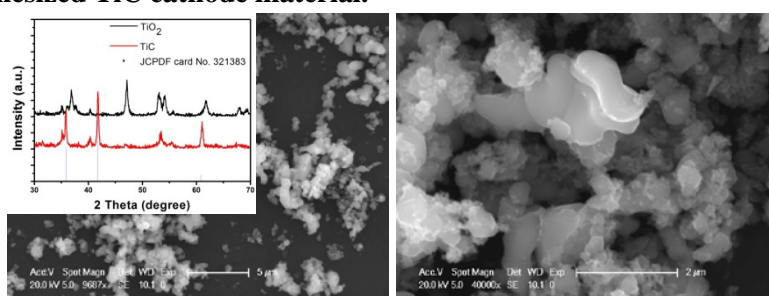


Fig. 5. SEM images and XRD pattern of as-synthesized TiC.

The XRD pattern demonstrate that the as-synthesized product was crystalline TiC. The index pattern basically agrees with JCPDS card no.32-1383. The XRD pattern of oxide precursor TiO<sub>2</sub> was also shown for comparison. It means that the TiO<sub>2</sub> precursor can be transformed into TiC after reaction with C<sub>3</sub>N<sub>4</sub> by present method in this case. The results suggest that this route is effective in converting TiO<sub>2</sub> to TiC. The reaction mechanism can be expected to include two steps: Firstly, C<sub>3</sub>N<sub>4</sub> decomposes into different carbon nitride species, such as C<sub>2</sub>N<sub>2</sub><sup>+</sup>, C<sub>3</sub>N<sub>2</sub><sup>+</sup>, and C<sub>3</sub>N<sub>3</sub><sup>+</sup>, at temperature higher than 550 °C. These species are highly reactive and easily bonded to oxygen atoms and reduce the titanium oxide into titanium metal. The subsequent carbonizing process between the titanium metal and the carbon-rich species will occur and finally lead to the formation of nanoparticles of TiC.

### 3.3. Materials characterization of as-synthesized porous Si NWs cathode material.

Fig. 6 shows the photograph (top left) and top view SEM image (top right) of the as-synthesized Si nanowires on highly doped Si substrate. In order to clearly reveal the Si NWs morphologies, the cross-section view of the Si substrate is shown in Fig. 5 (bottom). It is observed that surface of Si substrate is etched and morphology of these etched Si is nanowire arrays. The Si nanowire arrays have length of 10  $\mu\text{m}$  and width of 80-120 nm. The Si nanowire arrays have been successfully fabricated. The Si nanowires have crystalline crystal structures and large length-diameter aspect ratio and porous properties.<sup>9</sup> The as-synthesized porous Si nanowires have large surface areas which may be a good candidate as catalyst supporter.

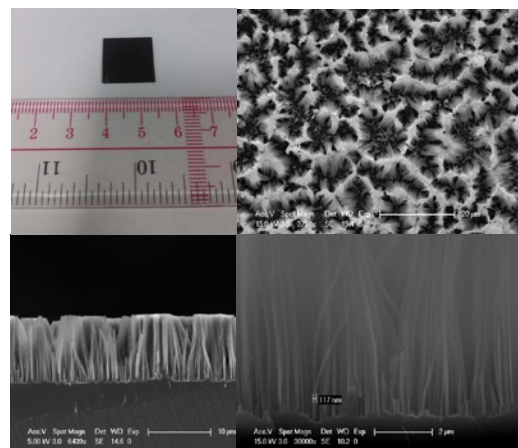


Fig. 6. Photograph and SEM images of Si NWs.

### 3.4. Materials and electrochemical characterization of sulfur/carbon electrode

Fig. 7 shows the galvanostatic measurement and the scanning electron microscope/energy-dispersive X-ray spectroscopy (SEM/EDX) images of four S/C electrodes including a mechanically-mixed S/C suspension with 5.0 vol% S- 12.0 vol% carbon (Ketjen black, KB) and three S-impregnated S/C composite electrode (i.e., 5.0 vol% S- 12.0 vol% KB (5S-12KB), 5.0 vol% S- 26.0 vol% KB (5S-26KB), 20.0 vol% S- 26.0 vol% KB (20S-26KB)). Impregnation of S with the conductive carbon matrix improves the electrical conductivity of the electrode and enhances the interfacial contacts between the insulating solid S and the carbon matrix, compared to mechanically-mixed suspension. The gravimetric discharge capacity of the mechanically-mixed catholyte (Fig. 7, 5S-12KB-MM, 700 mAh/g<sub>S</sub>) is lower than that of the S/C composite electrode (5S-12KB, 1235 mAh/g<sub>S</sub>) by ~50%. This suggests that the utilization of S in the catholyte is enhanced by uniformly intermixing of S and C using S impregnation. The SEM/EDX image of the 5S-12KB electrode shows that the S and C atoms are evenly distributed and overlapped across the composite suspension. On the other hand, the S and C atoms are separated in the mechanically mixed suspension (5S-12KB-MM).

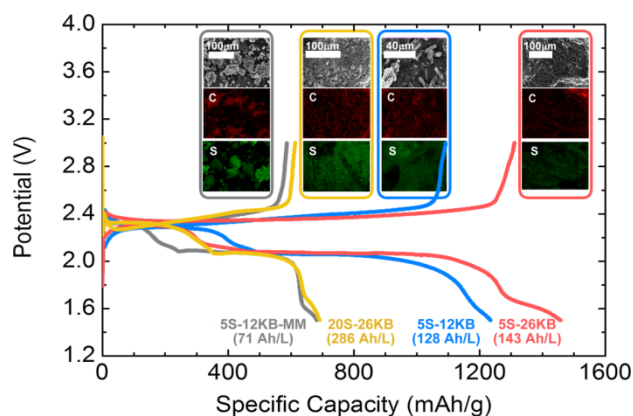


Fig. 7. Galvanostatic measurement of Li/S-C cells using S/C composite of 5S-12KB-MM, 5S-12KB, 5S-26KB, and 20S-26KB at C/9 ( $1C \equiv 1675 \text{ mA/g}_S$ ). Inserts: SEM/EDX images of as-prepared electrode of 5S-12KB-MM, 5S-12KB, 5S-26KB, and 20S-26KB.

### 3.5. O<sub>2</sub>-cathode fabrication and electrochemical characterization of select cathode materials

Oxygen-cathodes are fabricated by first mixing the cathode powder with PTFE binder in the ratio 95:5 (m/m) in isopropanol (Fig. 8a). The slurry is then drop casted onto a stainless steel mesh (0.6 mg/cm<sup>2</sup>). The coated mesh is dried in vacuum for over 12 hours at 150 °C. After this the electrodes are transfer to the glove box without exposure to air. As shown in Fig. 8b, the resulted electrode that the cathode material is evenly distributed across the mesh, both on and between the mesh wires. We systematically prepare five metal carbides electrodes including TiC, vanadium carbide (VC), chromium (Cr<sub>3</sub>C<sub>2</sub>), molybdenum carbide (Mo<sub>2</sub>C), and tungsten carbide (WC). The galvanostatic electrochemical characterizations of the five carbide nanoparticles are shown in Fig. 8c. The rates for discharge and charge were 50mA/g<sub>cathode</sub> and 10mA/g<sub>cathode</sub>, respectively. We also limited the discharge process to a capacity of 100mAh/g<sub>cathode</sub> to examine the discharge and charge behavior of Li-O<sub>2</sub> batteries without forming large/thick insulating Li<sub>2</sub>O<sub>2</sub> particles. As shown in Fig. 8c, the VC exhibits low discharge (i.e., poor discharge activity) but exceptionally low charge voltage (i.e., high charge activity). The low discharge voltage may be explained by its relatively small specific surface area, which further suggests that the VC exhibits the best catalytic activity for charging of the Li-O<sub>2</sub> batteries among the five carbides. In addition, TiC shows the highest charge potential, suggest that TiC

exhibit lower charging activity compared with other four carbides. We further characterize the electrochemical activities of four titanium based electrode materials including TiC, TiN, TiB<sub>2</sub> and TiO<sub>2</sub>. As shown in Fig. 9, the discharge process, or oxygen reduction reaction activity of TiC is the highest followed by TiN, TiB<sub>2</sub> and TiO<sub>2</sub>. Interestingly, the charge process, or oxygen evolution reaction activity of TiC is also the highest followed by TiN, TiB<sub>2</sub> and TiO<sub>2</sub>. Our study successfully identifies TiC as a highly-active bi-function electrocatalyst for Li-O<sub>2</sub> batteries.

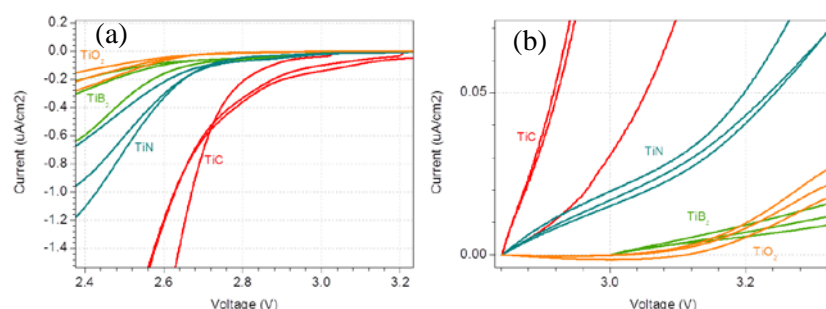


Fig. 9. Polarization curves of TiC, TiN, TiB<sub>2</sub> and TiO<sub>2</sub> electrodes in 0.1 M LiClO<sub>4</sub> in TEGDME for (a) oxygen reduction reaction and (b) oxygen evolution reaction.

### 3.6. Design of on-line electrochemical mass spectrometer & results on carbon-free electrode in Li-O<sub>2</sub> batteries.

We designed and developed an on-line electrochemical mass spectrometer (OEMS, Fig. 10)<sup>8</sup> to identify and quantify the gas or volatile species formed in the cell during charge. It consists of an electrochemical cell, a sampling system and a mass spectrometer. A pressure transducer will be connected to the cell and measures during discharge the change of oxygen pressure, from which the amount of oxygen consumed can be determined. During charging, the gas and volatile species yield during charge will be sent to the vacuum chamber by the sampling system. The mass spectrometer is used to analyze the composition of the gas. Fig. 11 shows the OEMS result of TiC electrode during discharge (Fig. 11a) and charge (Fig. 11b) of Li-O<sub>2</sub> operation. We monitored the oxygen consumption during discharge and quantitatively correlate to the electron passed to perform oxygen reduction reaction. The current (orange line) matched well with the oxygen consumption for a 2e<sup>-</sup> per oxygen molecule according to  $O_2 + 2e^- + 2Li^+ \rightarrow Li_2O_2$ . During charging, we successfully detected O<sub>2</sub>, CO and CO<sub>2</sub> at the end of the charging process. Since this is a carbon-free electrode, the detection of CO and CO<sub>2</sub> indicates that the electrolyte decomposed at voltage round 4.4 V. This highlights that developing stable electrolyte is critical to enable reversible Li-O<sub>2</sub> batteries.

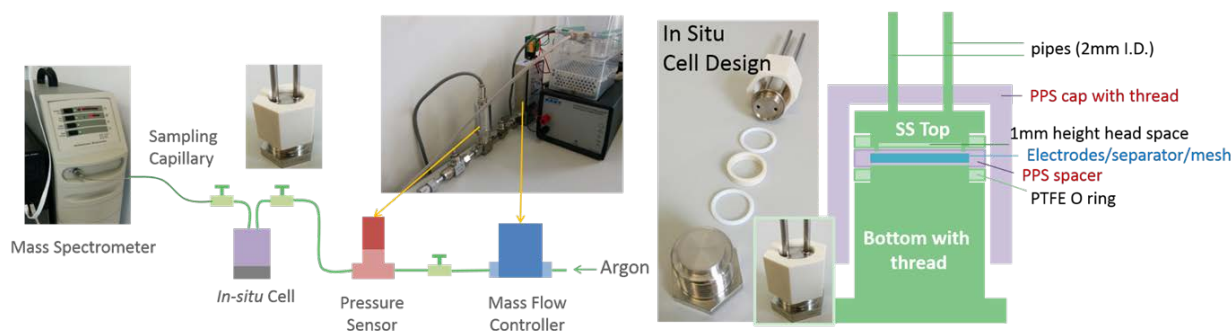


Fig. 10. Design the on-line electrochemical mass spectrometer

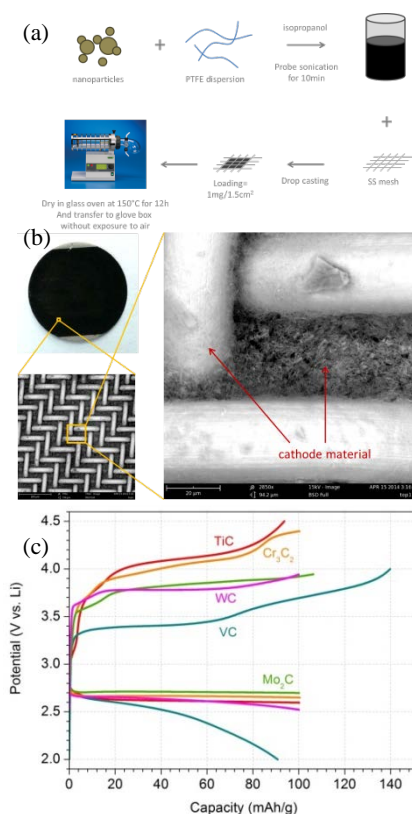


Fig.8. (a) Cathode fabrication (b) SEM image of O<sub>2</sub>-cathodes on stainless steel. (c) galvanostatic profile of Li-O<sub>2</sub> cells with cathode materials including TiC, Cr<sub>3</sub>C<sub>2</sub>, WC, VC and Mo<sub>2</sub>C.

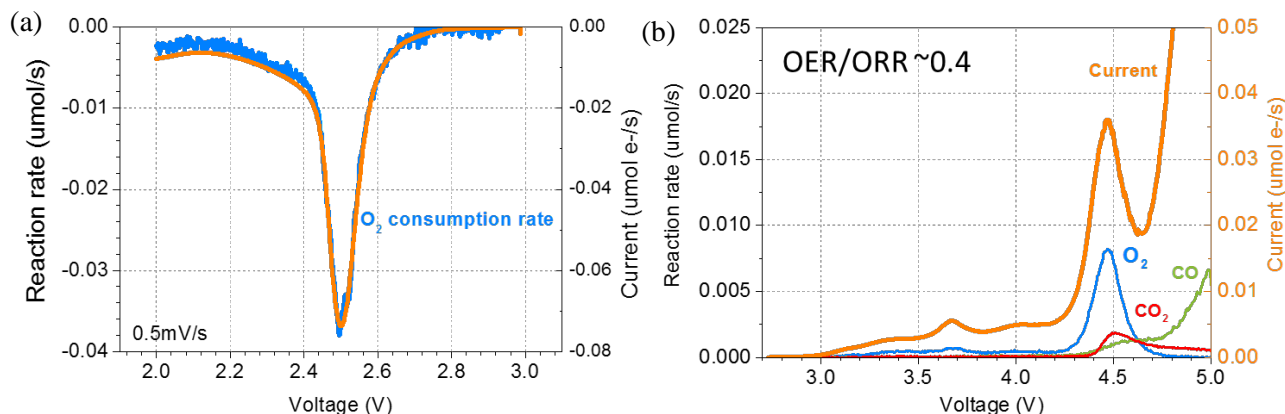


Fig. 11. OEMS result of a Li-O<sub>2</sub> battery using TiC electrode in DMSO. (a) Discharge process, oxygen reduction reaction; (b) Charge process, oxygen evolution reaction.

References: (1) Li et al., *Nano Lett.* 2013, 13, 4702. (2) Ottakam Thotiyl et al., *Nat. Mater.* 2013, 12, 1050. (3) Li et al., *J. Alloys Compd.* 2007, 430, 237. (4) Zhang et al., *J. Am. Chem. Soc.* 2013, 135, 18. (5) Qu et al., *Nanoscale* 2011, 3, 4060. (6) Chen et al., *Nat. Commun.* 2015, 6, Article number: 5877. (7) Lu et al., *Energy Environ. Sci.* 2011, 4, 2999 (8) Wang et al., *J. Phys. Chem. C*, DOI: 10.1021/acs.jpcc.6b00984 (2016) (9) Qu et al., *J. Mater. Chem.* 2010, 20, 3590.

#### 4. PUBLICATION AND AWARDS

##### Journal:

1. H. Chen, Q. Zou, Z. Liang, H. Liu, Q. Li, and Y.C. Lu, "Sulphur-Impregnated Flow Cathode to Enable High-Energy-Density Lithium Flow Batteries," *Nature Communications*, Nature Publishing Group, 6, Article number: 5877, Jan. 07 2015

##### Conference:

2. Y. Wang; Z. Liang, and Y.C. Lu, "Probing the Working Mechanism of Electrocatalyst-Assisted Nonaqueous Lithium-Oxygen Evolution Reaction," *227th Electrochemical Society (ECS) Meeting*, Electrochemical Society, Chicago, United States of America, May 27 2015.
3. H. Chen, Q. Zou, Z. Liang, H. Liu, Q. Li, and Y.C. Lu. "A Sulfur-Impregnated Flow Cathode for High-Energy Lithium Flow Batteries," *227th Electrochemical Society (ECS) Meeting*, Electrochemical Society, Chicago, United States of America, May 27 2015.
4. Z. Liang and Y.C. Lu, "Probing the Oxygen Evolution Efficiency of Redox Mediator-Catalyzed Lithium-Oxygen Batteries using On-Line Electrochemical Mass Spectrometer" *The 66th Annual Meeting of the International Society of Electrochemistry*, International Society of Electrochemistry, Taipei, Taiwan, 4-9 October 2015.
5. Q. Zou, and Y.C. Lu, "Influence of Electrolyte on Sulfur Redox Reactions: Combined RRDE and in situ UV-VIS Studies" *The 66th Annual Meeting of the International Society of Electrochemistry*, International Society of Electrochemistry, Taipei, Taiwan, 4-9 October 2015.

# GRAPHENE-BASED ASYMMETRIC SUPERCAPACITORS WITH HIGH ENERGY DENSITY FOR CLEAN ENERGY STORAGE SYSTEMS

Principal Investigator: Professor ZHANG Li  
*Department of Mechanical & Automation Engineering, CUHK*

Research Team Members:

Fen Wang<sup>(1)</sup>, Lijuan Han<sup>(1)</sup>, Yabin Zhang<sup>(1)</sup>,  
Dongdong Jin<sup>(1)</sup>, Dr. Rutao Wang<sup>(1)</sup>

<sup>(1)</sup> Dept. of Mechanical & Automation Engineering, CUHK

**Project Start Date: 1 July 2013**  
**Completion Date: 31 August 2015**



## ABSTRACT

The objective of the proposed research is to fabricate, characterize and optimize supercapacitors, energy storage devices based on nanocomposite, with high performance for clean energy storage systems.

Supercapacitors have attractive properties such as high charge-discharge efficiency at high power densities, long cycling life, and pollution-free for clean energy storage; however, to date, their potential applications are hindered by the low energy density. Nanocomposites are recently considered as an ideal electrode material for supercapacitors due to their 3D open microstructures and excellent intrinsic physical properties such as ultra-high specific surface area (SSA), outstanding electrical conductivity and excellent mechanical and chemical stability. Though supercapacitors are promising for practical applications, their energy and power densities are still need to be adequately improved to reach their best performance.

Taking advantage of novel synergistic effect of carbon-based nanomaterials/transition-metal nanostructures/conductive polymer components, the PI proposes to design and prepare supercapacitors using nanocomposites as electrodes, and to characterize and optimize the microstructural and electrochemical properties of prototype supercapacitor devices having high energy and power densities. The ultimate goal is to develop high-performance and low-cost supercapacitors which can be scaled-up for future commercial applications.

## 1. OBJECTIVES AND SIGNIFICANCE

The objective of the project is as follows:

1. To synthesize graphene oxide (GO) from expanded graphite using Hummers method. Since the surface of GO containing rich oxygen functional groups, it is an advantage to dispersively anchor metal ions for the nucleation of nanoscale metal oxides or hydroxides for the preparation of graphene-based nanocomposites.
2. To fabricate metal-oxide/reduced-graphene-oxide nanocomposites (MO/RGO, such as nanocomposite consisting of  $Mn_3O_4$  and RGO) and metal hydroxide/graphene (MOH/RGO) nanocomposites using a one-step solution method, a facile and low-cost process. Their microstructural aspects will be investigated by SEM, high resolution electron microscopy (HRTEM), X-ray diffraction (XRD), infrared spectrometer and thermogravimetric analysis (TG) to understand the formation mechanism of the nanocomposites.

3. To design and prepare prototype asymmetric supercapacitors using MO/RGO or MOH/RGO as positive electrodes and activated carbon as negative electrodes. These kinds of asymmetric supercapacitors are expected to have much higher working voltage and energy density than other type of supercapacitors.
4. To investigate the electrochemical properties of the as-fabricated supercapacitors using cycle voltammetry (CV), galvanostatic charge–discharge and electrochemical impedance spectroscopy (EIS) to determine their capacitance properties.
5. To conduct systematic optimization from both the nanocomposition of the hybrid materials and the design of the asymmetric electrodes to enhance the capacitor performance.

**Significance of the research:** The proposed study will impact scientific and technological development through providing high-performance supercapacitors for future low-cost and environmental-friendly commercial energy storage systems.

## 2. RESEARCH METHODOLOGY

The facile synthesis techniques for the preparation of graphene-based nanocomposites will be developed in the first phase of the research. GO will be fabricated from expanded graphite by Hummers method. It is beneficial for the dispersive nucleation of nanoscale metal oxides or hydroxides to prepare graphene-based nanocomposites due to the surface of GO containing rich oxygen functional groups. Then, a one-step solution method will be applied to fabricate metal-oxide/graphene and metal hydroxide/graphene nanocomposites, which is a low-cost technique.

In order to understand the relationship between the materials, structures and the corresponding electrochemical properties, each as-prepared nanocomposites will be investigated by SEM, HRTEM, XRD, infrared spectrometer and thermogravimetric analysis to study the formation mechanism of the nanocomposites and their influence on the electrochemical properties. Also EDX will be used to determine their elemental compositions. Upon completion, we will be able to unveil the dependence of composition, synthesis process, microstructures and electrochemical properties, which, hence, helps to systematically optimize their capacitance performance.

The third goal of this project is to design and construct prototype supercapacitor with optimized performance. We will use MO/RGO and MOH/RGO as positive electrodes and activated carbon as negative electrodes for the preparation of asymmetric supercapacitors. Their electrochemical properties will be tested by CV, galvanostatic charge–discharge and EIS to characterize their specific capacitance, energy and power density, and impedance; then, the experimental data will be investigated for further optimization of the capacitance performance of the devices. We will address and clarify the effects of these factors on figure-of-merit and provide materials design principles for high-performance graphene-based asymmetric supercapacitors.

## 3. RESULTS ACHIEVED

Based on the funding support from Shun Hing, we have published 6 journal papers and 1 conference proceeding, in which two journal papers (i.e. J[3] and J[5]) were highlighted as journal front covers. Furthermore, based on the achievement from the Shun Hing funding, I have successfully obtained one ITF (tier-2) grant as the PI and I had applied one Chinese Invention Patent with my Shun Hing team members (pending).

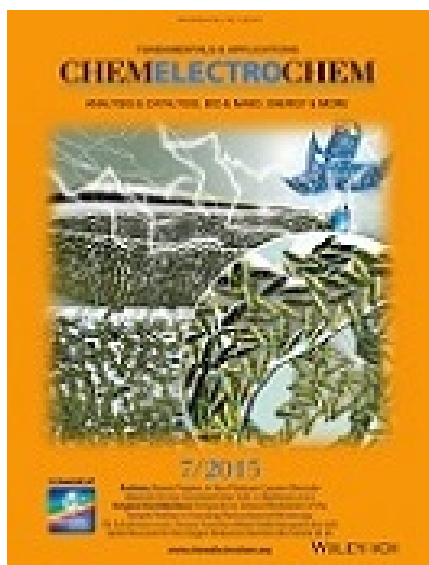
### Patent

1. P.Y. Tang, L.J. Han, L. Zhang, "基於超級電容器隔膜的復合平面電極及其製備方法", Chinese Invention Patent (Pending), 201410101760.1, applied in Mar. 2014.

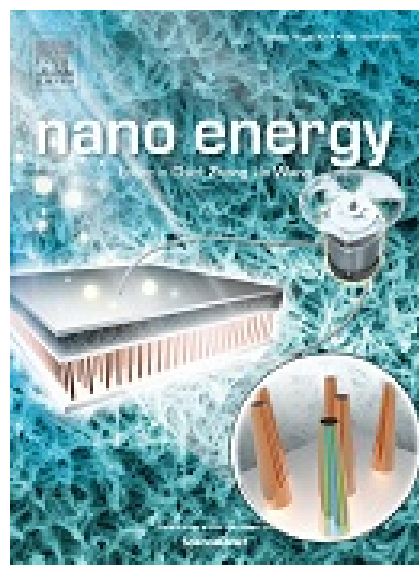
## ITF funding secured due to the Shun Hing Project outcome

1. **Principal Investigator**, HKSAR Innovation and Technology Commission (ITC) Innovation and Technology Fund (ITF), Tier-2 platform project, “Development of Eco-friendly Flexible Ultrathin Supercapacitors for Next-Gen Smart Cards”, HK\$ 1,700,288, 12/2014 – 11/2016, in which HK\$ 250,000 are the sponsorship from two local industrial companies. **The project No. ITS/160/14FP.**

## Journal cover highlights



J[3]



J[5]

The journal paper J[3] was also highlighted as a VIP paper in *ChemElectroChem*, and the cover profile highlight is shown in the next page.

## 4. PUBLICATION AND AWARDS

### Journal papers

J[1] L. J. Han, Y. J. Cai, P. Y. Tang\*, L. Zhang\*, “Microscale Flowers: Controlled Synthesis of Co<sub>3</sub>O<sub>4</sub> Nanostructures Using Soft-Templates-assisted Self-assembly”, *Materials Today*, Vol. 18, pp. 410-411, 2015. **(impact factor: 14.107)**

J[2] L. J. Han, P. Y. Tang, L. Zhang\*, “Encapsulation Architecture for Energy Storage”, *Materials Today*, Vol. 18, pp. 352-353, 2015. **(impact factor: 14.107)**

J[3] P. Y. Tang, L. J. Han, L. Zhang, S. Wang, W. Feng, G. Xu, L. Zhang\*, “Controlled Construction of Hierarchical Nanocomposites Consisting of MnO<sub>2</sub> and PEDOT for High-performance Supercapacitor Applications”, *ChemElectroChem*, Vol. 2, pp. 949-957, 2015. **(highlighted as the front cover)** (impact factor: Pending) **VIP paper of the journal with cover profile highlight**

J[4]. P. Y. Tang, L. J. Han, L. Zhang\*, “Facile Synthesis of Graphite/PEDOT/MnO<sub>2</sub> Composites on Commercial Supercapacitor Separator Membranes as Flexible and High-Performance Supercapacitor Electrodes”, *ACS Applied Materials & Interfaces*, Vol. 6, pp. 10506-10515, 2014. **(impact factor: 6.723)**

J[5]. L. J. Han, P. Y. Tang, L. Zhang\*, Hierarchical Co<sub>3</sub>O<sub>4</sub>@PPy@MnO<sub>2</sub> Core-shell-shell Nanowire Arrays for Enhanced Electrochemical Energy Storage, *Nano Energy*, Vol. 7, pp. 42-51, 2014. **(highlighted as the front cover)**. **(impact factor: 10.325)**

J[6]. Q. Li, J. Cheng\*, B. Wang, L. Zhang\*, “Activated Carbon Modified by CNTs/Ni-Co Oxide as Hybrid Electrode Materials for High Performance Supercapacitors”, *IEEE Transactions on Nanotechnology*, Vol. 13, pp. 557-562, 2014. **(impact factor: 1.825)**

### Conference paper

C[1]. Q. Li, J. Cheng, L. Zhang, “Nickel-cobalt Oxide Coated CNTs as Additives of Activated Carbon Electrode for High-performance Supercapacitors”, *Proc. of The 13th IEEE International Conference on Nanotechnology (IEEE NANO 2013)*, Beijing, China, Aug. 5-8, 2013.

## Controlled Construction of Hierarchical Nanocomposites Consisting of MnO<sub>2</sub> and PEDOT for High-Performance Supercapacitor Applications



Pengyi Tang



Lijuan Han



Group photo including Shijie Wang, Lin Zhang, and Prof. Li Zhang (4th, 6th, and 9th from the left, respectively).



Wei Feng



Guoqing Xu



香港中文大學  
The Chinese University of Hong Kong



中国科学院深圳先进技术研究院  
SHENZHEN INSTITUTES OF ADVANCED TECHNOLOGY  
CHINESE ACADEMY OF SCIENCES

The front cover artwork is provided by the group of Professor Li Zhang from The Chinese University of Hong Kong and his collaborators from the Shenzhen Institutes of Advanced Technology, Chinese Academy of Science. The image shows the fabrication of core-shell-branch hierarchical MnO<sub>2</sub>@PEDOT/MnO<sub>2</sub> nanocomposites, using simple electrochemical deposition for supercapacitor applications. Read the full text of the Article at 10.1002/celec.201500025.

### What is the most significant result of this study?

The most significant result is that the controlled fabrication of core-shell-branch MnO<sub>2</sub>@PEDOT/MnO<sub>2</sub> nanocomposites can be achieved by using a simple electrochemical deposition approach, and the obtained nanocomposites exhibit excellent electrochemical properties for energy-storage applications.

### Acknowledgments

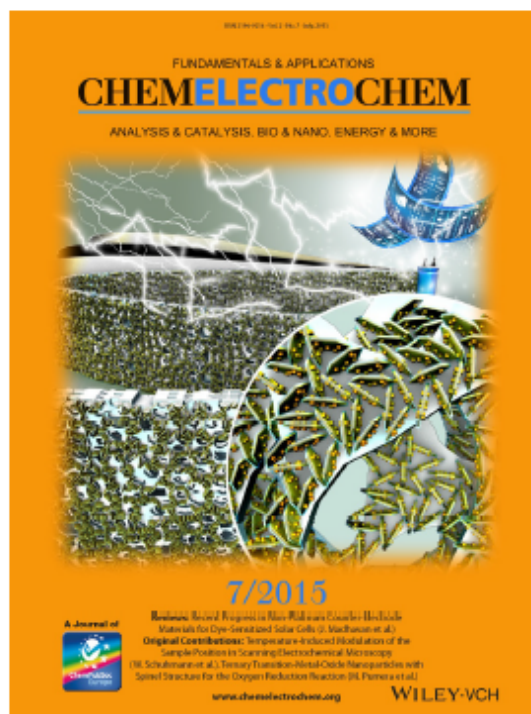
This work was partially supported by HKSAR Innovation and Technology Commission (ITC) with the Project No. ITS/160/14FP, and the **Shun Hing Institute of Advanced Engineering (SHIAE)** at CUHK with the Project No. 8115045.

### What prompted you to investigate this topic?

Many researchers have reported that hybrid nanocomposites composed of organic and inorganic materials can be obtained by using a combination of electrochemical deposition with hydrothermal and in situ chemical reaction methods. However, it is still a great challenge to synthesize hierarchical organic/inorganic nanocomposites by employing a simple electrochemical method.

### What other topics are you working on at the moment?

Prof. Zhang's group at the Chinese University of Hong Kong is dedicated to interdisciplinary research topics that bridge micro-/nanotechnology and functional materials with robotics technology at small scales, that is, micro-/nanorobotics. The primary research objectives of the group range from the development of functional nanomaterials to intelligent micro-/nanoscale machines and robotic systems for biomedical, energy storage, and environmental applications. The motivation of our collaborative research is to develop enabling materials, devices/systems, and technologies for the sustainable society and a better life.



## Biomedical Engineering Track

# Research Reports In Biomedical Engineering

### Newly Funded Projects

- (2017-2019) \* Development of a Novel Robotic Manipulator for Confined Space Surgery
- \* Development of an Inertial Microfluidics Based Approach for the Isolation of Mitochondria from Biological Samples

### Continuing Projects

- (2016-2018) \* An MRI-guided Robotic System for Breast Biopsy
- \* Intention-driven Shoulder Rehabilitation for Targeted Meuro-muscular Training using an Exo-musculoskeletal Robot
- \* Engineering Antimicrobial Surfaces Based on Micro-topography Using a Novel Ultrasonic Machining Method
- (2015-2017) \* Development of a Novel flexible Surgical Robot with Haptic Sensation
- \* Development of Injectable Supramolecular Hydrogels for Regenerative Medicine
- \* Developing Optomechanical Devices based on Layered Nanomaterials for Single-Biomolecule Mass Spectrometry

**Completed Projects**

- (2014-2016) \* Development of High-speed Laser Scanning Microscope for In Vivo Deep Brain Imaging
- \* Mechanism for the Transcytosis of Targeted Nanoparticles Across the Blood-brain barrier
- (2013-2015) \* Development of the Next Generation Neurosurgical Assistant System Based on Functional Brain Mapping
- \* Biomimetic scaffold for stem cell based cartilage regeneration and drug delivery

---

The following reports are enclosed in “Research Highlights” printed in June 2015

**Completed Projects**

- (2012) \* Dielectrophoresis Nano-separator for Precision Manufacturing of Polymeric Nanoparticles for Tumor-Targeted Drug Delivery

---

The following reports are enclosed in “Research Highlights” printed in June 2014

**Completed Projects**

- (2011) \* Viewing Biomolecules at the Right Site by Plasmonic Tweezers and Surface Enhanced Raman Scattering

---

The following reports are enclosed in “Research Highlights” printed in 2013

**Completed Projects**

- (2010) \* An inexpensive functional finger prosthesis with rebounded type progressive hinge lock
- \* Diffusion Tensor MRI Predictors of Cognitive Impairment in Confluent White Matter Lesion
- \* Lanthanide-impregnated molecularly imprinted polymer microspheres as antibody mimics on an optofluidic platform for the detection of disease biomarkers
- (2009) \* Terahertz probe for in vivo imaging
- \* Signal Processing Strategies on Cochlear Implant Devices for Effective Speech Perception of Tonal Languages
- \* Development of A Robotic Endoscope Holder for Nasal Surgery

---

The following reports are enclosed in “General Report and Research Highlights 2009-2011” printed in October 2011.

**Completed Projects**

- (2008) \* Development of highly sensitive and large throughput surface

**Completed Projects**

- |        |  |
|--------|--|
| (2008) | enhanced Raman scattering (SERS) substrates for molecular diagnosis  |
| (2007) | * Research on Language and Brain Waves<br>* Development of an Efficient Locomotion Mechanism for Wireless Active Capsule Endoscope<br>* Bio-electromagnetic Modeling and Experiment Setup for Medical Electronics RF Safety Assessment<br>* Medical Applications of Terahertz Imaging<br>* Hybrid Assistive Knee Braces with Smart Actuators |
| (2006) | * RF Radiation Effect and Efficiency of Wireless Medical Devices on Human Body<br>* Photonic biosensor micro-arrays for screening of common cancers  |
- 

The following reports are enclosed in “Research Highlights 2005-2007” printed in January 2008.

**Completed Projects**

- |        |  |
|--------|--|
| (2005) | * Cochlear Implants<br>* Virtual Anatomy and Dexterous Simulators for Minimal Access Cardiothoracic and Neuro-endoscopic Surgeries<br>* Systematic Synthesis of Nano-informatics Chips by Nano-Robotics Manipulation |
|--------|--|

*(Funded Year)*

## DEVELOPMENT OF A NOVEL ROBOTIC MANIPULATOR FOR CONFINED SPACE SURGERY

Principal Investigator: Professor AU, Kwok Wai Samuel  
*Department of Mechanical & Automation Engineering, CUHK*

**Project Start Date: 1 July 2017**



### ABSTRACT

Minimally Invasive Surgery (MIS) has been widely adopted in many surgical specialties. Still, for some hardly accessible anatomical regions, only limited options of MIS can be offered by physicians. Accessing these regions often require surgical tools passing through tortuous natural orifices. Yet, existing surgical instruments are predominantly straight and rigid with limited surgical capabilities. Flexible robotic instruments are believed to be the technological pathway to address this significant clinical problem. Although substantial progress has been made, existing flexible instruments still lack synergy among the core surgical enablers including the instrument accessibility, size, and surgical functionalities.

The objective of this project is to develop a novel flexible robotic manipulator for MIS. In this project, a flexible instrument/manipulator with a complex continuum spline will be designed and fused with an elastomer outer sheath and metal braided reinforcement. A flexible Fiber Bragg Grating (FBG) sensor will also be embedded into the spline to measure the distal configuration for feedback control. Like human-musculoskeletal system, this hybrid approach can provide exceptionally high axial stiffness and torsional resistance through the spline, as well as large internal lumen to carry tools without sacrificing instrument bendability and dexterity. The elastomer sheath enhances the structural integrity and torsional resistance. Different quantitative models will be studied to understand the mechanical and dynamic properties of flexible instruments with complex internal structures. The results of the project will lead us to create a systematic, model-based design approach for flexible instruments, as well as practicable, dynamic models that can be used for simulations and controller design. Experimental prototypes will be designed and fabricated. Experiments will be carried out to validate the overall performance and robustness. This research initiative will enable complex surgery in hardly accessible anatomical regions, allowing more patients benefiting from minimally invasive treatment.

### INNOVATION AND PRACTICAL SIGNIFICANCE:

Although substantial progress has been made, existing flexible instruments still lack synergy among the core surgical enablers including the instrument accessibility, size, and surgical functionalities. The success of this project will provide a new mechanical and control framework for the development of robotic instrument that is capable of overcoming these limitations. This innovative robotic system enables surgeons to provide more accurate, effective, and less invasive procedure

even for the complex cases such as skull base surgery, which are currently difficult to treat even with the state-of-the-art robotically assisted surgery. The proposed technology can also allow more patients suitable for and can benefit from MIS in these anatomical regions, ultimately, improving the quality of life of patients

### **PROJECT OBJECTIVES:**

- Design and fabricate a high performance flexible robotic manipulator. Key Issues: Superior functionality demands exceptional axial stiffness and structural integrity, which cannot be accomplished by existing flexible instrument designs. Possible Outcomes: A high performance flexible robotic manipulator will be delivered, that can provide exceptionally high axial stiffness and torsional resistance, as well as large internal lumen to carry tools without sacrificing instrument bendability and dexterity.
- Develop kinematic and dynamic models for the proposed design. Key Issues: Lack of a systematic, model-based design approach for complex flexible instruments. Possible Outcome: The results will lead us to create a systematic, model-based design approach for flexible instruments, as well as practicable, dynamic models that can be used for simulations and controller design.
- Develop a robust, closed-loop controller for instrument control, based on the fusion of the measurement of the distal FBG sensor, proximal motor encoder, and cable tension. Key Issues: Precise control of flexible instrument is uncommon due to the undesired instrument characteristics. Possible Outcome: A control framework will be developed that allows us to achieve high performance servo control as well as stable interaction with environment.
- Conduct experiments to validate the overall manipulator performance and robustness.

## DEVELOPMENT OF AN INERTIAL MICROFLUIDICS BASED APPROACH FOR THE ISOLATION OF MITOCHONDRIA FROM BIOLOGICAL SAMPLES

Principal Investigator: Professor Megan Yi-Ping HO  
*Department of Biomedical Engineering, CUHK*

**Project Start Date: 1 July 2017**



### ABSTRACT

This project aims to develop a novel approach to rapidly isolate mitochondria from samples of clinically relevant sizes. While currently available methods are mostly laborious and not suitable for small-scale analyses in the clinics, the proposed approach is able to handle 200 microliters of sample and process the isolation within 30 minutes. Aside from the possibility for small-scale analysis, the proposed approach offers many distinct features, including the simple procedures, undemanding equipment request, minimal damages to the isolated mitochondria, and continuous batch processing. Possibilities to analyse mitochondria from a limited amount of clinically relevant patient samples are expected to expand our knowledge towards the basic biological mechanisms of mitochondrial function, and to elucidate how mitochondria are involved in the development of diseases such as cancers, premature aging syndromes, diabetes and neurodegenerative disorders. For instance, it becomes practical to obtain mitochondria from the patient samples, and to elucidate how defective mitochondria link to the mitochondria-associated diseases. Furthermore, the isolation principle may be tailored for an array of subcellular fractions, rendering more efficient identifications and characterizations of intracellular organelles of interest and, consequently, advancing the study of biology and medicine continuously.

### INNOVATION AND PRACTICAL SIGNIFICANCE:

Defective mitochondria have been linked to several important human diseases, that urgently calls for the fundamental understanding of the disease mechanisms. To this end, presented here is a previously unavailable strategy enabling a fast and cheap isolation of mitochondria from samples of clinically relevant sizes. The proposed technology is revolutionary, yet highly transformable to a commercial product for routine clinical investigations and biological studies. Therefore, the developed platform will have a broad appeal to the pharmaceutical and clinical sectors targeting mitochondrial diseases. Table 1 summarizes the practical cost and expected performance for the isolation of mitochondria using the inertial based approach compared with other commercially available kits.

**Table 1. Comparison between the Inertial Based Isolation of Mitochondria and the Commercially Available Kits.**

	<b>Inertial Based</b>	<b>Thermofisher</b>	<b>Abcam</b>	<b>Qiagen</b>
<b>Assay Time (Post-Lysis)</b>	10 min	40 min	>30 min	>45 min
<b>Required Cells</b>	100	$2 \times 10^7$	$4 \times 10^7$	$5 \times 10^6$
<b>Bench Top Availability</b>	Yes	Yes	Yes	Yes
<b>Purity</b>	High	High	High	High
<b>Required Reagent Exchange</b>	No	Yes	Yes	Yes
<b>Price Per Isolation (HKD)</b>	20	45	97	296

**PROJECT OBJECTIVES:**

1. To optimize and fabricate the inertial microfluidic chip for the isolation of mitochondria.
2. To demonstrate effective recovery of mitochondria using purified mitochondria as a model.
3. To develop a series of protocols for the characterization of isolated mitochondria.
4. To revise the design chip for a rapid isolation of functional mitochondria from crude human cell lysates of a clinically relevant sample size.

# AN MRI-GUIDED ROBOTIC SYSTEM FOR BREAST BIOPSY

---

Principal Investigator: Professor David Navarro-Alarcon/ Professor Yun-Hui LIU  
*Department of Mechanical and Automation Engineering, CUHK*

Co-Investigator (if any):

Yun-hui Liu<sup>(1)</sup>, Defeng Wang<sup>(2)</sup>, Hayley Louise Chung<sup>(3)</sup>,  
 Terrance Chan<sup>(4)</sup>

Research Team Members:

Satwinder Saini<sup>(1)</sup>, Man Kiu Chow<sup>(1)</sup>, Henry Ng<sup>(1)</sup>, Tianxue Zhang<sup>(1)</sup>

<sup>(1)</sup>Dept. of Mechanical and Automation Engineering, CUHK

<sup>(2)</sup>Dept. of Imaging and Interventional Radiology, CUHK

<sup>(3)</sup>Time Medical Systems Ltd.,

<sup>(4)</sup>North District Hospital



**Reporting Period: 1 July 2016 – 30 April 2017**

## ABSTRACT

Breast cancer is the most common cause of cancer mortality in women in the world. To determine whether a growth of breast tissue is cancerous or not, a biopsy is conducted to extract and analyse sample cells from the suspicious area. In this research project we aim to develop a new robotic system which can accurately insert the biopsy needle into the target lesion. The trajectory of the robot is guided with real-time visual feedback from a magnetic resonance imaging (MRI) scanner. To operate the robot inside the scanning room, the mechanical structure of the robot is fabricated with non-magnetic materials such as aluminium and nylon, and a combination of pneumatic and piezoelectric actuators are used to drive the motion of the mechanism. Compared to the traditional manual biopsy, the proposed robot has the potential to considerably improve the accuracy, shorten the overall procedure's time, and reduce the trauma inflicted to the tissues.

## 1. OBJECTIVES AND SIGNIFICANCE

**Objective:** In China, 187,000 breast cancer cases were diagnosed in 2012, accounting for nearly 12% of the whole world new cases. To improve the disease's survival rate, it is important to accurately detect cancerous growths in early stages by performing a breast biopsy. This procedure is usually conducted in a minimally-invasive manner by a radiologist that inserts a biopsy needle into the tissues and guides it with some imaging modality such as MRI. Our aim in this project is to develop a robot which can insert the biopsy needle into the tissues; our main idea is to develop a system that can be guided with real-time images from the MRI scanner.

**Significance:** In traditional MRI-guided biopsy, the radiologist first scans the patient to get a diagnosis image, which he/she uses to estimate the lesion's position and then to insert the needle. A second scan is performed to corroborate the location, which if deviated from the target, further adjustments/scans are performed; this results in a repetitive and time consuming process. To cope with this problem, we propose to build a robot to automate the needle insertion. The novelty of this robot is its capability to operate within the scanner's bore. This innovative feature will allow radiologists to considerably reduce the procedure's time and cost. We hope that this university-industry collaboration will also greatly improve the chances for commercialisation of the obtained research outputs.

## 2. RESEARCH METHODOLOGY

### 2.1 Design Requirements

There are several design requirements that must be taken into consideration when developing this type of system, these include: (1) satisfying the scanner's dimensional constraints, (2) selecting non-magnetic materials and actuators, (3) adapting electronics to avoid visual artifacts. In our model we consider the dimensions of a Time Medical PICA scanner. Fig. 1 shows the proposed set-up, which requires the robot to have a vertical height smaller than 220 mm, and a width smaller than 400mm. The required linear motion range to perform a biopsy is  $[x, y, z] = [130, 90, 50]$  mm.

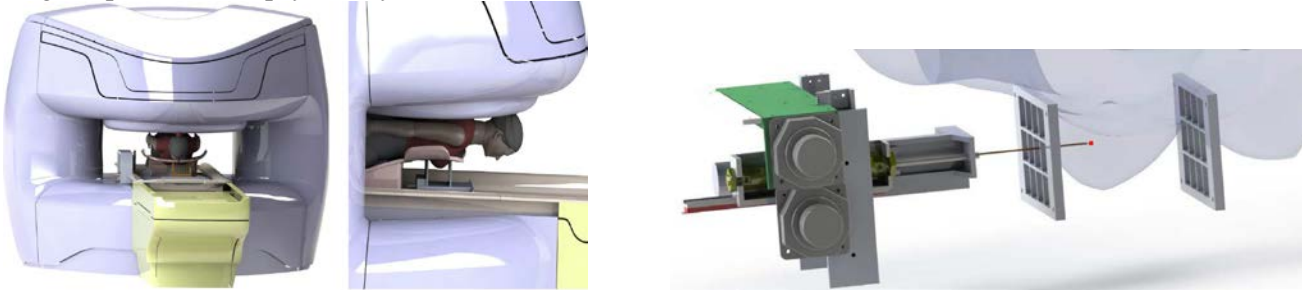


Fig. 1. (left) Conceptual MRI-guided biopsy set-up. (right) Needle insertion using the grid method

### 2.2 Proposed Mechanical Structure

To fulfil the above given design requirements, we propose to develop a robot consisting of three active linear joints for needle positioning and insertion motions. This 3-DOF design is intended to replicate the linear motions of a manual biopsy using the grid method. Fig. 2 conceptually depicts the details of proposed 3-DOF mechanism. To achieve stable motion, non-magnetic slides (made of aluminium, silicon nitride, graphite) are used on each active axis. An aluminium power screw with a nylon nut is used in the x-axis to transmit motion from actuator to the joint. Two parallel slides provide stable support to the biopsy gun from both sides; this vertical axis uses a brass rack and pinion to transmit the motion from the actuator to the joint.

The first two DOF of this system serve to align the needle's axis with the target lesion; these joints are driven by piezo-electric motors. To measure the robot's configuration, position sensors are embedded in all three joints. The mechanism that drives the needle is actuated by a double-acting pneumatic cylinder. The insertion mechanism is attached to the parallel slides of the vertical axis to provide support to the biopsy gun from both sides. The axis' slide has a linear travel range of 75 mm, which is used for providing smooth pushing/pulling motions to the piston rod. To perform the task, the cylinder must generate a pushing force of at least 3 N (a recent clinical study reports that a maximum force of 2.3 N is required to penetrate breast tissues). The pneumatic cylinder under consideration has piston areas of  $A_1 = 67.5 \times 10^{-6} \text{ m}^2$  and  $A_2 = 59.5 \times 10^{-6} \text{ m}^2$  and maximum chamber pressure of  $p_1 = 340000 \text{ pa}$ . By setting an opposing pressure of  $p_2 = 100000 \text{ pa}$ , we calculate that the cylinder has a maximum pushing force of  $f = A_1 p_1 - A_2 p_2 = 17 \text{ N}$ , which is sufficient to penetrate the tissues with the needle.

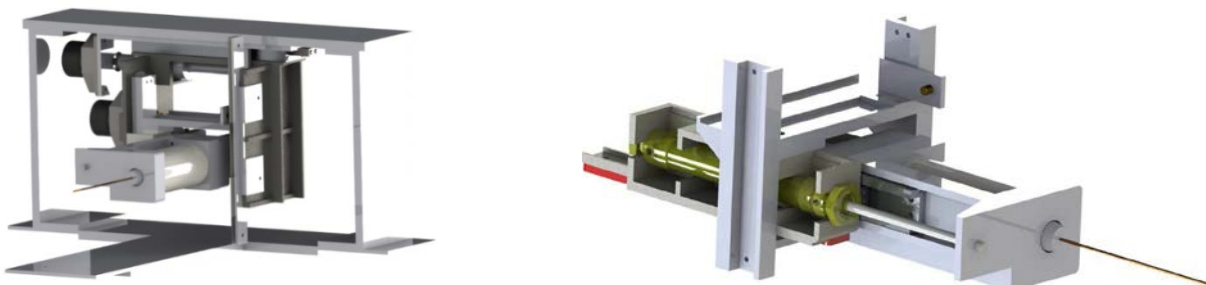


Fig. 2 (left) Conceptual model of the 3-DOF robot. (right) Details of the insertion mechanism

### 2.3 Motion Control System

The control system is composed of three servo modules: a stage positioning controller, a pneumatic regulator,

and a needle insertion controller. The piezo-motors that drive the x-y joints are used for initial needle positioning; these motors come with its own motion controller, current amplifier, and a feedback sensor. A pair of pressure regulated valves are used for driving the motion of the cylinder. To accurately regulate the cylinder's chamber pressure, two pressure sensors are installed in close proximity to the ports. A position sensor measures the linear displacements along the needle's insertion joint. In our system, we use pneumatic actuation to drive the needle as it presents the best performance for continuous MRI.

## 2.4 Adaptive Controller Design

The pneumatic valves used in our system can control the pressure being output to the cylinder; this pressure is directly proportional to the reference voltage. To drive the pneumatic cylinder, long tubing lines (of around 6 meters in our set-up) must be passed into the room through the panel's wave guides. Due to the long tubing length, the pressure commanded by the valves may differ from that inside the cylinder's chambers, here denoted by  $p$ . This situation can be fairly modelled by the following first-order system:

$$\delta p / \delta t = -H(p - d - u)$$

where  $d$  models the steady-state deviation from the control reference  $u$ ; the parameter  $H > 0$  determines the response of the chamber. To control the chamber's pressure, we propose the following adaptive regulator:

$$u = p_d - \hat{d}; \delta \hat{d} / \delta t = kH(p - p_d)$$

for  $p_d$  as the desired pressure,  $\hat{d}$  as the adaptive state, and  $k$  as a feedback gain. The above controller can asymptotically regulate the chamber's pressure. By computing the time derivative of the Lyapunov function

$$V = (|p - p_d|^2 + |\hat{d} - d|^2 / k) / 2$$

we can show that  $\delta V / \delta t = -H|p - p_d|^2$ , which clearly proves the stability. To command the pushing forces, we use the force-pressure relation  $f = A_1 p_1 - A_2 p_2$ , which allows us to solve  $p_{di}$  from a desired force  $f_d$ . The chamber pressures for forward and backward motions are, respectively, computed as follows:

$$p_{d1} = (f_d + A_2) / A_1; p_{d2} = -(f_d + A_1) / A_2$$

## 3. RESULTS ACHIEVED SO FAR

### 3.1 The Fabricated Prototype

Fig. 3 shows the developed robotic prototype, which has an overall dimension of 400×220×260 mm. As we can see in this figure, the structure of the robot is mostly 3D printed. The rigidity of the mechanism is secured by reinforcing the x-platform with an aluminium plate (Al 7075), and by transmitting the x-y motions with an aluminium power screw and a brass rack and pinion. This figure clearly depicts the individual motions of the robot joints. This figure shows a simulated biopsy set-up, where we can see that the fabricated prototype is compact enough to perform lateral insertions inside the open bore scanner considered in our model



Fig. 3 (left) The fabricated robot prototype. (right) A simulated lateral insertion with a breast coil model

### 3.2 Closed-Loop Robot Performance

The performance of the pressure regulator is evaluated by commanding a target trajectory of  $p_{d1} = \sin(t/2)/2 + 2$ , while applying external disturbances to feedback pressure (these were introduced by manually pushing the cylinder's rod, thus altering the chamber's pressure). Fig. 4 (left) depicts the pressure tracking results, where D1 and D2 denote disturbances. We can see that our adaptive method can adaptively control the chamber's pressure while recovering from perturbations. We also tested the performance of the pneumatic positioning controller. For that we command the system to regulate the position of the needle with incremental steps of 25

mm. Fig. 4 (right) depicts the performance of our pneumatic-based needle positioning controller.

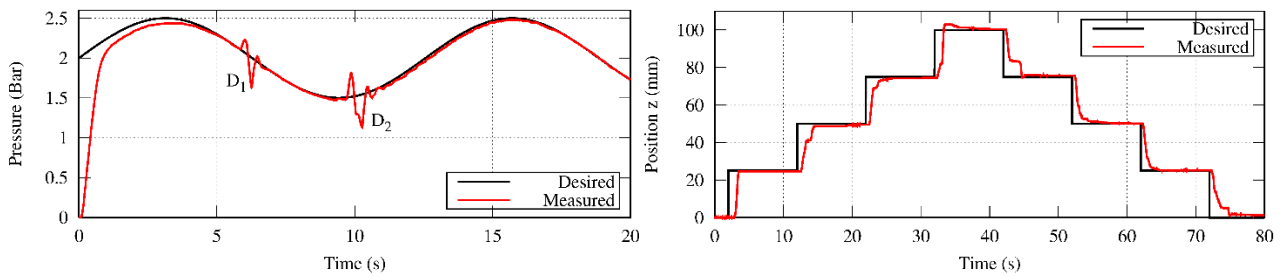


Fig. 4 (left) Trajectory tracking of the pressure controller. (right) Position regulation of the biopsy needle

### 3.3 MRI-Based Experiments

We experimentally evaluate the robot's performance and MR compatibility using a 0.2 T Time Medical Mona scanner, an MR head coil, and a silicon breast phantom tissue (see Fig. 5). For that, we first test the insertion performance into a breast phantom. Fig. 6 (left) shows the insertion distance estimated with the MRI scans; the system was required to insert the needle with 5 mm increments. Our results show an accuracy of  $\pm 0.4$  mm. Finally, we experimentally evaluate the signal-to-noise ratio (SNR) induced by the mechanism when located inside the scanner. We compare the SNR that is computed by imaging the phantom with and without the robot. Fig. 5 shows the obtained results.



Fig. 5 The scanner, head coil, and phantom tissue used for the MRI experiments

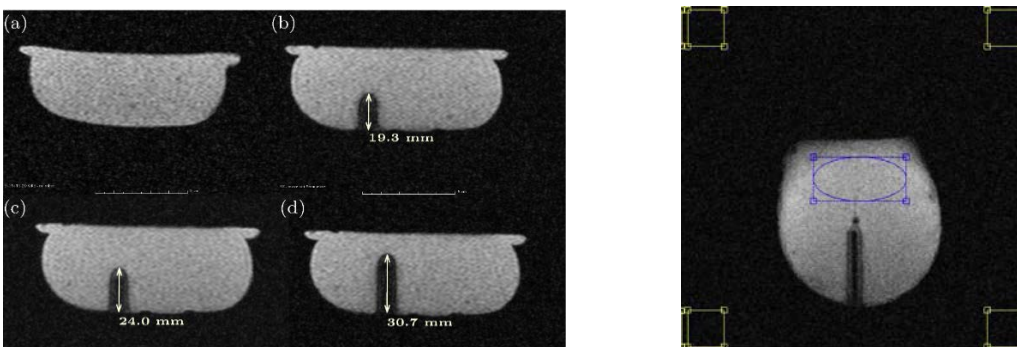


Fig. 6 (left) MRIs of the needle insertion. (right) MRI used for computing SNR of the robot

## 4. PUBLICATIONS AND AWARDS

- [1] D Navarro-Alarcon, S Singh, T Zhang, H Chung, KW Ng, MK Chow, YH Liu. Developing a Compact Robotic Needle Driver for MRI-Guided Breast Biopsy in Tight Environments. *IEEE Robotics and Automation Letters (RAL)*, vol. 2, no. 3, 1648–1655, 2017
- [2] T Zhang, D Navarro-Alarcon, KW Ng, MK Chow, YH Liu, H Chung. A novel palm-shape breast deformation robot for MRI-guided biopsy. *IEEE Int. Conf. on Robotics and Biomimetics*, pp. 527-532, 2016
- [3] F Zhong, D Navarro-Alarcon, Z Wang, YH Liu, T Zhang, HM Yip. Adaptive 3D Pose Computation of Suturing Needle Using Constraints from Static Monocular Image Feedback. *IEEE/RSJ Int. Conf. Intelligent Robots and Systems (IROS)*, 5521–5526, 2016

- [4] D Navarro-Alarcon and YH Liu. Contour-Based Deformation Servoing: A New Marker-Free Algorithm to Actively Deform Soft Objects into Desired Shapes with Manipulators. *IEEE Transactions on Robotics (TRO)*, under review, 2017 (under review)
- [5] KW Ng, MK Chow, D Navarro-Alarcon, S Singh, T Zhang, H Chung, YH Liu. Developing a Compact Robotic Needle Driver for MRI-Guided Breast Biopsy in Tight Environments. *IEEE/RSJ Int. Conf. Intelligent Robots and Systems (IROS)*, 2017 (under review)
- [6] S Singh, D Navarro-Alarcon, D Kwok, KW Ng, MK Chow, T Zhang, YH Liu. Towards Developing Benchmarking Indices for MRI-Compatible Robots: An Experimental Quantitative Study. *IEEE/RSJ Int. Conf. Intelligent Robots and Systems (IROS)*, 2017 (under review)
- [7] S Singh, D Navarro-Alarcon, MK Chow, KW Ng, T Zhang, YH Liu, H Chung. Can a Tesla Turbine be Utilized as a Pneumatic Actuator for MRI Interventions? *Journal of Mechanism and Machine Theory*, 2017 (under review)

# INTENTION-DRIVEN SHOULDER REHABILITATION FOR TARGETED NEURO-MUSCULAR TRAINING USING AN EXO-MUSCULOSKELETAL ROBOT

---

Principal Investigator: Professor Darwin Tat Ming LAU  
*Department of Mechanical and Automation Engineering, CUHK*

Co-Investigator (if any):  
 Prof. Raymond Kai Yu Tong <sup>(2)</sup>

Research Team Members:  
 Dr. Ghasem Abbasnejad <sup>(1)</sup> (postdoctoral fellow)

<sup>(1)</sup>Dept. of Mechanical and Automation Engineering, CUHK  
<sup>(2)</sup>Dept. of Biomedical Engineering, CUHK



**Reporting Period: 1 July 2016 – 30 April 2017**

## ABSTRACT

This project aims to develop an intention-driven rehabilitation robot for muscle-specific training of the human shoulder. By designing a cable-actuated exoskeleton where the cables are arranged to match the wearer's anatomy, the effectiveness of targeted neuromuscular training of the shoulder muscles will be explored through a pilot study involving both healthy human subjects and stroke patients.

Current rehabilitation robots have two noteworthy features. First, such robots provide assistance only in producing gross motion rather than assistance to the individual muscles. Second, an assist-as-needed (AAN) approach is used where more assistance will be provided if the patient is unable to complete a desired task themselves. The proposed device will aim to address the shortcomings resulting from these features. In recent years, a promising alternative to the AAN is intention-driven rehabilitation (IDR), where the assistance provided to the patient is proportional to the strength of their neuromuscular signals in order to train their ability to generate stronger signals. This approach has already been shown to be effective for simpler joints such as the elbow and wrist, but has not yet been studied for more complex joints such as the shoulder.

During the first reporting period of the project, three main tasks were completed: 1) the development of prototype of the exo-muscular robot; 2) integration of EMG sensors into the system to detect user intention; and 3) preliminary testing on healthy human subjects to show the validity of the prototype and methods.

## 1. OBJECTIVES AND SIGNIFICANCE

1. Develop a prototype of a wearable exo-musculoskeletal rehabilitation robot actuated by cables:
  - a) Arrange the robot cables anatomically to actuate in parallel six of the major shoulder muscle groups: *pectoralis major*, *deltoid*, *teres major*, *teres minor*, *infraspinatus* and *supraspinatus*.
  - b) Allow the system to be attached to the person's upper arm conveniently, to be worn comfortably and the attachment locations of the cable to be easily rearranged.
  - c) Capable of providing assistance to a healthy person to carry an extra load in addition to the weight of their arm.
  - d) Implement intention-driven control of the exo-muscles through electromyography (EMG) signals that are attached onto the surface of the arm (non-invasively).
2. Demonstrate the potential of intention-driven muscle-specific training through three pilot studies:
  - a) The preliminary pilot study will consist of 10 healthy human subjects, each using the

developed system for 10 x 30 minute training sessions to demonstrate the effects of muscle-specific training by only providing assistance to particular muscles of the system.

b) Compare the effectiveness of intention-driven rehabilitation (IDR) with the assist-as-needed approach (AAN) performed on another group of 10 healthy human subjects.

c) Finally, a pilot study of the system will also be performed on a group of 15 stroke patients.

Shoulder pain and impairment is a severe problem that affects the quality of life of the impaired subject and inhibits the motion of the arm even in performing even simple daily tasks, such as reaching for objects and feeding one self. Causes of such impairments include stroke, muscle weakness and shoulder subluxation (instability of the shoulder). Furthermore, shoulder subluxation is a common cause of pain for post-stroke patients (between 16-72% of stroke patients). The treatment of such impairments places significant burden on the health system. Successful completion of this project is expected to provide a new approach for performing effective shoulder training to patients with shoulder pain and impairment. Effective treatments would not only improve the quality of life of the patient and also decrease the burden on the Hong Kong health system.

## 2. RESEARCH METHODOLOGY

In the proposed project, an exo-musculoskeletal IDR robot for the shoulder will be developed. The cables will be arranged in parallel to the subject's muscles and will provide assistance to a particular muscle group. Using EMG feedback, an intention-driven scheme will be employed to perform muscle-specific training. The proposed project combines experiences of cable-driven robot development and musculoskeletal analysis skills of the PI with the experiences in intention-driven rehabilitation of the co-I. The research plan will consist of three main tasks: 1) design and prototype of the exo-musculoskeletal robot; 2) intention-driven control using EMG; 3) pilot study on healthy subjects to demonstrate the effectiveness of this method.

### I. Design and prototype of the exo-musculoskeletal robot

In this project, the PI proposes to develop a new type of exo-musculoskeletal robot that has cables arranged in an anthropomorphic manner. Six muscle groups identified as the major contributors to shoulder motion and are also situated closer to the surface will be used to design the arrangement of cables for the robot: the *pectoralis major*, *deltoid*, *teres major*, *teres minor*, *infraspinatus* and *supraspinatus*.

The cable actuators that will be used in the proposed prototype are the *Myomuscle* units developed by the Myorobotics project consortium who the PI collaborates with. In the design and development of the system, the robot should: be easy to attach onto the patient and wear, allow for reconfiguration of the pulley locations on the frame such that cables can be arranged to be in parallel with the muscles, and be safe for the subject to use given the high maximum cable force of the myomuscles.

The arrangement of cables in an anthropomorphic manner is one of the keys to allow the system to provide targeted muscle-specific training. By arranging cables in parallel to specific muscles, the force applied to a particular cable can be controlled to promote strengthening of the corresponding muscle. This is a key difference between the proposed system and existing rehabilitation robots that only assist in producing the gross motion.

### II. Intention-driven control using electromyography (EMG) signals

After the development of an initial prototype, the intention-driven control system for the exo-musculoskeleton will be implemented and tested. With the co-I's experience in EMG and IDR control, the placement of the EMG electrodes such that signals from the six muscle groups can be obtained will be properly considered. These signals will be used to control the cables through a simple intention-driven scheme, where

$$\mathbf{f}(t) = K_p \mathbf{V}_{EMG}(t) \quad (1)$$

The vector  $\mathbf{V}_{EMG}$  contains the EMG readings and  $\mathbf{f}$  is the forces that the cables should execute. The gains  $K_p$  correspond to the amount of assistance after considering the effort from the subject. As observed in [16], it is anticipated that the IDR approach will promote the subject to improve their neurological signal and muscle training in order to complete the set task, for example, the lifting motion of the arm.

### III. Pilot study of the exo-musculoskeletal robot on healthy subjects

To verify the effectiveness of the developed rehabilitation device and intention-driven control system, three studies will be performed. In the first study, a group of 10 healthy human subjects will use the exo-musculoskeletal robot to assess the effects of IDR on the shoulder. Each subject will use the robot for 10 sessions of 30 minutes per session. During these sessions, the subject would be required to perform a designed set of shoulder motion trajectories, ranging from the basic motions such as flexion/extension, adduction/abduction, and internal/external rotation, to more general trajectories. The trajectories will be selected to allow the activation of different muscle groups to be observed. During each of the sessions, the EMG signals, cable forces and kinematic trajectory of the motion will be recorded. This data allows the analysis of whether the IDR approach trains specific muscles when different trajectories are being performed.

In the second study, another group of 10 subjects will use the AAN control approach for the same set of exercises. This study serves to compare the IDR and AAN methodologies on the same robotic rehabilitation system to gain a better understanding on the effectiveness of the two approaches. Such a comparison has not been done within the literature to the best of the team's knowledge.

In the final study, the proposed device will be tested on a group of 15 stroke patients, again for 10 x 30 minute sessions. The selection criteria for the subjects are: first stroke with unilateral lesion in the chronic stage (that is, more than 6 months after stroke). Such patients would already have a stable condition and no significant improvements are normally expected. This would allow the effects of the developed device to be more clearly observable. Note that the subjects for all three studies must be above the age of 18.

### **3. RESULTS ACHIEVED SO FAR**

In the initial phase of the project, progress has been primarily focused on tasks 1 and 2 from the research methodology, and preliminary work in task 3 has also been undergone. The progress will be described in three sections: 1) mechanical prototype; 2) EMG-robot integration; and 3) preliminary human subject experiments.

#### **3.1. Mechanical Prototype Development**

In the first 6 months of the project, the prototype of the current exo-muscular robot (Figure 1) was completed. This prototype was reached to after six design iterations and trials. The current prototype possesses three muscle groups, the deltoid anterior, deltoid middle and deltoid posterior (as shown in Figure 1c).



*Fig. 1. Exo-muscular robot prototype. Overall view (left), front view (middle) and side view (right).*

The three muscles, deltoid anterior, middle and posterior, are involved primary in the shoulder flexion, abduction and extension, respectively. Figure 2 shows the motion produced by the robot on the subject by providing cable force actuation to each of the muscles, demonstrating the capability of the exo-muscle robot to motion that is similar to that of the corresponding muscles they are parallel to. Using the Myomuscle cable actuator units, integration with the ROS cable robot software (ROS-CASPR) developed by the PIs lab is completed in order to command the exo-muscles. In conclusion, during the first report period, the concept and design of the robot has been essentially completed with three muscles demonstrated. The next step is to attach additional exo-muscles to other muscles of the shoulder, such as the pectoralis major and teres major/minor.



*Fig. 2. Flexion (left), abduction (middle) and extension (right) motions of the shoulder produced through the robot prototype using the Myomuscle actuator units*

### **3.2. EMG integration with the robot**

The robot prototype (presented in the above section) can be controlled in two modes: 1) manual command input; and 2) EMG IDR feedback. The manual command input scheme was achieved through potentiometer dials that command each muscle (Figure 3 (left)). This mode is primarily used for testing and calibration. The main mode to be used within the IDR scheme is the EMG sensor feedback from the corresponding muscles that have exo-muscles attached. The EMG sensors, as shown in Figure 3 (right), record the electrical activity of the muscles and then send this information to the ROS software framework. This is then used to provide the actuation command for the corresponding muscle through the proposed scheme in (2).

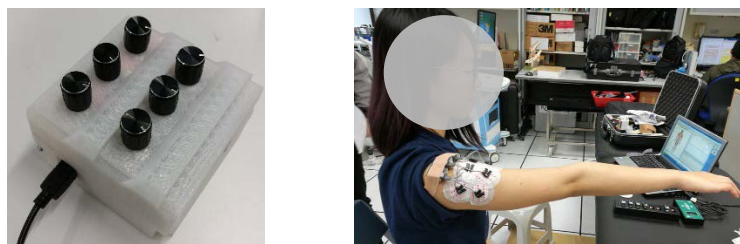


*Fig. 3. Command mode of robot: 1) potentiometers dials for each muscle (left); 2) EMG on muscles (right)*

Within this task, an appropriate calibration methodology for each muscle was developed. This involves the recording and determination of EMG range and calibrate sensors such that there is no over-saturation and that the required operating EMG range can be measured. The successful EMG integration with the robotic system was demonstrated through a teleoperation experiment. In the experiment, one subject wore the EMG sensors while another wore the robot system, and the detected EMG signals are used to actuate the wearer of the robotic system, while the wearer remains relaxed. Results of the experiment showed that EMG detection in muscle and shoulder motion intention was successful and the produced corresponding motion to the wearer of the exo-muscle robot.

### **3.3. Preliminary Human Subject Experiment**

Preliminary human subject experiments were performed in order to demonstrate the working principles and confirm the potential of the proposed approach. These experiments were performed on three healthy subjects. In this experiment, each subject wore both the EMG sensors and robot, in the same manner as would be expected during the rehabilitation, and the subject were asked to perform shoulder flexion, abduction and extension motion while carrying different amount of weights. The EMG signals on the shoulder muscles were then recorded both with and without the exo-muscle robot assistance for a fixed intention-assistance gain. As shown in Figure 4, it can be clearly observed that the robot assistance using the IDR scheme produced lower measured EMG, indicating that lower muscle forces were required. Consequently, this supports the idea that using the same EMG strength, the wearer would be capable of carrying a heavier load. This validation is important later experiments with impaired subjects as it demonstrates that the robot would be capable of providing additional force during their therapy through the IDR scheme. In the remaining time of the project,

additional experiments on a wider range of healthy and stroke patient subjects will be aimed to be performed.

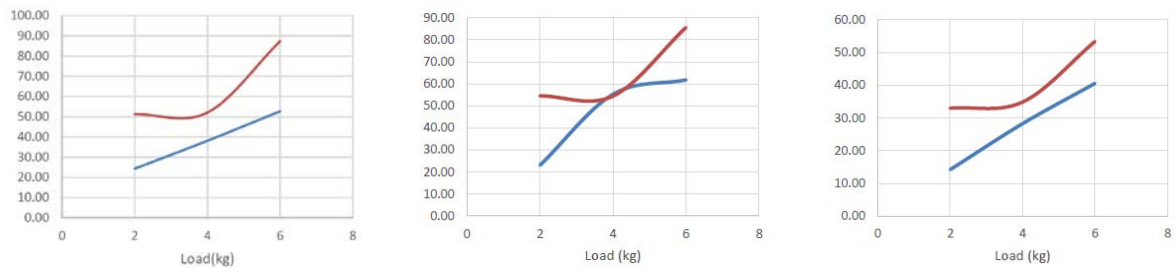


*Fig. 4. Summary of human experiments. Load vs EMG reading without robot (red) and with robot (blue). Anterior for flexion motion (left), middle for abduction (middle) and posterior for extension (right).*

#### **4. PUBLICATION AND AWARDS**

Two final year projects from the MAEG programme and the BME programme were involved in this project. They were primarily involved in the system design and their project was awarded the 1<sup>st</sup> runner up of the CUHK Charles K. Kao Student Creativity Award for the individual entry. Furthermore, we are now preparing a publication to be submitted to the IEEE Transaction on Robotics (leading journal in robotics).

# ENGINEERING ANTIMICROBIAL SURFACES BASED ON MICRO-TOPOGRAPHY USING A NOVEL ULTRASONIC MACHINING METHOD

---

Principal Investigator: Professor Ping GUO  
*Department of Mechanical and Automation Engineering, CUHK*

Research Team Members:

Yang Yang, PhD student <sup>(1)</sup>, Hanheng Du, Research assistant <sup>(1)</sup>  
 Meiyu Liu, Research assistant <sup>(1)</sup>

<sup>(1)</sup>Dept. of Mechanical and Automation Engineering, CUHK



**Reporting Period: 1 July 2016 – 30 April 2017**

## ABSTRACT

There are great demands of antimicrobial surfaces, which could prevent the adhesion of micro-organisms and the formation of biofilms. Microbial contamination of surfaces, which are directly exposed to human tissues (surgical equipment) and food (utensils), can cause serious infection and the associated disinfection costs. Biomedical implants, such as prosthetic devices and artificial joints, are subjective to adhesion of pathogenic bacteria and biofilms, which not only significantly reduce the lifespan of the implants but also increase the risks of various infections. Biofouling on marine vessels of barnacles and algae is a great concern in shipping industry due to corrosion to the ship hulls and increased fuel and maintenance costs.

The project aims to develop a novel manufacturing process for fast creation of micro-structured surfaces for the antimicrobial surfaces application directly on stainless steel and titanium alloy surfaces which are mostly widely used in the hospitals, food industry, and biomedical market. The outcome from this project will enable the creation of antimicrobial surfaces based on surface micro-topography, which is non-toxic, permanent and chemical free, to be applied to the related applications in hospitals, biomedical implants and devices, food packaging, marine industry, etc.

## 1. OBJECTIVES AND SIGNIFICANCE

1. The research project, if carried out successful, will enable the technology to create antimicrobial surfaces, which could prevent the adhesion of bacteria and formation of biofilms, in many critical applications, such as surgical equipment, biomedical devices and implants, and food packaging.
2. The project aims to develop a novel manufacturing process for fast creation of micro-structured surfaces for the antimicrobial surfaces application directly on stainless steel and titanium alloy surfaces which are mostly widely used in the hospitals, food industry, and biomedical market.
3. The project aims to systematically study and test the surface micro-topography and its effects on the prevention of microbial adhesion. The surface wettability and an innovative surface roughness engineering index will be utilized as the criteria to categorize different surface micro-features.
4. The project aims to carry out experiments to produce various micro-patterned stainless steel and titanium surfaces according to the optimized results from our model. These antimicrobial surfaces will then be tested to verify their retention ability of different micro-organisms.

## 2. RESEARCH METHODOLOGY

The research project, if carried out successful, will enable the technology to create antimicrobial surfaces, which could prevent the adhesion of bacteria and formation of biofilms. There are three main research tasks in

this project, namely, (1) development of the ultrasonic texturing system for creating micro-structured surfaces; (2) study of the relationship between surface micro-topography and its effects on microbial retention; (3) to generate various micro-patterned surfaces to test against smooth/polished surfaces.

In order to make the micro-structured surfaces effective against microbial attaching, the feature size must be reduced to be comparable to the size of targeted micro-organisms, which is in the range of 1-5  $\mu\text{m}$ . The previously developed ultrasonic texturing system by our group was used to create features in tens of microns for the friction reduction application. The system will be adapted to control the trajectory of the cutting tool to create more specific surface patterns. The same vibration texturing principle will be utilized but a new non-resonant tool will be designed and adopted to achieve higher precision as shown in Figure 3(c).

While it is commonly accepted that the microbial adhesion responds to the surface topography, the intrinsic mechanisms are yet to be fully understood. Some think surface roughness ( $R_a$ ) is a key parameter to the effectiveness of microbial retention, but some works suggest otherwise. The surface roughness is good to characterize a surface with random or simple surface features, but it cannot fully describe the complex patterns. In this project we take two parameters to hypothetically characterize the effectiveness of surface topography on microbial retention. One is the wettability or contact angle of surfaces; the other is engineering roughness index proposed by Schumacher et al.

We will design and optimize the surface topography based on the surface wettability, engineering roughness index, and the capability of our texturing system. These patterns will be directly machined on stainless steel and titanium surfaces, which are most widely used in hospitals and biomedical related devices. Experiments of their effectiveness on microbial retention will be tested using different micro-organisms to compare with smooth and untreated surfaces.

### 3. RESULTS ACHIEVED SO FAR

#### 3.1 Design and manufacturing of anti-fouling surfaces

The settlement of chlorella is mainly influenced by the feature size, geometry, and roughness of the engineered surface. For a more comprehensive description of the relationship between these factors and the adhesion density, engineered roughness index (ERI) is developed.

$$ERI = (r * df) / f_D$$

The ERI consists of three variables associated with the size, geometry, and spatial arrangement of the topographical features: Wenzel's (1936) roughness factor ( $r$ ), depressed surface fraction ( $f_D$ ), and the degree of freedom for movement ( $df$ ). These values are based on the preferential settle tendencies of *Ulva* spores and the hypothesis that increasing the tortuosity of surface topography will make the surface less favorable for settlement. This formula indicates that an interaction exists between roughness measures and feature spacing that must be considered when designing topographic surface.

Chlorella prefer to squeeze along the recessed area with the surface topography and seldom bridge between the features within the repeat unit. So, the width of recessed area between features is better smaller than the diameter of chlorella (3 – 10  $\mu\text{m}$ ).

However, there is still a lower number of chlorella were observed on the protruded features, leaning against the edge of the triangle feature, instead of settling on the flat top surface. So the protruded feature can be in larger size. According to these regulars, we choose two different patterns to carry out the experiments as shown in Figure 1 and Figure 2.

(1)  $df = 1$

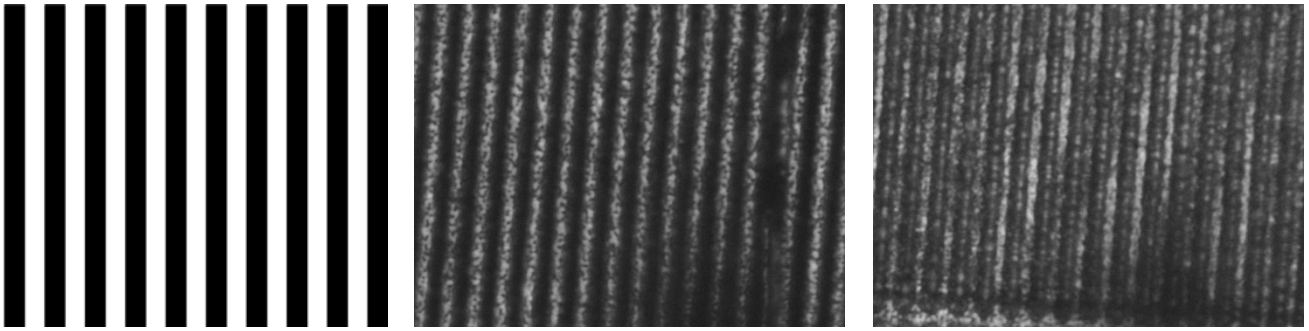


Figure 1. Designed channel patterns with degree of freedom of 1: designed patterns and laser machined patterns.

(2)  $df = 2$

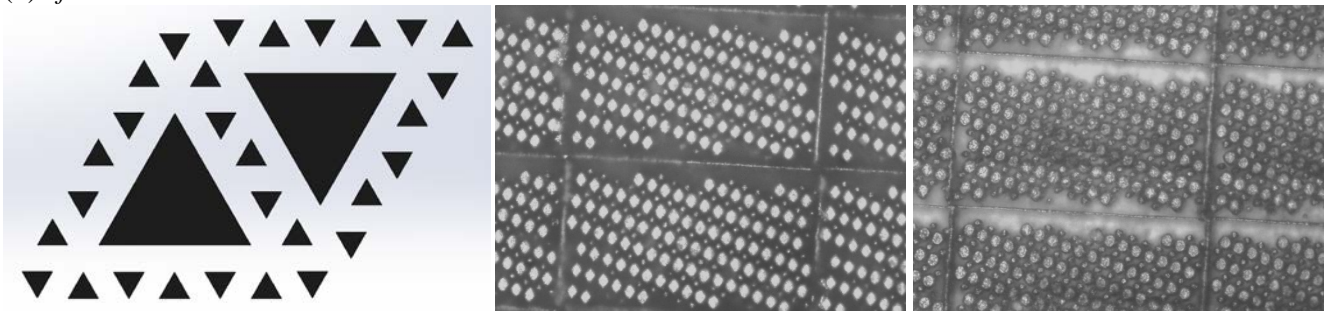


Figure 2. Designed diamond patterns with degree of freedom of 2: designed patterns and laser machined patterns.

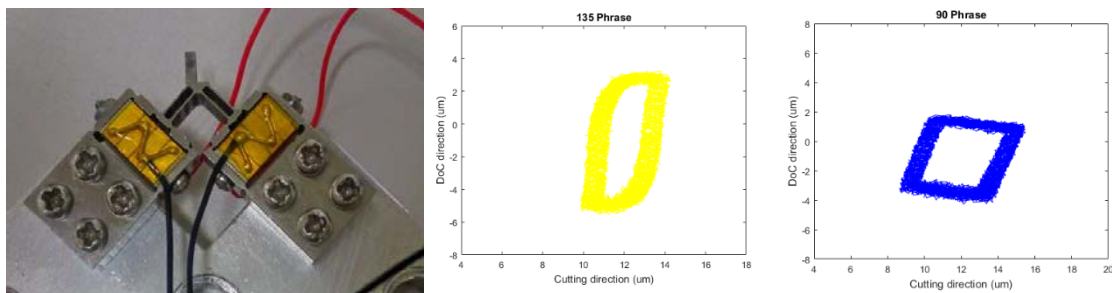


Figure 3. Prototype of non-resonant vibration cutting tool and generated arbitrary tool paths.

### 3.2 Machining micro patterns using vibration cutting

In our research, we focus on manufacturing micro-patterns with our two dimensional non-resonant tertiary motion generator, which is based on the flextensional structures. The holder of cutting tool is connected to two perpendicularly placed flextensional actuators with flexure hinges which decouple the motion outputs from the two actuators. The prototype has been developed shown in Figure 3.

We plan to manufacture the channel patterns based on the Cardioid line, and the trajectory of tool tip is shown in the following picture with  $f = 2500$  Hz and  $v = 13$  mm/s, such that

$$x = 2 \sin(\omega t) + vt$$

$$y = 3 \sin(\omega t + \theta) - 2 \sin(2\omega t + \theta)$$

By applying this trajectory, one side of the channel features is nearly vertical as shown in Figure 4, which is more effective to avoid settlement of the micro-organisms.

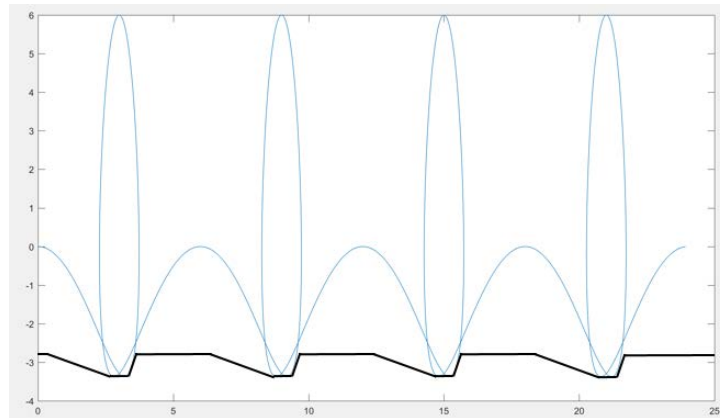


Figure 4. Proposed vibration cutting method for fast generation of micro-patterns.

### 3.3 Human mesenchymal stem cell (hMSCs) spreading on patterned surfaces

We have also tested the hMSCs spreading on patterned aluminum surfaces. The machined patterned surfaces have hierarchical micro-structures, which have first level of features in the range of several tens of microns and a second-order textures of several microns. The represented surfaces are shown in Figure 5.

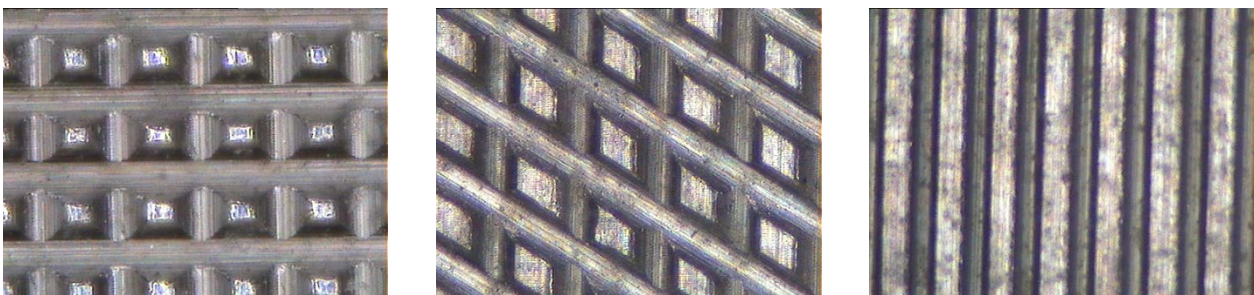
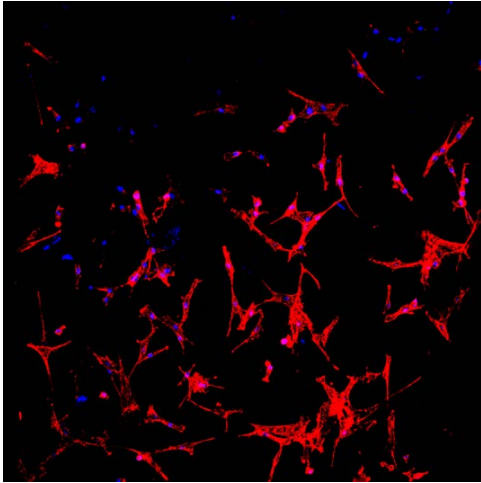
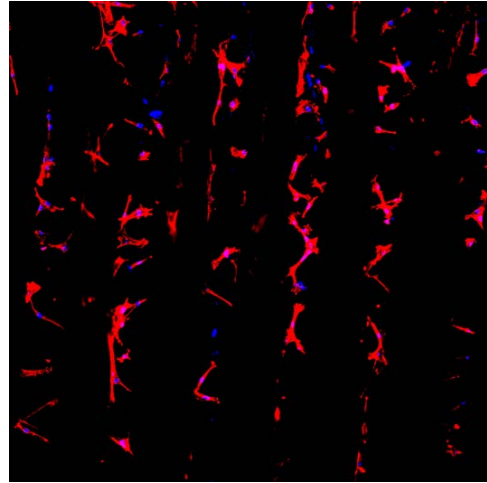


Figure 5. Machined patterned surfaces on aluminum workpieces.

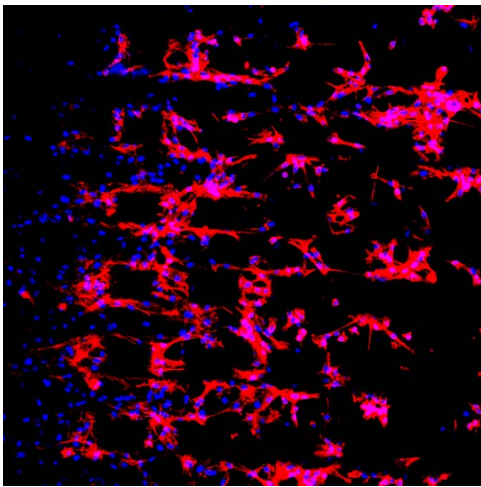
hMSCs are cultured on the sample surfaces to test their effect on the spreading and differentiation of the stem cells. The results are summarized and compared in Figure 6. According to the results, hMSCs tend to attach and spread in the valley of patterns. Few cells are on the top of patterns.



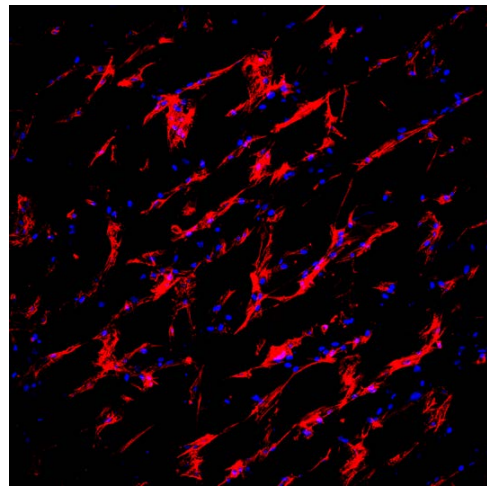
Unpatterned surface



Linear patterned surface



Rectangular patterned surface (high cell density)



Diamond patterned surface (high cell density)

Figure 6. hMSCs spreading and differentiation on unpatterned and patterned surfaces.

# DEVELOPMENT OF A NOVEL FLEXIBLE SURGICAL ROBOT WITH HAPTIC SENSATION

---

Principal Investigator: Professor Zheng LI  
*Department of Mechanical and Automation Engineering, CUHK*

Co-Investigator (if any):  
 Joseph J.Y. Sung <sup>(1)</sup>, Philip W.Y. Chiu <sup>(1, 2, 3, and 4)</sup> and Ruxu Du <sup>(5)</sup>

Research Team Members:  
 Hongmin Wang, RA <sup>(1, 2)</sup>, Chengzhi Song, Junior RA <sup>(1, 2)</sup>



- <sup>(1)</sup> Institute of Digestive Disease, CUHK
- <sup>(2)</sup> Chow Yuk Ho Technology Centre for Innovative Medicine
- <sup>(3)</sup> Biomedical Engineering, CUHK
- <sup>(4)</sup> Dept. of Surgery, CUHK
- <sup>(5)</sup> Dept. of Mechanical & Automation Engineering, CUHK

**Reporting Period: 1 July 2015 – 30 April 2016**

## ABSTRACT

This project aims to develop a novel tele-operated flexible surgical robot for general minimally invasive surgery (MIS). In the proposed robot, key drawbacks in existing surgical robots will be addressed. The performance of the robot will be evaluated systematically in the CUHK Jockey Club Minimally Invasive Surgical Skills Center and the Chow Yuk Ho Technology Center for Innovative Medicine by ex vivo mockup surgeries and animal (pig) tests.

Robot assisted MIS brings to patient multiple benefits, including shorter hospital stay, less post-operative pain, less blood loss, better cosmesis, etc. In the market, the da Vinci robot is the dominant player in MIS. It is equipped with slender rigid arms and lacks of tactile sensation which is crucial in surgical interventions. The rigid arms pivot about the trocar and lack of dexterity inside the body. Also, the pivoting creates a large sweeping motion, which may cause damages to vital structures. Flexible robot is intrinsically safer. However, their payload capacity is small due to the low stiffness. The sweeping motion generated by the arm bending remains significant. Also, the workspace and dexterity are limited due to the lack of control in either the length or the curvature of the bending section. In this project, a novel constrained tendon-driven serpentine mechanism (CTSM) will be employed to design the proposed flexible surgical robot. In the CTSM both the length and curvature of the bending section are controllable, which gives the robot much improved dexterity and larger workspace. A shape reconstruction based force sensing method will be developed to enable the robot's tactile sensation. What's more, a tension based stiffness control method will be implemented to endow controllable stiffness to the flexible robot. Therefore, the payload capability can be actively adjusted based on the surgical task. As a summary, the developed robot will integrate the following advantages: tactile sensation, much reduced sweeping motion, controllable stiffness, enhanced dexterity, and expanded workspace.

## 1. OBJECTIVES AND SIGNIFICANCE

### Project Objectives:

1. Development of a novel tele-operated flexible surgical robot with the following advantages or performances without sacrificing the surgical robot arm's dimensions:
  - (a) Tactile sensation with a force sensing resolution of finer than 0.1 N.
  - (b) Controllable stiffness: the robot can work with at least two stiffness options, i.e. stiff-floppy.
  - (c) Reduced sweeping motion than existing rigid/flexible surgical robot arms at same dimensions.

- (d) Improved dexterity than existing rigid/flexible surgical robot arms at same dimensions and same end effector condition.
  - (e) Larger reachable workspace than existing rigid/flexible surgical robot arms at same base movement.
  - (f) Tele-operation: the slave flexible robot can be controlled stably with the master input device.
2. For ex vivo mockup tests and animal tests, we'd like to achieve the following:
- (a) Build a test platform for ex vivo mockup surgery, which can be used for the developed flexible surgical robot as well as other similar surgical instruments for MIS.
  - (b) Verify the aforementioned advantages of the developed flexible surgical robot, and find its possible limitations for future improvement.
  - (c) Prove the feasibility of the developed flexible surgical robot in live animal surgery.

**Significance:** Every upgrade in surgical tools can bring multitude benefits to patients and surgeons, as shown by the da Vinci robot system. The successful completion of this work will yield a surgical robot much more capable than the existing da Vinci robot, including restored tactile sensation, controllable stiffness, reduced sweeping motion, enhanced dexterity, and expanded workspace inside the body. The tactile sensation is not possessed by the da Vinci robot yet. It gives surgeons an additional sense, therefore more comprehensive intraoperative decisions can be made. The improved dexterity and expanded workspace enable the surgeons fulfilling operations in an easier way and new operations that is less invasive and less time consuming is predictable. The reduced sweeping motion and controllable stiffness enable the robot avoiding damages to vital structures during the operation. Thus, safety can be improved. The controllable stiffness can suits the robot arm to variable surgical tasks. Therefore less surgical tools are needed during the surgery and the cost can be reduced.

## 2. RESEARCH METHODOLOGY

I. Development of A Flexible Surgical Robot Arm: Based on the CTSM, the PI proposes to develop a flexible surgical robot arm using bio-compatible materials at first. In this robot arm, four tendons will be used to control the omnidirectional bending of the flexible section. The length of the bending section is controlled by the constraint tube and the curvature is controlled by the tendons. This gives the robot arm a wide range of configurations to access the target position (enhanced dexterity). Meanwhile, the sweeping motion can be greatly reduced. Tactile sensation of the robot arm is achieved by the shape reconstruction based force sensing model. The force at the distal end is sensed and is reflected to the operator by a haptic device.

II. Development of the Flexible Surgical Robot System: In the MIS typically three arms are needed: two arms for operation and the third arm for imaging guidance. Based on the successful development of the flexible surgical robot arm, a flexible surgical robot system will be developed. This system will include two identical arms with interchangeable end effectors (e.g., forceps, grasper, needle holder and scissors) and another arm with a micro camera. The system will be tele-operated using the haptic input devices.

III. Ex vivo Tests and Animal Tests: Ex vivo tests will be performed on the flexible surgical robot arm and the robot system at the CUHK Jockey Club Minimally Invasive Surgical Skills Center and the Chow Yuk Ho Technology Center for Innovative Medicine. Workspace and dexterity inside the manikin model will be tested by accessing markers with obstacles. Haptic sensation will be tested by palpate a tissue model with known hardness distribution. Lifting performance will be conducted to test the effectiveness of the stiffness control of the robot arm. This part is expected to cost 6 months.

## 3. RESULTS ACHIEVED SO FAR

### Summary:

- Developed one test platform for studying the CTSM;
- Developed one flexible surgical robot arm prototype based on the CTSM;
- Studied the shape sensing algorithm for the CTSM;
- Published 3 journal papers and 1 conference paper; submitted another two conference papers;
- Attracted one external grant (ITF Tier 3).

### 3.1 Test platform

To study the properties of the CTSM, such as bending, stiffness, force sensing, etc., a test platform is developed as in figure 1 (a). This platform contains four stepping motors to pull the wires and one additional stepping motor to control the movement of the rigid tube. The tension in the wires are monitored by the force sensors. One Arduino board is used to control all the stepping motors. To facilitate the control of the wire movement, a graphic user interface (GUI) was developed using C#. The screenshot is as shown in figure 1 (b). On the GUI, one could control the movement of the wires in desired direction and range, also the tension could be displayed. Currently, this platform could be used to study the bending performance of the CTSM. A few improvements are needed to meet the requirement in stiffness control and force sensing. These include accuracy of the wire control, accuracy in tension monitoring, etc. In the next year, we will further refine this test platform and employ it to study the stiffness control and intrinsic force sensing of the CTSM.

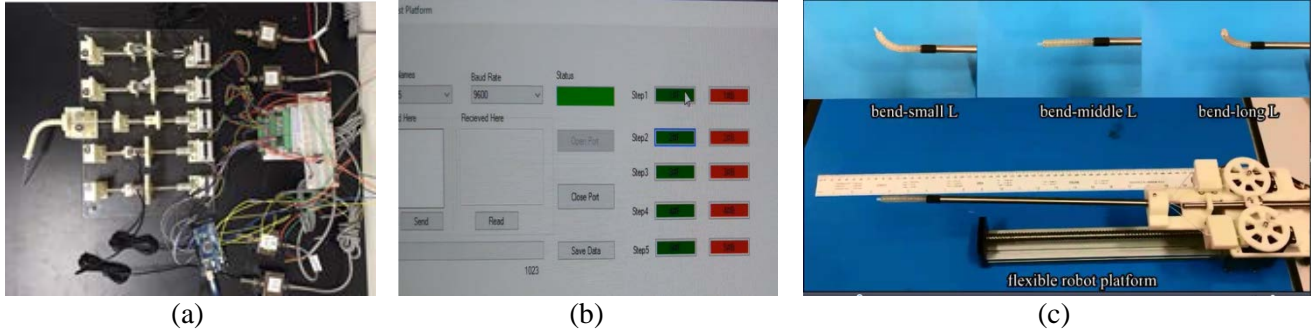


**Fig. 1** (a) the hardware; (b) screenshot of the GUI; (c) CTSM based flexible surgical manipulator.

### 3.2 Flexible surgical robot arm based on the CTSM

Figure 1 (c) shows the CTSM based flexible surgical robot arm prototype. This prototype contains one bending section, which is driven by two pairs of wires. The components in this prototype are fabricated using 3D printing. The main features of this prototype are: 1) the distal flexible section could bend to all directions by two servo motors; 2) the length of the bending section is controlled by a stepping motor; 3) a micro camera is integrated to the tip of the robot arm, which could be used for imaging in surgery; 4) the motion of the robot is controlled using joystick. This prototype could well demonstrate the concept of the CTSM and show the advantages.

### 3.3 Shape sensing method for the CTSM

To control the CTSM, including the tip position, orientation and shape of the bending section, a shape sensing method based on electromagnetic (EM) sensor is proposed. In this method, one EM sensor is used to measure the position and orientation of the CTSM distal tip. The deformed shape of the backbone is estimated using the Cubic Biezer curve, as expressed in Eq. (1). The shape of the curve is controlled by the four controlling points  $P_0$ ,  $P_1$ ,  $P_2$  and  $P_3$ . The two middle control points  $P_1$  and  $P_2$  could be expressed by the orientations at  $P_0$  and  $P_3$  as in Eq. (2), where  $H_0$  is the orientation at  $P_0$  and  $H_3$  is the orientation at  $P_3$ ,  $S_1$  and  $S_2$  represent the  $\|P_0P_1\|$  and  $\|P_2P_3\|$ .

$$\mathbf{B}(t) = (1-t)^3 \mathbf{P}_0 + 3(1-t)^2 t \mathbf{P}_1 + 3(1-t) t^2 \mathbf{P}_2 + t^3 \mathbf{P}_3 \quad (1)$$

$$\begin{cases} \mathbf{P}_1 = \mathbf{P}_0 + S_1 \mathbf{H}_0 \\ \mathbf{P}_2 = \mathbf{P}_3 - S_2 \mathbf{H}_3 \end{cases} \quad (2)$$

In the CTSM, the position and orientation of the proximal of the bending section could be obtained from the controller and the information of the distal end could be obtained using EM sensors. Since the length of the CTSM is constant, the length of the estimated curve should be the same. This is the critical information for solving the  $S_1$  and  $S_2$ . The length of the estimated Bezier curve is as in Eq. (3).

$$L_c = \sum_{i=1}^n \|\mathbf{B}_i - \mathbf{B}_{i-1}\| \quad (3)$$

Figure 2 shows some of the simulation results. From the results, this method could well predict the deformed shape of the CTSM at different bending angle and different length of bending section. In the near future, experiments will be carried to validate this shape sensing method.

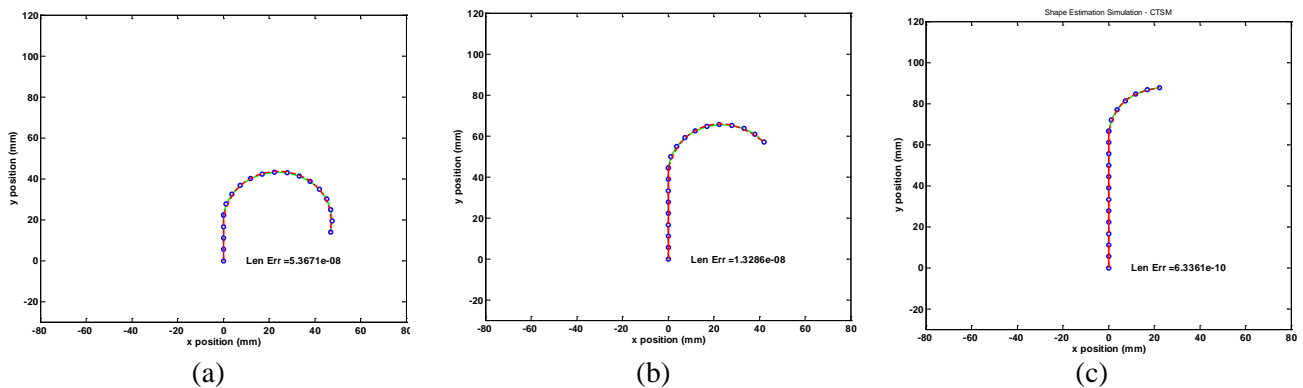


Fig. 2 Shape sensing results.

### 3.4 Initial work on flexible surgical robot system

In the next year, we will focus on developing the flexible surgical robot system and experimental testing. A framework of the flexible surgical robot system has been proposed as in figure 3. In this framework, a master input device will be used to send commands to the flexible surgical robot.

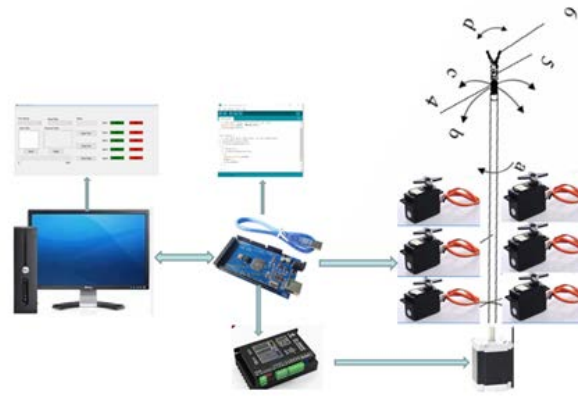


Fig. 3 Framework of the flexible surgical robot system

## 4. PUBLICATION AND AWARDS

### Journal publications:

J[1] Shuang Song, **Zheng Li**, Max Q.H. Meng, Haoyong Yu and Hongliang Ren. Real-time shape estimation for wire-driven flexible robots with multiple bending sections based on quadratic Bezier curves [J] Sensors Journal, IEEE, 2015, 15(11): 6326-6334.

J[2] **Zheng Li**, Hongliang Ren, **Philip W.Y. Chiu**, **Ruxu Du** and Haoyong Yu. A novel constrained wire-driven flexible mechanism and its kinematic analysis [J]. Mechanism and Machine Theory, 2016, 95: 59-75.

J[3] **Zheng Li**, Min Zin Oo, Varun Nalam, et al. Design of a Novel Flexible Endoscope - Cardioscope [J]. Journal of Mechanisms and Robotics, ASME, 2016, 8 (5):1-9.

### Conference publications:

C[1] **Zheng Li**, Hao Yong Yu, Hongliang Ren, **Philip W.Y. Chiu** and **Ruxu Du**. A Novel Constrained Tendon-driven Serpentine Manipulator [C], Intelligent Robots and Systems (IROS), 2015 IEEE/RSJ International Conference on. IEEE, 2015: 5966-5971.

- C[2] **Zheng Li, Chengzhi Song and Hongmin Wang.** Design and Prototyping of A Concentric Wire-driven Manipulator [C]. Biomedical Robotics and Biomechanics (BioRob), 2016 IEEE RAS/EMBS International Conference on. (Accepted)
- C[3] **Zheng Li, Philip W.Y. Chiu and Ruxu Du.** Design and Kinematic Modeling of A Concentric Wire-driven Mechanism Targeted for Minimally Invasive Surgery [C]. Intelligent Robots and Systems (IROS), 2016 IEEE/RSJ International Conference on. (Submitted)

# DEVELOPMENT OF INJECTABLE SUPRAMOLECULAR HYDROGELS FOR REGENERATIVE MEDICINE

---

Principal Investigator: Professor BIAN Liming  
*Department of Mechanical & Automation Engineering, CUHK*

Co-Investigator (if any): Gang Li<sup>(3)</sup>, Arthur Mak<sup>(2)</sup>

Research Team Members:

Zhu Meiling, Feng Qian, Wei Kongchang, Li Jinming<sup>(1)</sup>

<sup>(1)</sup> Dept. of Mechanical & Automation Engineering, CUHK

<sup>(2)</sup> Dept. of Biomedical Engineering, CUHK

<sup>(3)</sup> Dept. of Orthopaedics and Traumatology, CUHK



**Reporting Period: 1 July 2015 – 30 April 2016**

## ABSTRACT

**Objectives:** to develop self-healing, bioadhesive, and mechanically resilient supramolecular gelatin hydrogels for articular cartilage repair.

**Motivation:** hydrogels are ideal carrier material for the delivery of therapeutic cells (like stem cells) and drugs to enhance the healing and regeneration of damaged biological tissues/organs. However, conventional chemically crosslinked hydrogels have a number of limitations that hinder the clinical translation of these hydrogels. In this project, we aim to develop novel supramolecular hydrogels, which are free of chemical crosslinking and have an array of unique features that are desirable for potential clinical applications.

**Methodology:** supramolecular hydrogel are generally mechanically weak. We have developed a novel “Host-guest macromer” (HGM) approach to fabricate supramolecular hydrogels with enhanced mechanical properties. Briefly, premixing the free diffusing crosslinkable host molecules with the polymer containing guest motifs significantly enhance the host-guest complexation efficiency due to the low steric hindrance. The subsequent polymerization of the obtained “HGM” produces the supramolecular hydrogels that are highly stretchable and self-healable. Furthermore, the residual hydrophobic cavities of the host molecules in the hydrogels afford the potential for facile modular modifications such as incorporation of hydrophobic drugs and tethering of bioactive molecules.

**Impact & benefit:** the advantages of the proposed HGM supramolecular hydrogels compared to existing products include mechanical resilience, tissue adhesiveness, self-healing, ease of use, and capability of delivering hydrophobic drugs. These benefits make the proposed hydrogels ideal vehicles for delivering therapeutic cells and drugs to assist treatments of human cartilage defects and a variety of other diseases including spinal cord injury, intervertebral disc herniation, etc.

## 1. OBJECTIVES AND SIGNIFICANCE

This project aims to develop novel supramolecular hydrogels to address these limitations of existing hydrogels, and following project objectives are proposed.

1. To fabricate and characterize the supramolecular gelatin hydrogels.
2. To examine the hMSC chondrogenesis in the physically crosslinked supramolecular hydrogels

- To assess the controlled release of hydrophobic chondrogenic small molecules from the supramolecular hydrogels.
- To evaluate the efficacy of the supramolecular hydrogels as the carrier material of stem cells and drug to repair cartilage defects in an animal model.

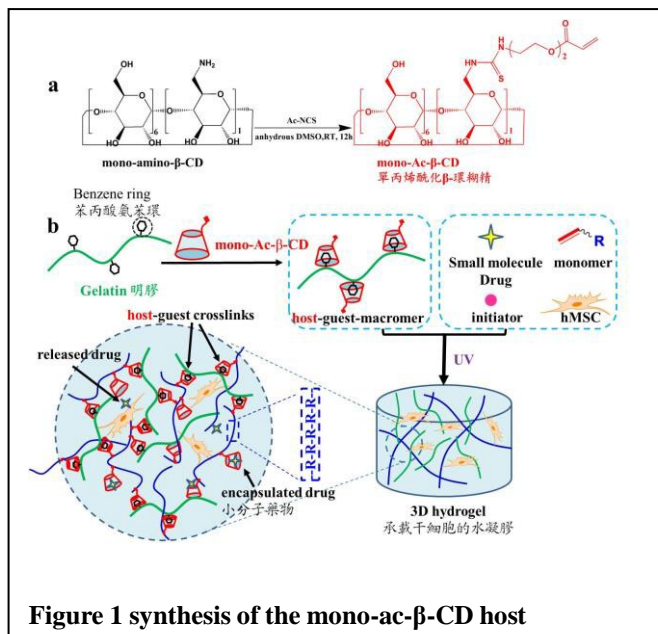
### Impact and benefits

The findings from this project will help guide the design and promote the clinical translation of injectable hydrogels for cartilage repair. Hydrogels developed in this study will not only enhance cartilage repair but will also be instrumental to the development of minimal invasive therapies for repairing connective tissues including bone, meniscus and intervertebral disc.

## 2. RESEARCH METHODOLOGY

### Objective 1: To fabricate and characterize the supramolecular gelatin hydrogels

#### i. Synthesis of mono-functional acrylated host molecule $\beta$ -cyclodextrins (mono-Ac- $\beta$ -CD)



Ac- $\beta$ -CD (or mono Ac- $\beta$ -CD) will be synthesized as reported previously [15] (Figure 1a). Briefly,  $\beta$ -cyclodextrin will be dissolved in 100 mL anhydrous DMF at room temperature followed by the addition of trimethylamine. The mixture will be cooled to 0 °C on ice. Acryloyl chloride will be added slowly. The reaction will be kept at room temperature for 12hr before being dripped into acetone. The precipitate will be washed with acetone and dried in vacuum. The degree of acrylation will be controlled to be around 1.0 and confirmed by  $^1\text{H}$  NMR.

#### ii. Hydrogel fabrication, and rheological and mechanical testing

Typically, a mixture of gelatin, Ac- $\beta$ -CD, photoinitiator (I2959) will be dissolved in PBS and exposed to UV light (10 mW/cm<sup>2</sup>, 10min)

to form the hydrogels (Figure 1b). The effect of additional monomers such as poly (ethylene glycol) acrylate on the hydrogel mechanical properties will also be examined. Dynamic viscoelasticity of the hydrogels will be measured by a rheometer using a plate-plate setup. The mechanical properties of the hydrogels will be measured on a MACH-1 Micromechanical.

#### iii. Injectability and self-healing evaluation

Freshly cut hydrogels will be kept in juxtaposition to allow healing. The tensile property of the healed hydrogels will be evaluated and compared to those of the intact hydrogels. The injectability of the hydrogels will be evaluated by a custom protocol. Briefly, preformed hydrogels of rectangular shape will be loaded into a syringe by suction and injected into a mold of triangular shape. The viability of the hMSCs encapsulated within the hydrogels after injection will be examined by using a viability staining kit (Invitrogen).

## **Objective 2: to examine the hMSC chondrogenesis in the physically crosslinked supramolecular hydrogels**

### **i.hMSC encapsulation in ECM hydrogels and chondrogenic induction**

hMSCs (Lonza) will be expanded to passage 3 in a growth medium consisting of  $\alpha$ -MEM with 16.7% FBS (fetal bovine serum). hMSCs (20 million/ml) will be encapsulated in hydrogel constructs ( $\varnothing$ 5mm, 2 mm thickness). Constructs will be cultured in chondrogenic media (DMEM, 1% ITS+Premix, 50  $\mu$ g/ml L-proline, 0.1  $\mu$ M dexamethasone, 50 $\mu$ g/ml ascorbate) supplemented with transforming growth factor (TGF- $\beta$ 3, 10ng/ml)(Figure 1 b)[16].

### **ii.Gene expression analysis**

RNA will be extracted using Trizol according to the manufacturer's instructions, and the RNA concentration will be determined using a spectrophotometer (Nanodrop). Obtained RNA will be reverse transcribed into cDNA using a reverse transcription kit (Invitrogen). The real time polymerase chain reaction (qPCR) will be performed using Taqman primers and probes specific for GAPDH (housekeeping gene) and other genes of interest (type II collagen, Aggrecan, Sox9). The sequences of the primers and probes are listed in a previous publication [17]. The relative gene expression will be calculated using the  $\Delta\Delta$ CT method.

### **iii.Histological analysis**

The remaining halves of the constructs will be fixed in 4% formalin, embedded in paraffin, and processed using standard histological procedures. Immunohistochemical staining will be performed on histological sections (8  $\mu$ m thick) for targets of interest using the Vectastain ABC kit and the DAB Substrate kit for peroxidase (Vector Labs). Non-immune controls will undergo the same procedure without primary antibody incubation.

### **iv.Statistical and power analysis**

Statistica (Statsoft) will be used to perform statistical analyses using two-way ANOVA, followed by Tukey's HSD post hoc testing to allow for comparison between groups. Statistical significance will be set at  $p < 0.05$ . A statistical power analysis indicates that  $n=8$  samples per group should be sufficient for obtaining a study power of 0.85 with significance set at  $p<0.05$ .

## **Objective 4: To evaluate the efficacy of the supramolecular hydrogels as the carrier material of stem cells and drug to repair cartilage defects in an animal model**

The following animal studies will be conducted in collaboration with Co-PI Professor Li Gang from the Department of Orthopaedics and Traumatology. Guidelines on animal care and use from the Chinese University of Hong Kong will be followed.

### **1. Implantation in critical-sized focal cartilage defect in rabbits**

New Zealand White rabbits (8 weeks) will be used. Surgery will be performed to expose the left knee joints under anesthesia. 3 mm diameter defects will be created in the center of the trochlear groove with a biopsy punch without disrupting the subchondral bone. The hMSCs and kartogenin loaded hydrogels will be injected into the defects. The same procedures will be performed on the right knees without injecting the hydrogels and cells to serve as the control. The knee joints will be closed with sutures. The animals will be followed for 10 weeks.

### 3. RESULTS ACHIEVED SO FAR

#### Objective 1: To fabricate and characterize the supramolecular gelatin hydrogels

we have successfully synthesized mono-functional acrylated host molecule  $\beta$ -cyclodextrins (mono- Ac- $\beta$ -CD). The synthesis products were evaluated using NMR to confirm the synthesized product (Figure 2). 2D-NOSEY NMR confirms that mono-Ac- $\beta$ -CD can complex with the gelatin molecules (Figure 3). Rheological studies show that stable supramolecular hydrogels can be formed (Figure 4, Figure 5). As the Ac-CD content increases, both the storage and loss modulus of the supramolecular hydrogels increase at 25°C (Figure 4a). The tensile and compressive properties of gelatin hydrogels are also improved. At 25°C, unmodified gelatin (8% (w/v), Gel8CD0) is a brittle hydrogel with a small failure strain of around 20% (Figure 4c). Similarly, the chemically crosslinked methacrylated gelatin (MeGel) hydrogels are even more brittle and break at a tensile strain of around 10% at 25°C. In contrast, the physically crosslinked HGM hydrogels containing the same content of gelatin as that in the unmodified and methacrylated gelatin hydrogels, break at much higher strains (145% for Gel8CD4 and 205% for Gel8CD10) (Figure. S4c). This dramatic change indicates the efficacy of the supramolecular approach in preparing highly stretchable hydrogels. It should be noted that the Young's modulus of the HGM hydrogels decreases with the increasing content of Ac- $\beta$ -CD (Figure 4c). This may be due to the reduction of gelatin inter-molecular interactions as a result of the hydrophobic aromatic residues complexing with ac-CDs. Moreover, at 37°C, the breaking strains are higher than those measured at 25°C.

The fragmented HGM hydrogel pieces are capable of self-healing and becoming one integrated hydrogel again due to the reversible nature of the host-guest complexation crosslinks (Figure 6, Figure 7). This finding further demonstrates the self-healing property of HGM hydrogels that will be instrumental to the retention and structural integrity of the hydrogels, and therefore the targeted delivery of the loaded cells/drugs after injection, especially in load-bearing locations in vivo.

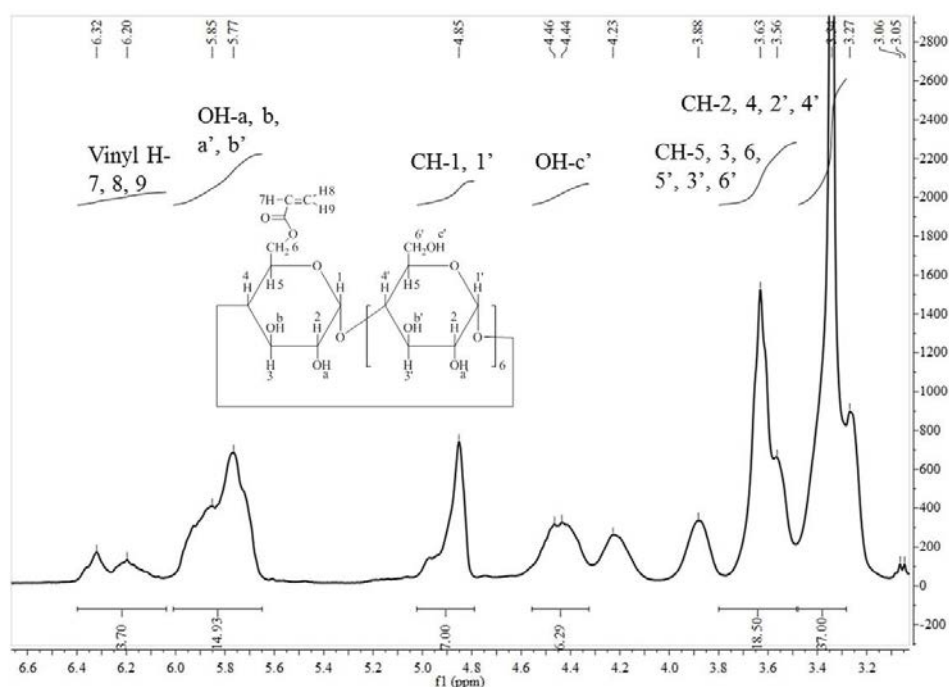


**Figure 2**  $^1\text{H}$  NMR of Ac- $\beta$ -CD recorded in DMSO- $d_6$ .  $^1\text{H}$  NMR (400 MHz, DMSO)  $\delta$  6.26 (d,  $J$  = 49.2 Hz, 1H), 5.81 (d,  $J$  = 34.6 Hz, 4H), 4.85 (s, 1H), 4.45 (d,  $J$  = 11.7 Hz, 1H), 3.63 (s, 2H), 3.34 (s, 9H).

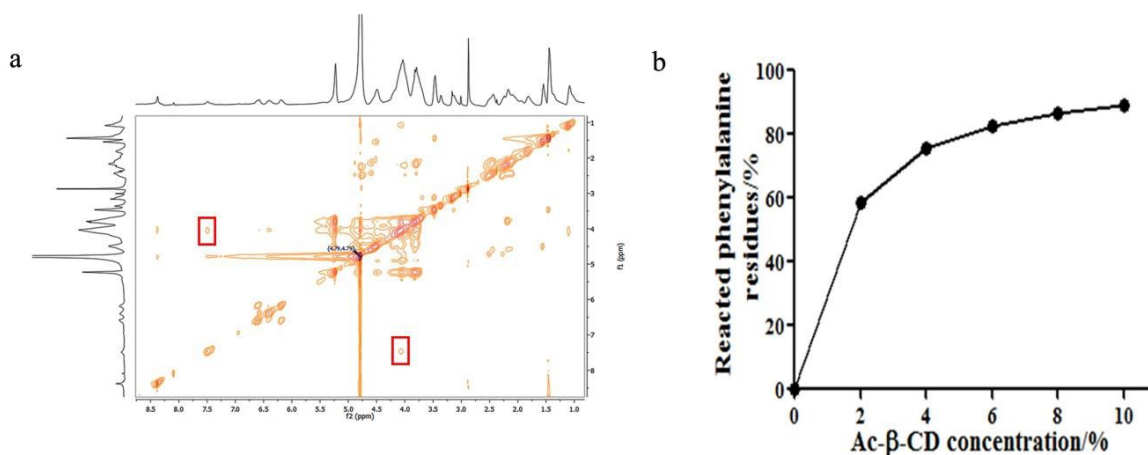


**Figure 3.** (a) 2D-NOSEY NMR of gelatin/Ac-β-CD mixture recorded in D2O at 37°C. (b) Reacted aromatic residues percentage depending on the Ac-β-CD concentration at 37°C.

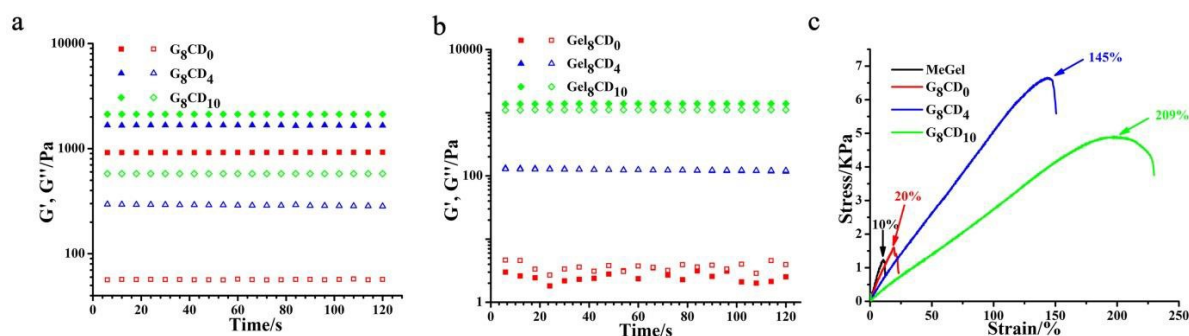


**Figure 4** (a) Time sweep of dynamic rheology study on GelxCDy at 25°C. (b) Time sweep of dynamic rheology study on GelxCDy at 37°C; (c) Stress vs. strain curves of Me-gelatin and GelxCDy at 25°C.

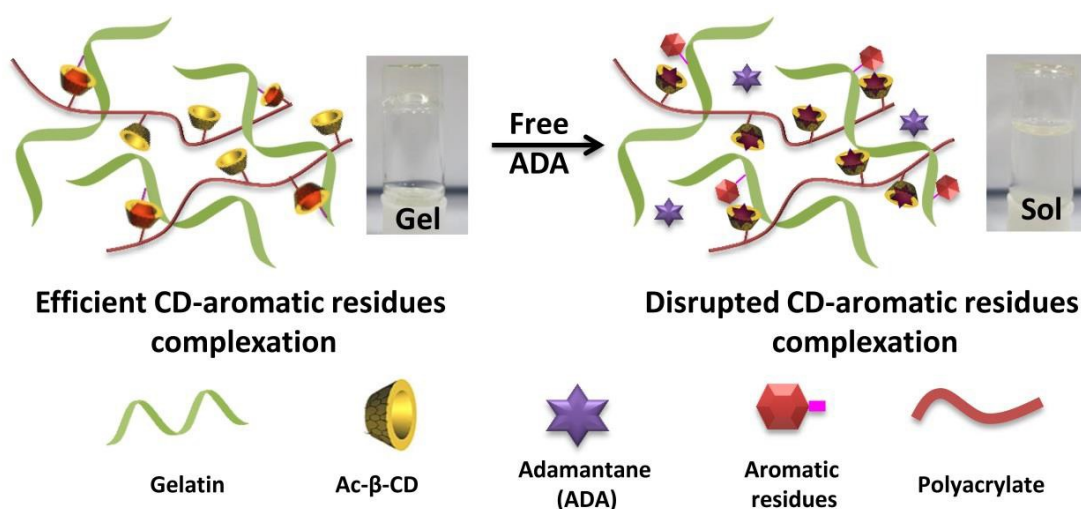


**Figure 5** Dissolution of HGM hydrogel with free adamantane (ADA) solution at 37°C.

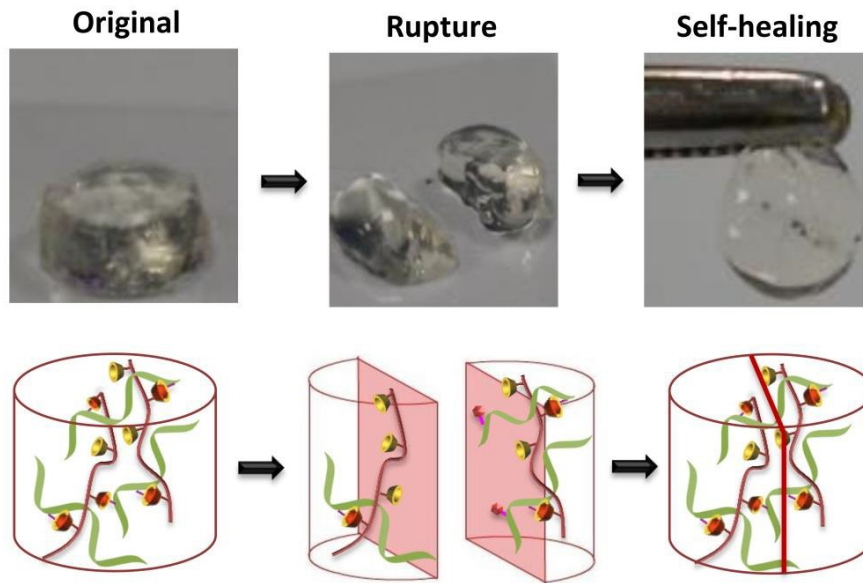


**Figure 6** Self-healing properties of HGM hydrogels at 37°C: the two halves of the cut supramolecular hydrogel self-heal to reintegrate into one piece after brief 5 min incubation in juxtaposition.

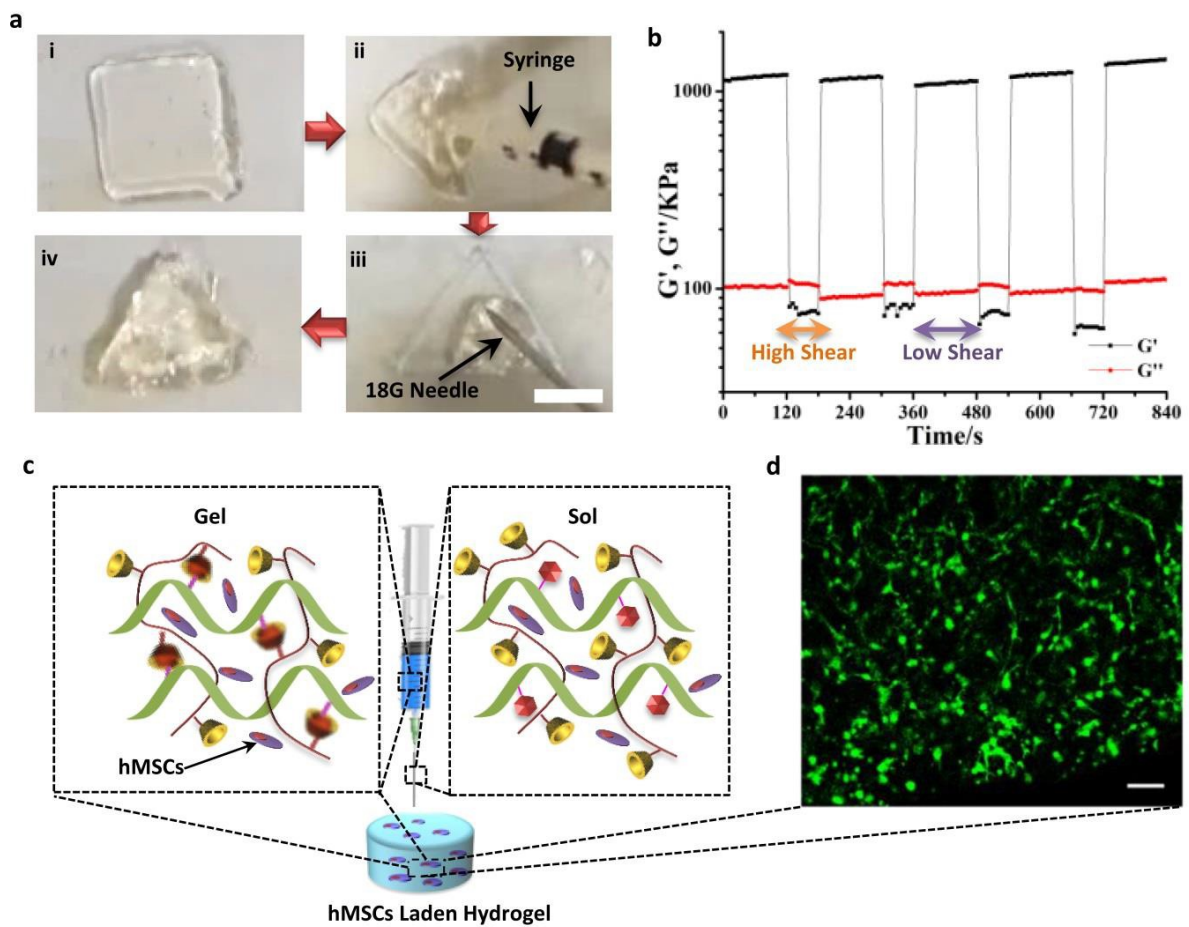


**Figure 7** The self-healing and injectable behavior of HGM hydrogels at 37 °C.

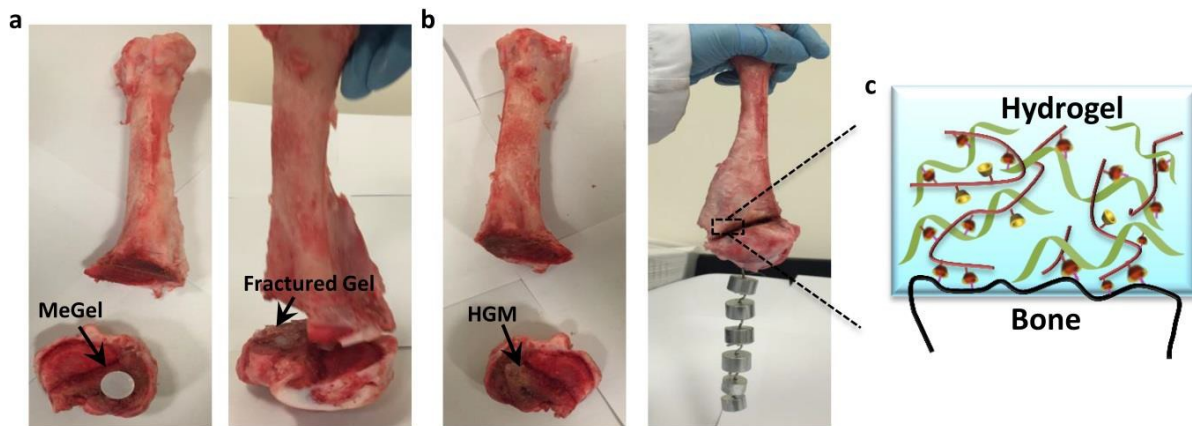


**Figure 8** The HGM hydrogels bond two pieces of bone tightly even in the aqueous environment (in PBS), whereas conventional MeGel hydrogels are not bioadhesive.

**Objective 2: to examine the hMSC chondrogenesis in the physically crosslinked supramolecular hydrogels**

We have encapsulated hMSCs in the HGM supramolecular hydrogels and the conventional chemically crosslinked MeGel hydrogels. Cell viability assay shows that hMSCs remain mostly viable in both hydrogels, and the cells in the HGM hydrogels are capable of spreading within the hydrogels (**Figure 9**)

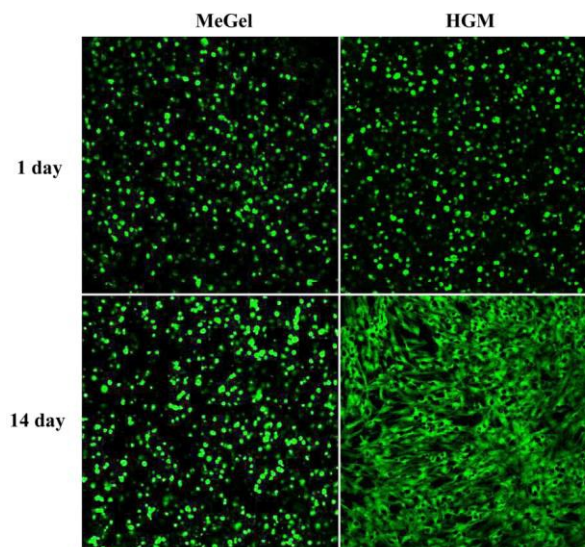


**Figure 9** Cell viability staining of the hMSC-laden MeGel and HGM hydrogels after 1 day and 14 days of culture.

**Objective 3: To assess the controlled release of hydrophobic chondrogenic small molecules from the supramolecular hydrogels**

We have encapsulated both the small molecular drug, KGN, and the model protein, BSA in our supramolecular hydrogels (Figure 10). Cumulative release data show that our supramolecular hydrogels are capable of mediating the more sustained release of both KGN and BSA (Figure 11, Figure 12), which will be beneficial to the differentiation of the encapsulated hMSCs.

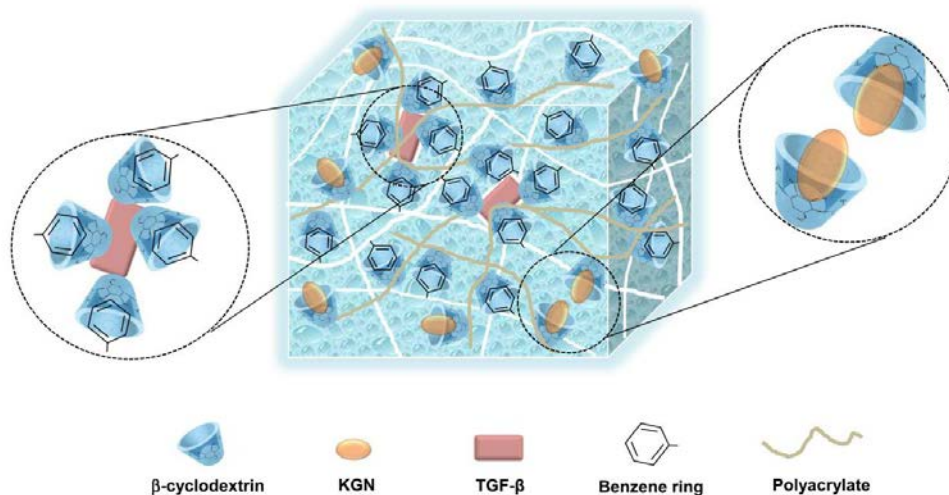


**Figure 10** Schematics of delivery of hydrophobic drugs and growth factors by HGM hydrogels.

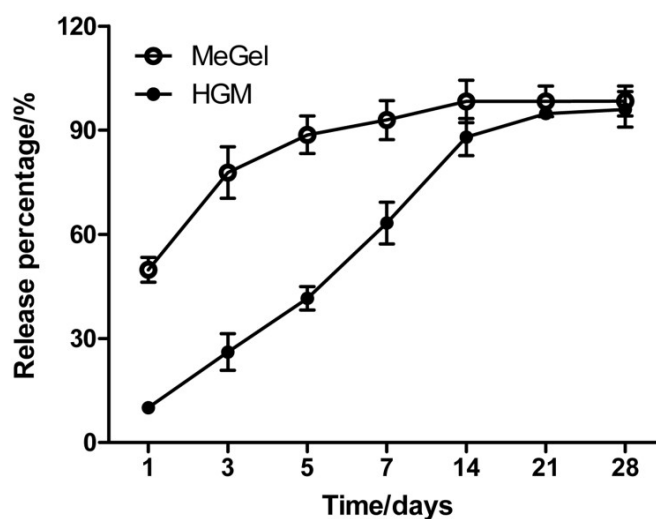


**Figure 11** Cumulative release of KGN encapsulated in the MeGel and HGM hydrogels.

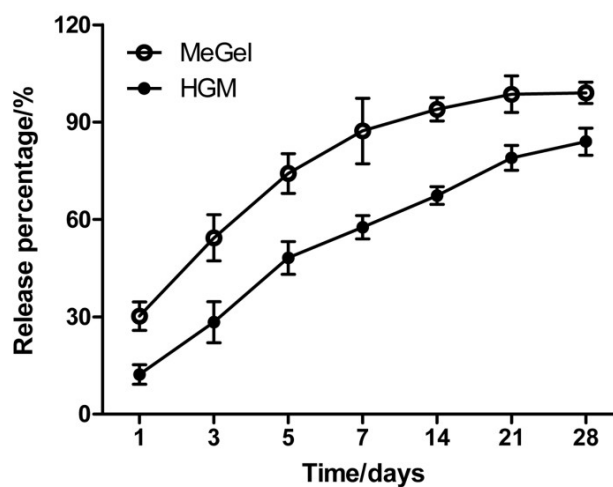


**Figure 12** Cumulative release of BSA encapsulated in the MeHA and HGM hydrogels.

#### 4. PUBLICATION AND AWARDS

(\*corresponding author)

1. +Feng, Q.; +Wei, K.; Lin, S.; Xu, Z.; Shi, P.; Gang Li, G.; \*Bian, L. Supramolecularly Engineered Multifunctional Gelatin Hydrogel Crosslinked by Host-Guest Interactions for Regenerative Medicine. Under review.
2. Huang, H.; Xu, J.; Wei, K.; Xu, Y.; Choi, C. K.; \*Bian, L. Bioactive nanocomposite poly (ethylene glycol) hydrogels crosslinked by multifunctional layered double hydroxides nano-crosslinkers. *Macromolecular Bioscience*, Accepted.
3. Wei, K.; Zhu, M.; Su, Y.; Xu, J.; Feng, Q.; Lin, S.; Wu, T.; Xu, J.; Tian, F.; Xia, J.; Li, G.; \*Bian, L. Robust biopolymeric supramolecular Host-Guest Macromer hydrogels reinforced by in situ formed multivalent nanoclusters for cartilage regeneration. *Macromolecules*, 2016 Jan, 49 (3), pp 866-875.

# DEVELOPING OPTOMECHANICAL DEVICES BASED ON LAYERED NANOMATERIALS FOR SINGLE-BIOMOLECULE MASS SPECTROMETRY

---

Principal Investigator: Professor Xiankai SUN  
*Department of Electronic Engineering, CUHK*

Co-Investigator (if any): Prof. Xu, Jianbin <sup>(1,2)</sup>

Research Team Members:

Ma, Jingwen, Junior Research Assistant <sup>(1,2)</sup>

Gu, Jiahua, Junior Research Assistant <sup>(1,2)</sup>

Li, Yuan, Junior Research Assistant <sup>(1,2)</sup>

Xi, Xiang, Research Postgraduate Student <sup>(1)</sup>

Yu, Zejie, Research Postgraduate Student <sup>(1)</sup>



<sup>(1)</sup> Dept. of Electronic Engineering, CUHK

<sup>(2)</sup> Shun Hing Institute of Advanced Engineering, CUHK

**Reporting Period: 1 July 2015 – 30 April 2016**

## ABSTRACT

The capability of determining the mass of biomolecules with high accuracy and fast speed has been playing a crucial role in proteomics for the development of molecular and cellular biology. Conventional mass spectrometers suffer from high cost, relatively large sample consumption, and low sensitivity. Nanoelectromechanical-system-based mass spectrometers can measure the proteins' mass directly. Landing of analyte (e.g., a protein) onto the device results in a variation of the resonator mass and thus shifts its resonant frequency. By tracking the frequency shift in real time, one can measure the mass variation, so as to determine the analyte species and quantity. However, the large parasitic capacitance and impedance mismatch inherent with the electrical transduction scheme limit the operation bandwidth and detection sensitivity.

Here we develop nanophotonic and nano-optomechanical devices based on layered nanomaterials (e.g., graphene, MoS<sub>2</sub>, and black phosphorus) to obtain the ultimate sensitivity. The mass of the mechanical resonator is greatly reduced from that made in a traditional material, thus enabling a much higher resolution for detecting the analyte mass. By using optical methods for mechanical actuation and detection, we can obtain unlimited operation bandwidth and, more importantly, the ultimate detection sensitivity that is capable for resolving a single biomolecule.

## 1. OBJECTIVES AND SIGNIFICANCE

### Objectives:

1. To design and simulate an optomechanical structure based on layered nanomaterials that is capable of detecting a single biomolecule for mass spectrometry
2. To establish an on-chip integrated photonics platform that involves simultaneous measurements of photonic, electronic, and mechanical properties
3. To experimentally investigate the schemes of monolithic integration of nanophotonic circuits and nanomechanical resonators with layered nanomaterials
4. To fabricate an optomechanical device based on a layered nanomaterial and characterize its photonic and mechanical properties

### Significance:

Mass spectrometry has been playing a crucial role in proteomics for the development of molecular and cellular biology. Its capability to identify and precisely quantify proteins from complex samples has broad impact on biology and medicine. Conventional mass spectrometers measure electromagnetic properties of ionized biomolecules to determine their mass-to-charge ratios, but this technique suffers from high cost, relatively large sample consumption, and low sensitivity. Nanoelectromechanical system (NEMS)-based mass spectrometers measure mass of the proteins directly. Such spectrometers serve as an efficient interface between the frontend analyte and the backend outside world with the aid of CMOS integrated electronics. Landing of analyte (e.g., a protein) onto the device results in a variation of the resonator mass and thus shifts its resonant frequency. By tracking the frequency shift in real time, one can measure the analyte mass, so as to determine its species and quantity. However, the large parasitic capacitance and impedance mismatch inherent with NEMS limit the operation bandwidth and detection sensitivity. To overcome this difficulty, we develop nano-optomechanical devices based on layered nanomaterials (e.g., graphene, MoS<sub>2</sub>, and black phosphorus) aiming to obtain the ultimate detection sensitivity. With a layered nanomaterial being the nanomechanical element, the mass of the mechanical resonator is greatly reduced from that made in a traditional material, thus enabling a much higher resolution for detecting the analyte mass. By using optical methods for mechanical actuation and detection, we can obtain unlimited operation bandwidth and, more importantly, the ultimate detection sensitivity that is capable for resolving a single biomolecule. The ability to detect single proteins in real time will eventually lead to the possibility of single-cell proteome profiling, an important milestone in both areas of biology and medicine.

## 2. RESEARCH METHODOLOGY

### Theory and device design

We focus on two types of nanomechanical resonators: one is a bar-shaped doubly clamped beam resonator with length  $L$  and the other is a circular “drum” resonator with diameter  $D$ . Their resonant frequencies are:

$$f_{\text{beam}} = \frac{1}{2L} \sqrt{\frac{E}{\rho}} \varepsilon, \quad f_{\text{drum}} = \frac{0.766}{D} \sqrt{\frac{E}{\rho}} \varepsilon,$$

where  $E$ ,  $\rho$ , and  $\varepsilon$  are the elastic stiffness, mass density, and strain, respectively. For two-dimensional graphene nanosheets,  $E = 340 \text{ N/m}$ ,  $\rho = 7.4 \times 10^{-19} \text{ kg}/\mu\text{m}^2$ , and  $\varepsilon$  can vary from case to case. Figure 1 shows the calculated resonant frequencies assuming that  $\varepsilon = 0.01$ .

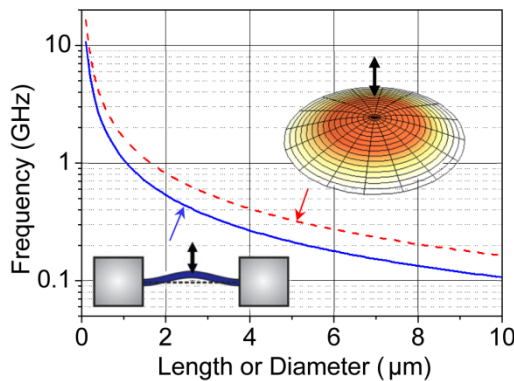


Fig. 1. Theoretical resonant frequencies of doubly clamped beam (blue solid) and circular drum (red dashed) graphene resonator as a function of the beam length  $L$  or drum diameter  $D$ .

For a drum resonator with  $D$  of  $1 \mu\text{m}$ , it has a mass  $m_0$  of  $0.58 \text{ fg}$  and it vibrates in its fundamental mechanical mode with a resonant frequency  $f_0$  around  $1 \text{ GHz}$ . Variation in the resonator mass can be detected from a corresponding shift of the mechanical resonant frequency. The mass detection resolution  $\delta m$  is proportional to the minimal observable frequency shift  $\delta f$ :

$$\frac{\delta m}{m_0} = 2 \frac{\delta f}{f_0} \approx 2 \cdot 10^{-DR/20} \sqrt{\frac{BW}{f_0} \frac{2\pi}{Q}},$$

where  $DR$  is the dynamic range in units of dB,  $BW$  is the measurement bandwidth, and  $Q$  is the quality factor of the mechanical resonator. With reasonable values of  $DR = 60$  dB,  $BW = 1$  kHz, and  $Q = 100$ , we estimate a mass detection resolution  $\delta m$  of 30 yoctograms. This is sufficient to accurately determine the mass of a single biomolecule, because the mass of typical biomolecules is 10s of zeptograms.

### Device description

Figure 2 is a conceptual illustration of a hybrid integrated nano-optomechanical device: the photonic element is realized in a planar silicon photonic circuit while the mechanical element is made of a layered nanomaterial. Due to the strong optomechanical coupling, the mechanical drumhead motion can be sensitively transduced into the optical domain. The transduction signal can be significantly enhanced if a photonic cavity (e.g., a ring cavity) is incorporated into the design.

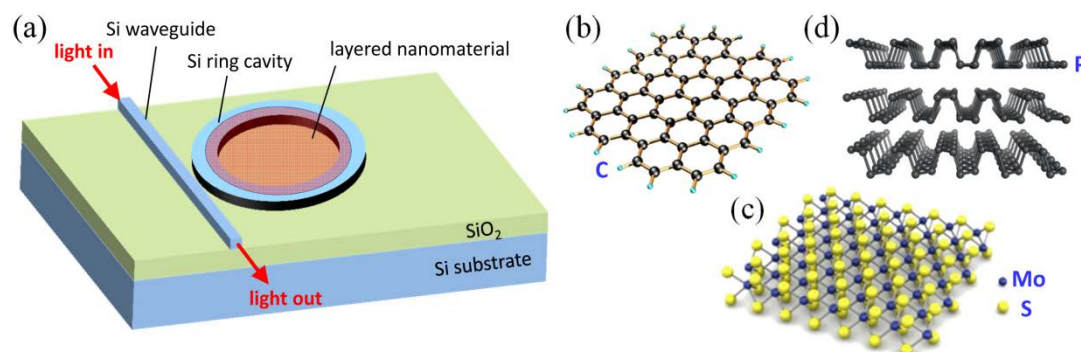


Fig. 2. (a) Optomechanical device based on hybrid integration of Si and a layered nanomaterial. (b–d) Layered structure of graphene (b), MoS<sub>2</sub> (c), and black phosphorus (d).

### Device fabrication and characterization

The devices can be fabricated with a CMOS-compatible top-down nanofabrication approach. The planar photonic circuits are fabricated on a silicon-on-insulator substrate. The pattern of the photonic circuits is defined by high-resolution electron-beam lithography and then transferred to the silicon device layer by plasma dry etching. The graphene nanosheet (or other layered nanomaterials) that forms the mechanical resonator is then placed on top of the photonic circuit by a standard transfer technique. An additional step of photolithography and subsequent etching is employed to define the shape of the nanosheet as needed. The fabricated device chip should be placed in a vacuum chamber that is equipped with optical and electrical feedthroughs for characterizing the devices' optical and mechanical properties. The vacuum chamber helps to maintain an ultralow ambient pressure so that the air damping effect to the mechanical resonator is minimized. The response of mechanical resonant frequency to additional mass loading onto the resonator can be examined experimentally to determine the device's sensitivity of mass detection.

## 3. RESULTS ACHIEVED SO FAR

### 3.1. Design and simulation of a graphene-based optomechanical resonator

In order to enhance optomechanical interaction between a photonic cavity and a layered nanomaterial, we have designed and simulated a type of photonic cavity based on circular photonic crystal. The structure is shown in the left panel of Fig. 3. The light is confined to the center hole with diameter of 3  $\mu\text{m}$ . With finite-difference time-domain simulation, we obtained the optical modal field profile, which is superimposed on the structure, with an optical  $Q$  factor of  $\sim 400$ . We have also simulated with a finite-element method the mechanical modes of a graphene drum with diameter of 3  $\mu\text{m}$ , with their mechanical displacement field shown in the right panel of Fig. 3. The fundamental mechanical mode vibrating at 0.44 GHz possesses substantial overlap with the optical mode, thus ensuring a strong optomechanical transduction.

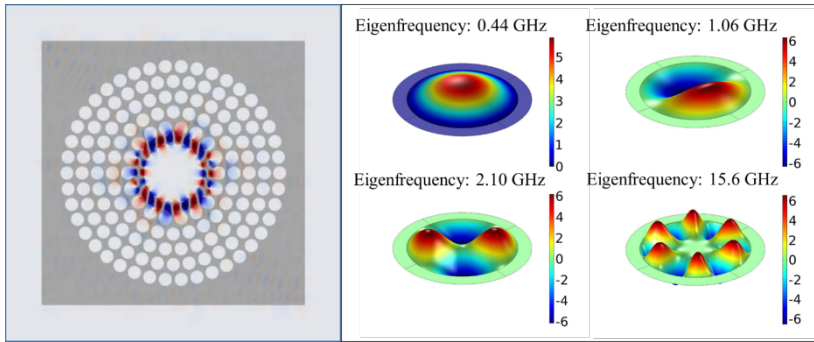


Fig. 3. (left) Sunflower-type photonic crystal cavity for confining light to the center region. (right) Displacement field of the first 4 mechanical modes of the graphene drum placed at the center of the photonic crystal cavity.

### 3.2. Design and simulation of a graphene-based optical isolator

Optical isolators are a critical component to ensure unidirectional light flow. They are often used in optical systems to prevent reflection of light back into a laser source. Here we have designed an integrated version of optical isolator for controlling on-chip light flow based on the same hybrid integration platform. As shown in Fig. 4(a), it consists of a photonic bus waveguide and a microring resonator, whose inner top surface is covered by a patterned graphene nanoribbon. When a magnetic field is perpendicularly applied to the device plane, we expect distinct light transmission spectra for the two opposite propagation directions, thus achieving the function of optical isolation. As shown in Fig. 4(c), at 77 K and 8.4 T we can achieve an extinction ratio of  $\sim 45$  dB with a reasonable insertion loss of  $\sim 12$  dB for light of  $1.552 \mu\text{m}$  wavelength. Such integrated nonreciprocal devices based on two-dimensional materials should find great promise and wide applications in the next-generation on-chip photonic systems.

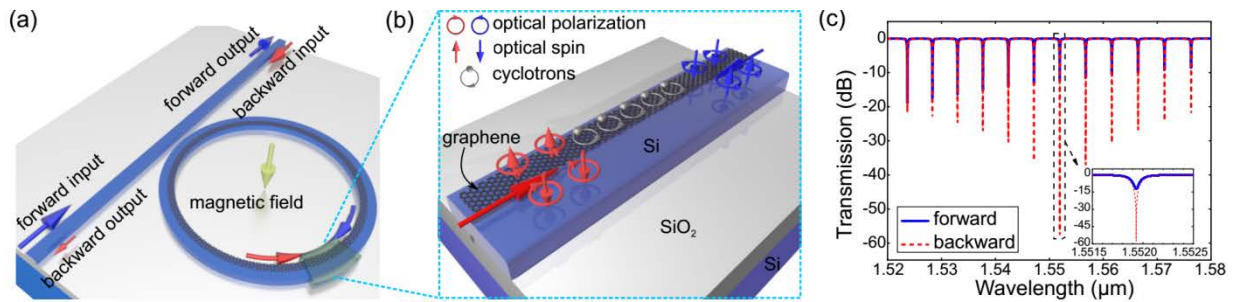


Fig. 4. (a) Schematic of the hybrid graphene/silicon integrated optical isolator. (b) A zoomed section of the isolator showing mechanism of the nonreciprocal optical transmission. (c) Calculated forward and backward light transmission spectra of the proposed device.

### 3.3. Experimental progress of device fabrication

The device fabrication involves conventional top-down nanofabrication approach for patterning the silicon structures plus a step of graphene transfer. In the past year, our group members have received extensive training on the relevant equipment in the cleanroom for various processing steps, including photolithography, electron-beam lithography (EBL), reactive ion etching (RIE), and wet chemistry processing, and have qualified for photolithography and RIE. With the EBL training still ongoing, we have already practiced many times and fabricated some critical components of this project, e.g., integrated grating couplers and microring resonators (Fig. 5). On the other hand, we have also obtained graphene samples to be transferred onto our fabricated chips. The next immediate step is to combine the graphene mechanical resonator with the photonic components and optimize the device performance. In summary, we have already acquired the capabilities and are ready to move on to the next phase to produce our proposed graphene nano-optomechanical devices.

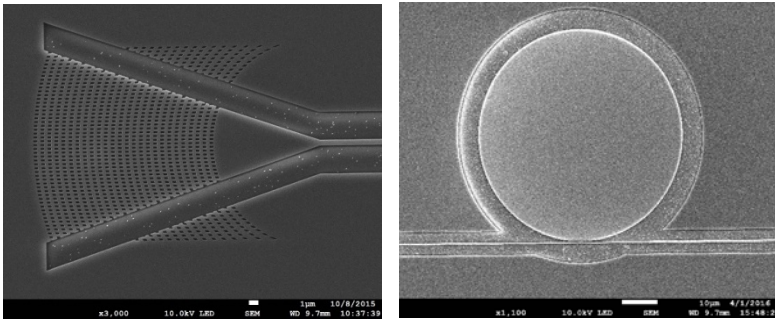


Fig. 5. (left) An integrated grating coupler for coupling light between fiber and on-chip silicon waveguide. (right) An integrated microring resonator with a bus waveguide.

#### 4. PUBLICATION AND AWARDS

J[1] Jingwen Ma, Xiang Xi, Zejie Yu, and Xiankai Sun, “Hybrid graphene/silicon integrated optical isolators with photonic spin-orbit interaction,” *Applied Physics Letters* 108 (15): 151103, Apr. 2016. [Featured as cover article and selected as Editor’s Pick]

C[1] Jingwen Ma, Xiang Xi, Zejie Yu, and Xiankai Sun, “Spin-orbit Interaction of Light in Photonic Nanowaveguides: A Proposal of Graphene-based Optical Isolators,” *PIERS 2016 in Shanghai*, The Electromagnetics Academy, Shanghai, China, Aug. 2016. (accepted)

# DEVELOPMENT OF HIGH-SPEED LASER SCANNING MICROSCOPE FOR IN VIVO DEEP BRAIN IMAGING

---

---

Principal Investigator: Professor Shih-Chi CHEN

*Department of Mechanical and Automation Engineering, CUHK*

Co-Investigator (if any): YUNG, Wing-Ho <sup>(2)</sup>

Research Team Members:

WALKER, Steven <sup>(2)</sup>, JIANG, Jun <sup>(1)</sup>

CHENG, Jiyi <sup>(1)</sup>, ZHANG, Dapeng <sup>(1)</sup>

<sup>(1)</sup> Dept. of Mechanical and Automation Engineering, CUHK

<sup>(2)</sup> School of Biomedical Science, CUHK

Project Start Date: 1 July 2014

Completion Date: 30 June 2016



## ABSTRACT

This proposal aims to develop new imaging techniques for custom-designed laser scanning confocal and two-photon excitation (TPE) microscopes, including (1) tunable frame rate and (2) omnidirectional imaging. Current microscopes typically run at a fixed frame rate with a flat imaging plane. However, all biological subjects are “3-dimensional (3-D)” in nature and various biological events, e.g. blood flow or neuron signaling, occur at different time scales. Accordingly, a versatile microscope with capabilities of frame-rate tuning and a 3-D programmable imaging plane is highly desirable. The frame-rate tuning function can be achieved by a new synchronization circuit and related software development. Omnidirectional imaging, i.e. 3-D programmable imaging plane, is achieved by the introduction of a high-speed piezoelectric objective scanner. During the in-plane raster scan procedure, the objective lens can be moved to any arbitrary position in the Z axis, thus enabling the “omnidirectional scan”. These new functions will be used to investigate deep regions in brain in vivo and enable many new studies that cannot be realized in the past. Specifically, we will follow neuron axons (not in the same plane) in a mouse brain and identify their related neural circuits and simultaneously observe their signaling processes at high frame rate, e.g. 30 -1000 fps. We will perform deep brain calcium imaging of visual and motor cortical columns (400-800 $\mu$ m deep) and record from multiple hypercolumns in a single scan. Lastly, we will study and image dendritic spines and track the formation and disappearance of individual spines. These results will generate significant impact by elucidating the learning processes involved in visuomotor tasks.

## 1. OBJECTIVES AND SIGNIFICANCE

The objectives of this project include the development of new imaging modalities and functions for the confocal and TPE microscopes as well as the in vivo imaging and study of mice using the new microscope functions. For the new imaging techniques, we aim to achieve the following performance specs:

- (a) Tunable frame rate between 30 – 17, 280 frames per second with a constant pixel dwell time.
- (b) A 3-D programmable imaging plane that can follow different biological structures in space in vivo, e.g. blood vessels/neurons, and work with different frame rates.

- (c) The microscope can be operated in both fluorescence and reflectance modes and in both upright and inverted configurations.
- (d) A microscope system suitable for deep brain high-speed imaging, i.e. 0.8-1.2mm (depth).
- (e) The microscope should achieve 0.2/0.6  $\mu\text{m}$  lateral/axial resolution.

For in vivo deep brain imaging and study on mice, we like to achieve the following:

- (a) Develop an adaptive algorithm to identify neurons and related neural circuits based on calcium imaging.
- (b) Perform deep brain calcium imaging of visual and motor cortical columns to depths of 0.8mm, and record from hypercolumns, 0.5mm across, in a single scan.
- (c) Image dendritic spines and track the formation and disappearance of individual spines, as well as overall spine density, as a measure of the plastic changes in neural connectivity.
- (d) Correlate the circuit activity and dendritic spine morphological changes to elucidate the learning processes involved in visuomotor tasks.

Most breakthroughs in biology and medicine are driven by the advancement of new diagnostic tools and novel instrumentations. The successful completion of this work will enable scientists to image, discover, and study new biological phenomena that have never been seen; for example, to image and follow neuron axons in a mouse brain in vivo and observe their signaling processes at ultra-high frame rate, e.g. 1000 fps, or to image cancer cell trafficking in vivo. For the proposed brain imaging experiments, visuomotor coordination is a central component of human interaction with the environment. It enables an individual to manipulate objects, defend against physical threat and is vital for survival. However, to date little is known about them due to limited instrumentation performance. Our new microscope system enables an unprecedented ability to identify and record neurons/circuits of interest over an arbitrary path/plane and large effective volume, at high temporal and spatial resolution. Elucidation of such circuits and the corresponding neural computation may reveal strategies for visuomotor training, as well as rehabilitation or compensatory therapies in disorders such as brain trauma or visuomotor ataxia. Successful demonstration of this system will have a wider impact in neuroscience research, in which many other higher mammalian functions mediated by other areas of the neocortex can be investigated beyond existing capabilities.

## 2. RESEARCH METHODOLOGY

1. Development of the (1) frame rate tuning and (2) omnidirectional imaging modalities.
2. A head-fixated 2-dimensional forelimb lever manipulation task: *To address the computational function of the motor cortex (M1), we first develop a behavioral test in which the extrinsic parameters, e.g. forelimb kinematics and kinetics, are precisely controlled. Accordingly, we custom-built a two degrees of freedom planar robotic lever with which mice could interact using a single forelimb while head-fixated under the imaging system. A pair of quadrature rotary encoders is used to sense the lever joint angles and then solved for the end effector position in real-time using MATLAB software. Two servomotors are used to perturb the limb motion and/or provide physical resistance. Together, this system enables precise acquisition of both intrinsic and extrinsic limb parameters, which we hypothesize to be encoded within the circuits of the motor cortex.*
3. In vivo imaging of M1 during motor performance and learning: *Mice undergo surgery for AAV viral injection and implantation of a cranial window and head-fixation plate. The mice are allowed to recover for 3-4 weeks while the transgene is expressed in neurons. We use the genetically encoded calcium indicator GCaMP6 to report calcium transients during neuronal action potential. GCaMP6 is also expressed in dendritic spines; the formation and elimination of which is a form of morphological plasticity and associated with motor learning. We perform chronic imaging of the motor cortex as the mice are trained to perform the above tasks, and thus be able to dissect neuronal*

population activities in terms of its immediate computation as well as its spatiotemporal changes over the duration of training.

### 3. RESULTS ACHIEVED

We present the major results in the following two sub-sections:

#### 3.1. High-speed omnidirectional imaging for two-photon microscopy

In the first year (2014-15) of the project, we have successfully developed the frame rate tuning module and installed it on the two-photon microscope for in vivo experiments. The module enables flexible frame rate tuning ranging from 30Hz to 17,280Hz. In our approach, the higher frame rates are obtained at the expense of reduced field of view (instead of adjusting the scanning speed of polygonal scanner). Hence, the number of photons from each pixel/point is the same as it runs at lower frame rates. In other words, the pixel dwell time does not change when frame rate is adjusted. This is important as in our system higher frame rates can be obtained without sacrificing the signal to noise ratio. However, it is worthy to note that as the same area is scanned more frequently at higher frame rates, specimens/tissue samples can be photo-bleached in a shorter amount of time. We have also carefully measured the point spread function of the multiphoton microscope to ensure the lateral and axial resolution achieves 0.2 and 0.6  $\mu\text{m}$  respectively. Preliminarily, we have explored the concept of omnidirectional imaging via a high-speed piezoelectric objective scanner (400  $\mu\text{m}$  stroke) with feed-forward control, which led to an SPIE Photonic West Poster Competition Award in the Multiphoton Microscopy session [C1]. Figure 1 shows an example of real time omnidirectional imaging via piezo-scanner.

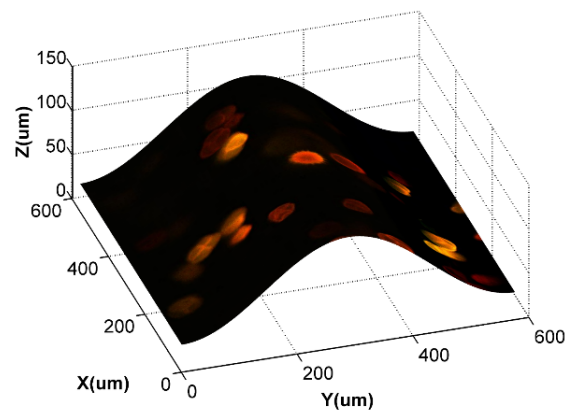


Figure 1: Pollen sample: An imaging plane is programmed to be sinusoidal

In the second year (2015-16), pursuing higher axial scanning speed, our team developed an ultra-high speed digital micromirror device (DMD)-based scanner, where binary holograms of spherical wavefronts of increasing/decreasing radii are programmed to the DMD to control the focal point of a femtosecond laser at the DMD pattern rate, i.e., 32.5 kHz [J1]. (The DMD is the chip used in an everyday projector that consists of several millions of binary micromirrors; it is generally considered a low-cost high-performance spatial light modulator.) **This is the fastest axial scanning method reported to date and has led to a pending U.S. patent [P1], which is presently licensed to a local company, Precision Instrument and Optics Limited for commercialization.** Figure 2 presents the optical configuration of our custom-built 3-D two-photon microscope integrated with the DMD-scanner.

Following axial scanning method, our team develops methods to perform 3-D random-access scanning based on the DMD-scanner [J2]. Since the DMD-scanner runs a 32.5 kHz, we have realized the most compact and simple two-photon microscope without any mechanical scanner—the DMD

arbitrarily control the focal point in space at 32.5 kHz, which is a ground breaking development. The new microscope system is presented in Fig. 3. The results have been featured in the news at the Faculty of Engineering at CUHK, “*The World’s Most Compact and Versatile Two-photon Microscope Enabled by a Low-cost DMD Chip, Realizing Ultrafast Random-access and 3D Imaging*” [1].

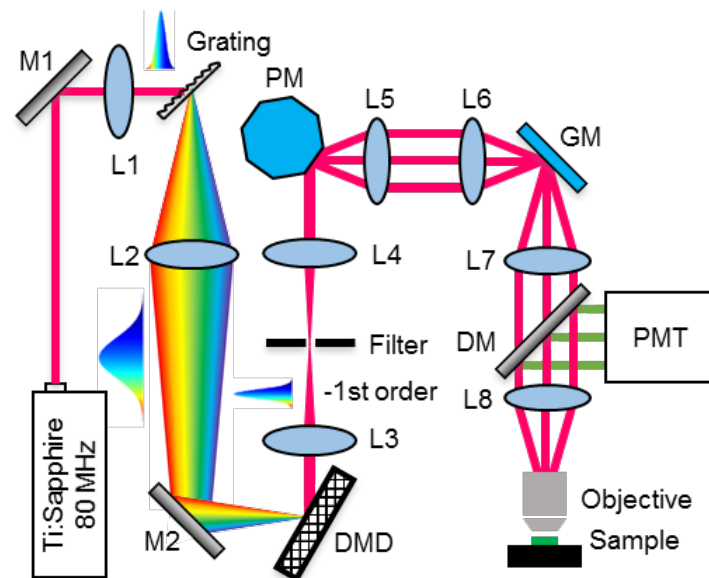


Figure 2: Optical configuration of the 3D TPE microscope; M1, M2: high-reflectivity mirrors; L1-L8: lenses; DM: dichroic mirror; PM: polygonal mirror scanner; GM: galvanometric mirror scanner

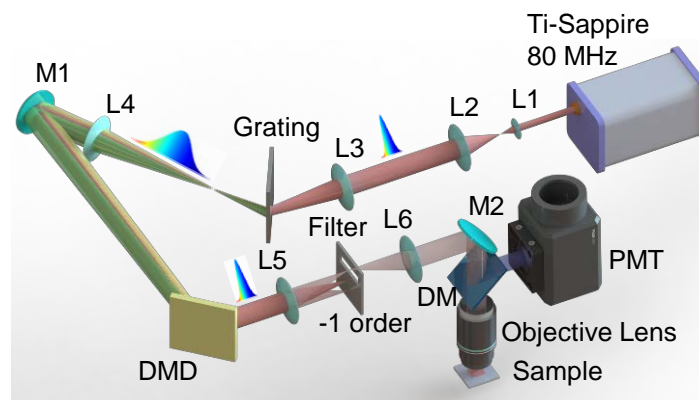


Figure 3: Optical configuration of the scanless TPE microscope based on a single DMD; M1, M2: high-reflectivity mirrors; L1-L6: lenses ( $f_{L1}$ ,  $f_{L2}$ ,  $f_{L3}$ ,  $f_{L4}$ ,  $f_{L5}$ ,  $f_{L6}$  = 50, 200, 100, 100, 200, and 200 mm respectively); DM: dichroic mirror; PMT: photomultiplier tube.

Figure 4 and 5 present example images obtained by the DMD microscope, including a pollen grain sample imaging at arbitrarily defined surfaces, i.e., spherical and sinusoidal surfaces, as well as randomly imaging, i.e., 6 selected points around the pollen, respectively. All images are collected and generated at the DMD pattern rate, i.e., 22.7 kHz.

Importantly, the DMD-scanner also enables precision 3-D resolved optical stimulation, which can be realized by simply extending the dwell time of the laser focus at any selected point in space; for example, a dwell time of 1 millisecond allows 80,000 laser pulses to impinge the specimen, providing sufficient power and speed to stimulate, blaze, or even cut individual cells or tissues.

Figure 6(a) – 6(c) present the selective optical stimulation results, where the selected seven spikes on the pollen are exposed to laser pulses for a total period of 0, 3, and 15 seconds respectively at low power level, i.e., 30 mW. From the results, one can clearly observe the effect of photobleaching, where the spikes no longer emit fluorescence signals and the adjacent areas remain unaffected.

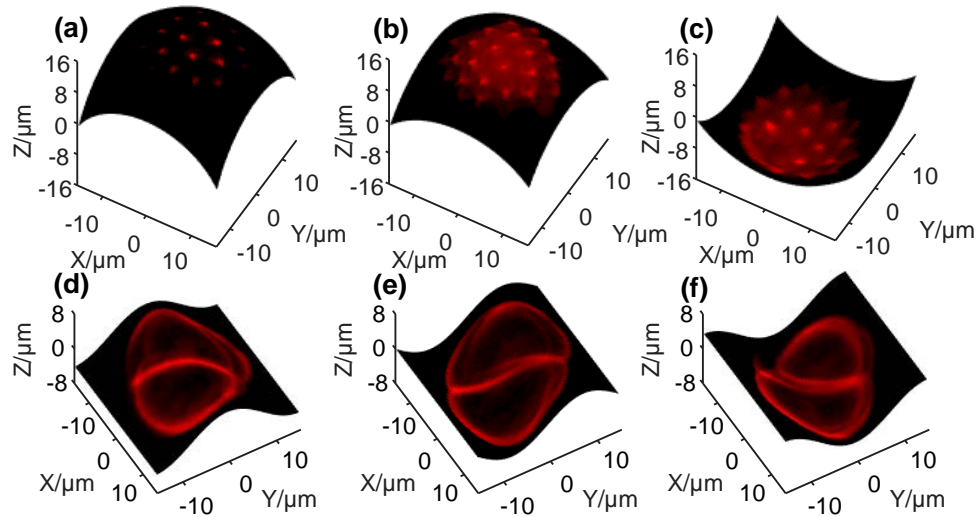


Figure 4: Cross-sectional images of two selected pollen grains on arbitrarily programmed spherical surfaces (a) - (c) and sinusoidal surfaces (d) - (f).

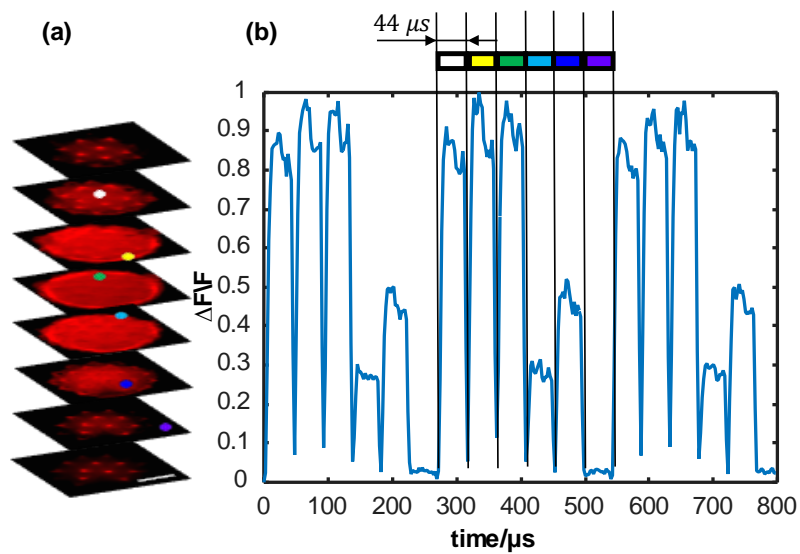


Figure 5: Random-access imaging experiments on a pollen grain: (a) eight imaged layers of the pollen grain, where six distant points are selected at different layers with color labels; the scale bar is 10  $\mu\text{m}$ ; (b) recorded voltages (i.e., fluorescence intensities) of the selected points; the color bar associates the fluorescence data to specific points in Fig. 4(a).

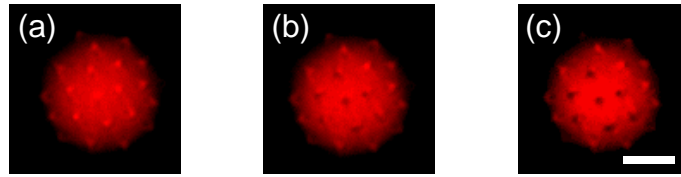


Figure 6: Photobleaching process of the seven selected spikes on the pollen grain for a total of (a) 0 second; (b) 3 seconds; and (c) 15 seconds; the scale bar is 10  $\mu\text{m}$ .

### 3.2. Forelimb manipulation system, mouse training, and in vivo brain imaging

In the first year (2014-15) of the project, we designed and characterized the mouse forelimb manipulation system (described in Section 2.2). Also, experiments and training procedures for the mice have been developed to ensure the mouse behavior can be recorded and clearly reflects the corresponding cue. Figure 7 presents the statistics of the mouse training processes; the results show a significantly improved success rate after a four-day training process. During the training, a blue LED presents a cue for up to 30 seconds, during which a mouse must move the lever in both X and Y directions above a fixed distance, e.g. 5mm. The successful completion of the task leads to the delivery of a 25 $\mu\text{L}$  sucrose reward.

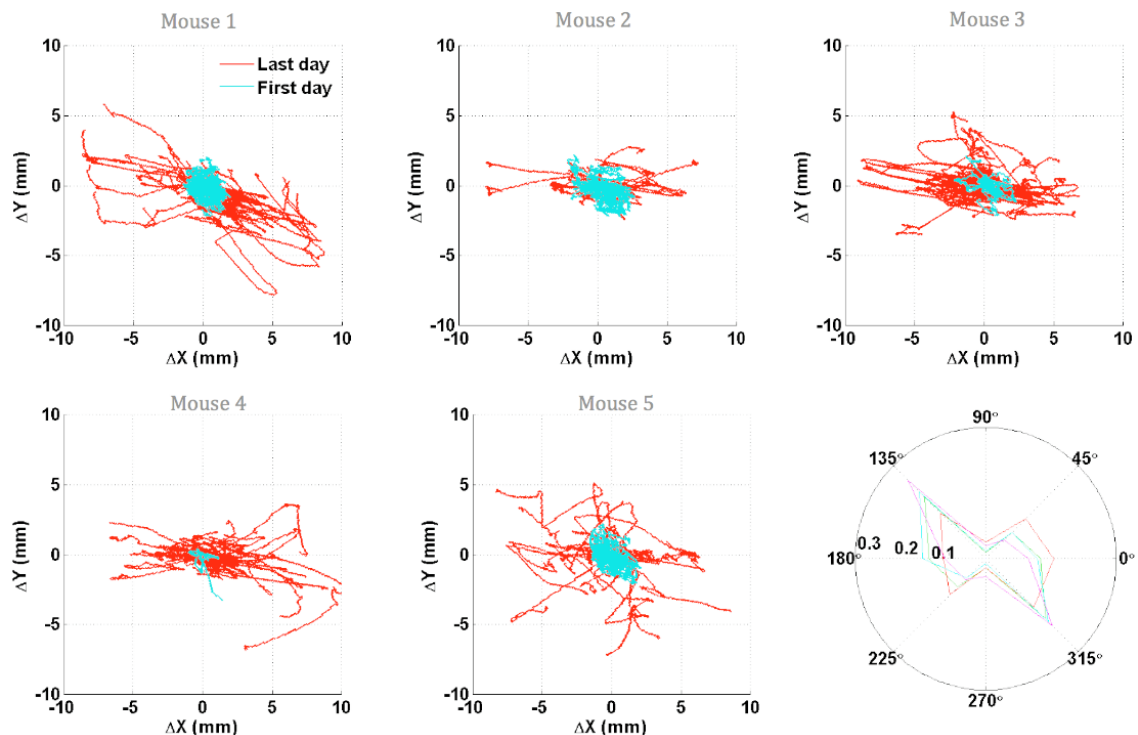
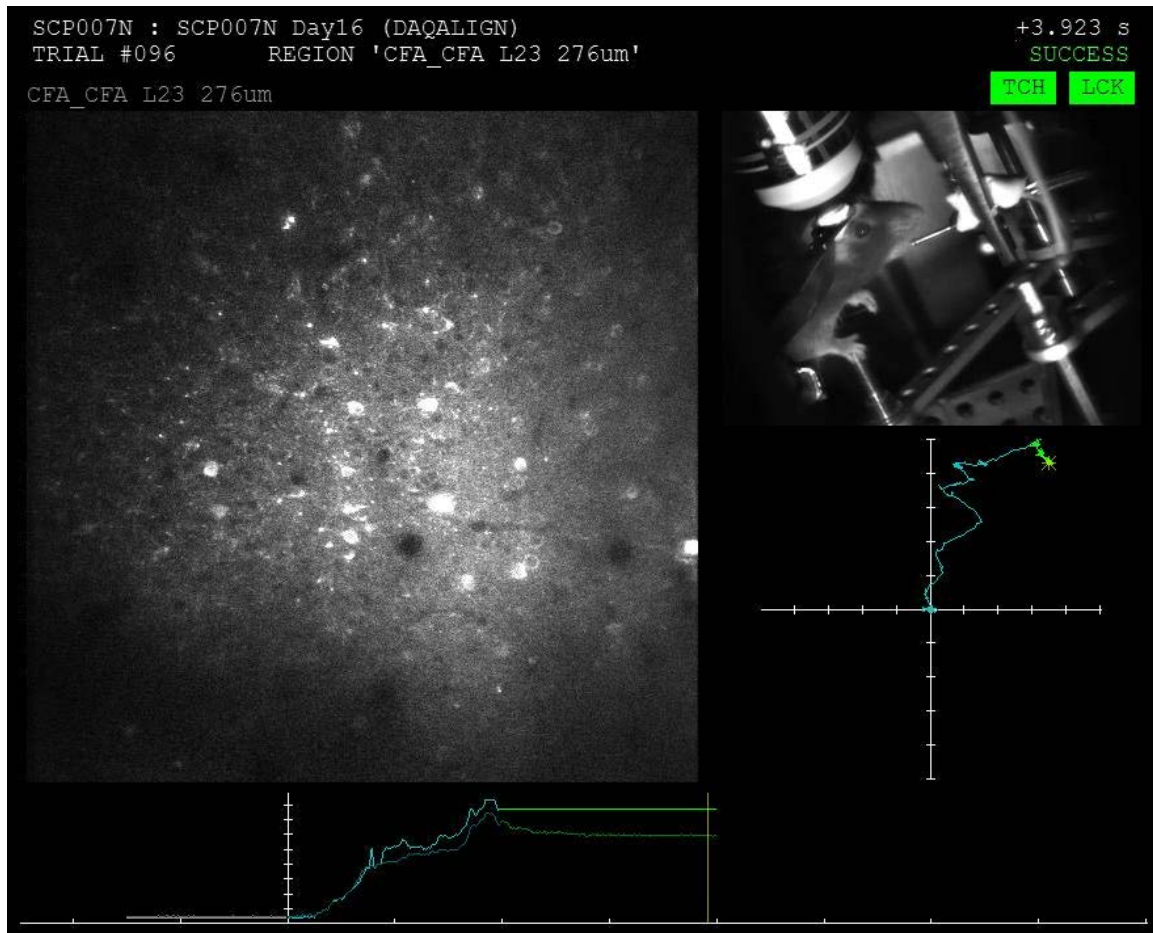


Figure 7: Training statistics of five mice over 4 training days, showing substantially improved success rate

In the second year (2015-16), our team has been focusing on integrating the two-photon microscope and the developed mouse forelimb manipulation system so that during a behavioral experiment, the neuronal activities in the mouse brain can be monitored in real time. Imaging processing algorithms have also been developed to realize simultaneous tracking of hundreds of neurons in real time.

Figure 8(A) shows a screenshot of the in vivo imaging experiments, where the mouse is trained to operate the 2-dimensional manipulandum with simultaneous in vivo two-photon calcium imaging. An infrared camera is installed in the enclosed experimental system to observe the mouse behavior in situ. Notably, the manipulandum telemetry is also shown on the screen in real time. Figure 8(B)

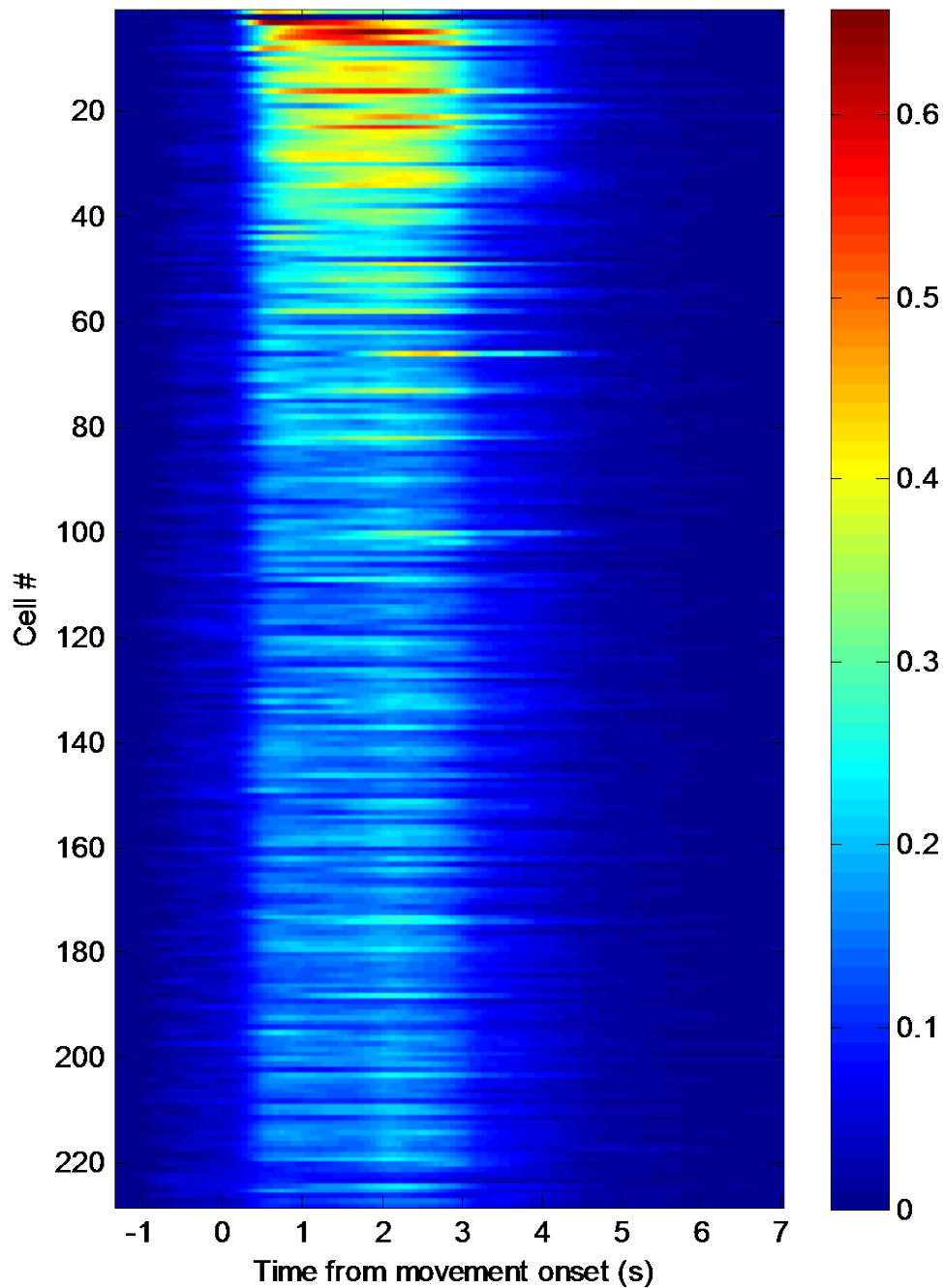
presents the corresponding neuronal activities recorded in real time, where the signals are the measured relative fluorescence ( $dF/F$ ) of calcium transients. In this particular experiment, activities of 228 individual neurons were monitored simultaneously. Figure 8 (C) presents the averaged relative fluorescence across 228 individual neurons, aligned to the onset of mouse movement. These results will be published in the near future.



A



B



C

Figure 8: (A) Representative in vivo acquisition trial of a mouse trained to operate a 2-dimensional manipulandum, with synchronized in vivo calcium imaging, infrared camera, and manipulandum telemetry; (B) relative fluorescence ( $dF/F$ ) of calcium transients extracted from the trial; and (C) averaged relative fluorescence across all trials in session for 228 individual neurons activity aligned to onset of movement.

In addition to mouse imaging experiments, our team has also performed brain imaging experiments on zebrafish in vivo via our custom-built two-photon microscope. Figure 9 presents optical cross-sectional images of zebrafish at frame rate of 100 frames per second. The results have been published in [J3].

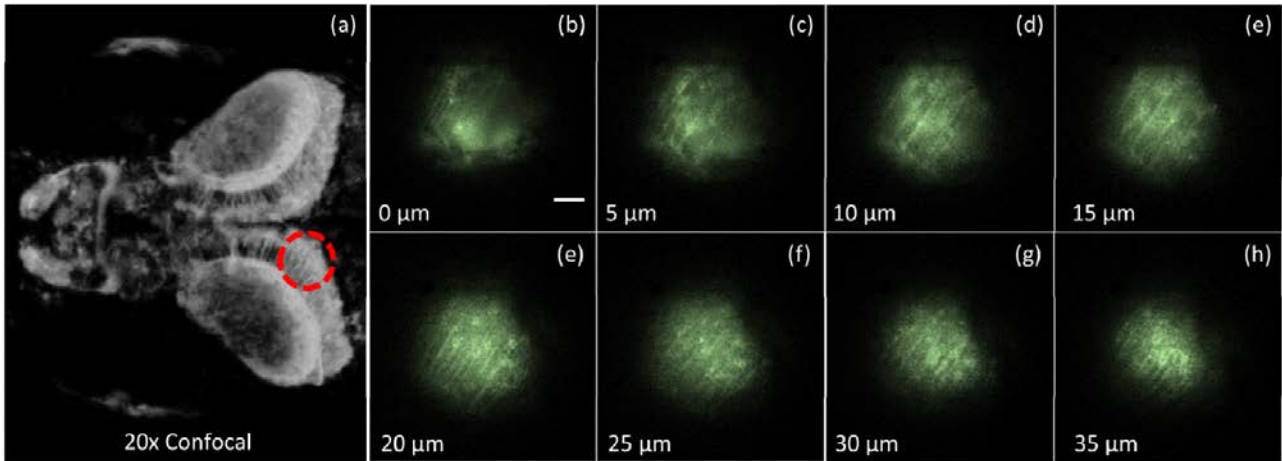


Figure 9: In-vivo two-photon  $\text{Ca}^{2+}$  imaging of zebrafish. Left: image of a 4dpf larva zebrafish head obtained by a confocal microscope. The red circle indicates a zoom-in area imaged using the two-photon temporal focusing microscope. Right: (b) - (h) fluorescence images from the temporal focusing microscope of the 4dpf zebrafish larva brain at different depths; the z position of each image is obtained by Fig. 3(b); and the magnification is re-scaled using Fig. 3(c); scale bar = 20  $\mu\text{m}$ ; pixels: 256  $\times$  256. Images were collected in the left hemisphere of the tectum opticum.

#### 4. PUBLICATION AND AWARDS

J[1] J. Cheng, C. Gu, D. Zhang, D. Wang, and S. Chen, “Ultrafast Axial Scanning for Two-photon Microscopy via a Digital Micromirror Device and Binary Holography,” *Optics Letters*, OSA, USA, Vol. 41, No. 7, pp. 1451-54, 2016.

J[2] Q. Geng, C. Gu, J. Cheng, and S. Chen, “Digital Micromirror Device-based Two-photon Microscopy for Three-dimensional and Random-access Imaging,” *Optica*, OSA, USA, Vol. 4, No. 6, pp. 674-677, 2017.

J[3] J. Jiang, D. Zhang, C. Gu, S. Walker, Y. Ke, W. Yung, and S. Chen, “Fast 3-D Temporal Focusing Microscopy Using an Electrically-tunable-lens,” *Optics Express*, OSA, USA, Vol. 23, No. 19, pp. 24362-68, 2015.

C[1] J. Cheng, D. Zhang, and S. Chen, “Multi-photon Laser Scanning Omnidirectional Imaging with Tunable Frame Rate”, *SPIE Photonic West*, San Francisco, SPIE, USA, February 7-12, 2015. (Poster Competition Award)

P[1] S. Chen, J. Cheng, C. Gu, and D. Zhang, The Chinese University of Hong Kong, “High-speed Binary Laser Beam Shaping and Scanning”, U.S. Utility Patent Application, No. 14/860,461, Sept 21<sup>st</sup>, 2015.

[1] <http://cloud.itsc.cuhk.edu.hk/enewsasp/app/article-details.aspx/57EBB283B0412F45F45F1573D1027D3D>

# MECHANISM FOR THE TRANSCYTOSIS OF TARGETED NANOPARTICLES ACROSS THE BLOOD-BRAIN BARRIER

Principal Investigator: Professor CHOI Chung Hang, Jonathan  
*Department of Biomedical Engineering, CUHK*

Research Team Members:

Dr. ZHANG Lei, Dr. CHEN Zhong,  
 Miss YANG Hongrong, Mr. CHOI Chun Kit,  
 Miss LIU Yao, Miss HO Lok Wai Cola <sup>(1)</sup>

<sup>(1)</sup> Dept. of Biomedical Engineering, CUHK

**Project Start Date: 1 July 2014**  
**Completion Date: 30 June 2016**



## ABSTRACT

Delivery of therapeutics to the brain represents a significant challenge. Unlike small molecules such as nutrients or metabolic wastes, nanoparticles (NPs) cannot easily penetrate through the blood-brain barrier (BBB) and accumulate in the brain. One non-invasive approach to directing intravenously administered NPs across the BBB involves the attachment of ligands on the surface of nanoparticles for engaging receptors on the surface of brain endothelial cells. In this project, we have developed a novel class of NPs that can first activate the  $A_{2A}$  adenosine receptor ( $A_{2A}$  AR, tight junction signaling protein) through ligand-receptor interactions, penetrate through the BBB, and finally enter neurons *in vitro*. Specifically, these NPs contain gold nanoparticles (AuNPs) as cores, a thin polydopamine (PDA) layer as neuron-targeting coating, and poly (adenylic acid) (poly (A)) oligonucleotides (single strand DNA) as surface ligands to activate  $A_{2A}$  AR receptor and open the tight junction between endothelial cells of BBB. We delineate the effectiveness of such NPs by achieving these milestones: 1) Construction of targeted NPs with functional coatings; 2) Investigation of underlying mechanism that governs the cellular entry of targeted DNA-coated NPs; 3) Proof of DNA (poly (A)) effectively increasing the permeability of BBB *in vitro* and entering Neuro 2A cells (mouse neuroblastoma); and 4) Elucidation of *in vivo* organ-level and cellular-level distribution of systemically injected DNA-coated NPs. Our future work will focus on the intracranial distribution of DNA-coated NPs and *in vivo* imaging.

## 1. OBJECTIVES AND SIGNIFICANCE

In this progress report, our team have achieved the following three objectives.

### Objective 1: Fabrication of targeted nanoparticles (NPs)

- Preparing functional NPs (*i.e.*, DNA-coated NPs, alkyl-coated NPs, DNA- and PDA-coated NPs) targeting a specific cell type (e.g., brain endothelial cells, keratinocytes, neurons, macrophages)

### Objective 2: Probing the cellular uptake properties of targeted NPs *in vitro*

- Deciphering the cellular uptake mechanism of NPs containing different types of targeting ligands (*i.e.*, DNA oligonucleotides and long alkyl chains)
- Delineating the cellular uptake behaviors of PDA-coated AuNPs by tuning the PDA polymerization time and monomer concentration
- Monitoring the uptake of DNA (poly(A))- and PDA-coated AuNPs in a non-contact, *in vitro* model of

brain endothelial cells closely packed to mimic the BBB

### Objective 3: Investigating the *in vivo* properties of DNA-coated NPs

- Demonstrating the organ-level and cellular-level distribution of DNA-coated NPs *in vivo*

Our fundamental studies of “bio-nano” interactions between the targeted NPs with functional coatings and mammalian cells provide mechanistic insights into drug delivery carriers based on these prevalent natural biomolecules. In light of these basic mechanism investigations, the as-prepared poly (A)- and PDA-coated AuNPs exhibit promising capability in crossing the BBB and achieving transendothelial targeting by *in vitro* non-contact model. Our results will guide the design of more effective NP-based agents to non-invasively treat and image brain-related diseases, such as cancer, stroke, and other neurodegenerative or psychiatric diseases.

## **2. RESEARCH METHODOLOGY**

### **Synthesis of oligonucleotide**

Thiolated DNA oligonucleotides were synthesized by an automated synthesizer (Azco Biotech) using standard solid-phase synthesis and reagents. All oligonucleotides were purified using a high performance liquid chromatography instrument (HPLC, Agilent) with a Microsorb C18 column (Varian).

### **Preparation of DNA-coated gold nanoparticle conjugates (DNA-AuNPs)**

To modify nanospheres with DNA oligonucleotides, the gold-DNA mixture was manually shaken for a few seconds and tuned to 0.01% SDS. Concentrated NaCl solution (5 M) was sequentially added to the NP solution at time intervals of 30 min up to a final concentration of 0.7 M to achieve dense coverage of the NP surface with DNA. The DNA-AuNPs were purified by centrifuging them for three times.

### **Preparation of DNA-coated superparamagnetic iron oxide nanoparticles (DNA-SPIONs)**

Carboxylate-coated SPIONs (PEG-SPIONs) were synthesized by thermal decomposition of ferric acetyl-acetonate ( $\text{Fe}(\text{acac})_3$ )<sub>2</sub>, and later purified and lyophilized. Amine-modified DNA oligonucleotides were attached to PEG-SPIONs *via* DCC/NHS chemistry. Typically, 5 mg PEG-SPIONs was dissolved in 0.5 mL DMSO and activated with 20  $\mu\text{mol}$  DCC and NHS for 2 h. Next, 6 nmol DNA was added to the mixture and left to stir overnight. The DNA-coated SPIONs (DNA-SPIONs) were dialyzed against Nanopure water by a centrifugal filter (molecular weight cutoff size: 50000) for at least three times.

### **Preparation of Alkyl-Terminated PEG-Coated NPs**

Citrate-capped AuNPs of 25 nm in diameter were prepared by an established seed-mediated growth method. The carboxyl group of the bifunctional polyethylene glycol (PEG) linker, HS-PEG5000-COOH was activated and conjugated to hexylamine, dodecylamine, or octadecylamine by EDC/NHS chemistry. To prepare alkyl-terminated, PEG-coated AuNPs (alkyl<sub>x%</sub>-PEG-AuNPs), an aqueous suspension of AuNP solution was mixed with x mol % of HS-PEG5000-C<sub>n</sub>H<sub>2n+1</sub> and (100 – x) mol % of HS-PEG<sub>5000</sub>-OCH<sub>3</sub> by keeping the total PEG concentration at 20 PEG molecules per nm<sup>2</sup> of gold surface to be coated. All PEGylation reactions lasted for 1 h with sonication, followed by purification by 5 rounds of centrifugation at 13,000 rpm for 15 min and resuspension in deionized water.

### **Preparation of polyA- and PDA-coated gold nanoparticles (polyA-PDA-AuNPs)**

Citrate-capped AuNPs were functionalized by polyethylene glycol molecules (m-PEG1000-SH) by forming a strong Au-S binding first to keep the stability of AuNPs. Next, monomeric dopamine (DA-HCl) was added under alkaline conditions (Tris buffer; pH = 8.5) to induce self-polymerization. Poly (A) oligonucleotides, either linear or hairpin in shape, were added into PDA-coated AuNPs. The mixture was allowed to incubate at room temperature for 1 h. Excess DNA strands were removed by centrifugation.

### **Cell culture and the non-contact *in vitro* BBB model (Transwell assay)**

All cells (*i.e.*, C166, RAW 264.7, bEnd.3, Neuro 2A) were grown in a 10 cm tissue culture dish at 37 °C with 5% CO<sub>2</sub>. The growth medium consists of Dulbecco's Modified Eagle's Medium (DMEM) supplemented with 10% v/v fetal bovine serum (FBS) and 1% v/v penicillin–streptomycin. The non-contact *in vitro* BBB model

was conducted in the Transwell assay that consists of two monolayers of cell in the apical chamber and basal chamber, respectively (Figure 3B). The brain endothelial cell (bEnd.3) monolayer was placed at the apical chamber and the monolayer neuroblast (Neuro 2A) was placed at the basal chamber.

### **Cellular uptake and inductively coupled plasma mass spectrometry (ICP-MS)**

During the experiment, the cells were incubated with a certain concentration of NPs. At different time points, the NPs were removed, and the cells rinsed by PBS twice and trypsinized. Cell pellets were collected by centrifugation at 4000 rpm for 5 min. Cell pellets were digested by 0.25 mL of *aqua regia* overnight, and diluted to 10 mL by the matrix solution (2% HCl, 2% HNO<sub>3</sub>, with 10 ppb indium as internal standard) for ICP-MS measurements (Agilent). The number of NPs in each resultant solution was obtained by computing metal content (*i.e.*, Au or Fe) of known concentrations.

### **TEM imaging for cells**

For TEM imaging, freshly harvested cell pellets were fixed with 2.5% glutaraldehyde for 2 h and then stained by 1% osmium tetroxide for another 2 h. Pellets were gradually dehydrated in increasing ethanol gradients and propylene oxide, and later embedded in Epon 812 resins (Electron Microscopy Sciences; EMS) and finally polymerized at 55 °C for 48 h. Ultrathin sections of around 70 nm in thickness were deposited onto 200-mesh copper grids and stained with 4% uranyl acetate (in 50% methanol) and Reynolds lead citrate for observation under TEM (Hitachi H7700) at a beam voltage of 100 kV.

### **Immunofluorescence**

After treatment of NPs, cells were then rinsed with PBS, fixed with pre-cooled methanol at -20 °C for 10 min, and switched to cooled acetone for another 1 min. Next, cells were blocked with 2% BSA in PBS at RT for 1 h. Cells were stained with a primary antibody (5 µg/mL in 1% BSA) against the protein of interest overnight at 4 °C. After rinses with 0.05% Tween-20 in PBS, cells were stained with an AlexaFluor 488-labeled secondary antibody (2 µg/mL in 1% BSA) for 1 h at RT. DAPI was used to stain the nuclei of the cells. Samples were visualized under a fluorescence microscope with DAPI and FITC filter.

## **3. RESULTS ACHIEVED**

### **Fabrication of DNA-coated NPs and investigation into their interactions with cells**

We first investigated the cellular uptake mechanism of DNA-coated NPs. DNA-coated AuNPs and DNA-coated SPIONs were chosen to serve this purpose. By exploring how DNA-coated AuNPs with four different aspect ratios (ranging from 1 to 7, *i.e.*, AR=1, 2, 4, and 7) interact with C166 cells (mouse endothelial), we surprisingly observed an optimal aspect ratio that maximizes their cellular uptake (*i.e.*, short nanorods of aspect ratio around 2), a different trend from their untargeted/PEGylated counterparts. Besides, regardless of aspect ratio, we found that DNA oligonucleotides on gold surface will engage Class A scavenger (SR-A) receptors on cell surface to enter the cells, evidenced by significant decrease (60-90%) in cellular uptake after pre-treatment by fucoidan (FCD), a known pharmacological inhibitor of SR-A (Figure 1A). Also, we prepared DNA-coated superparamagnetic iron oxide nanoparticle (DNA-SPION): To the surface of a SPION core coated with poly(ethylene glycol) (PEG) strands that bear carboxylate groups (HOOC-PEG-SPION) at their distal ends, single-stranded amine-terminated DNA oligonucleotides (ssDNA-NH<sub>2</sub>) are covalently conjugated *via* EDC/NHS chemistry. By incubating RAW 264.7 cells (macrophage) with DNA-SPIONs with FCD, filipin III (an inhibitor of lipid raft/caveolae) and cytochalasin D (an inhibitor of actin), we found that the cellular uptake was greatly suppressed (Figure 1B), indicating that internalization process involves multiple pathways. However, after transfection with siMSR1 (knockdown class A macrophage scavenger receptor), siFLOT1 (knockdown Flotillin-1) and siCAV1 (knockdown caveolin-1), we found that the cellular uptake decreases drastically with genetic suppression of MSR1 (Figure 1C), hence proving that SR-A still significantly mediates the cellular uptake of DNA-coated nanorods (Yang H et al., *Small*, 2016).

Thanks to the support by SHIAE, we also examined another type of bionanomaterials besides DNA-coated

NPs and further explored their interactions with cells, namely alkyl-terminated NPs. Specifically, we evaluated the role of alkyl group ( $-C_nH_{2n+1}$ ), a prevalent functional group in bionanomaterials, in “bio-nano”. By exposing densely PEGylated gold nanoparticles (PEG-AuNPs) that bear alkyl chains of different carbon chain lengths (*i.e.*,  $n=6, 12, 18$ ) to Kera-308 keratinocytes, we found that dodecyl-PEG-AuNPs ( $n = 12$ ) and octadecyl-PEG-AuNPs ( $n = 18$ ) can enter Kera-308 cells 30-fold more than methoxy-PEG-AuNPs (no alkyl groups) and hexyl-PEG-AuNPs ( $n = 6$ ) with an alkyl mass percentage as modest as 2% in PEG shell. Such strong “alkyl chain length” dependence is valid for both serum-free and serum-containing (up to 10% fetal bovine serum) cell culture media. In addition, we provided evidence to prove these alkyl-PEG-AuNPs enter cells *via* the filipodia-mediated pathway and adopt the “endo-lysosomal” route of intracellular trafficking (Figure 1E). These results are potentially useful for designing alkylated NPs for crossing the BBB (Ho LWC et al., *ACS Nano*, 2017).

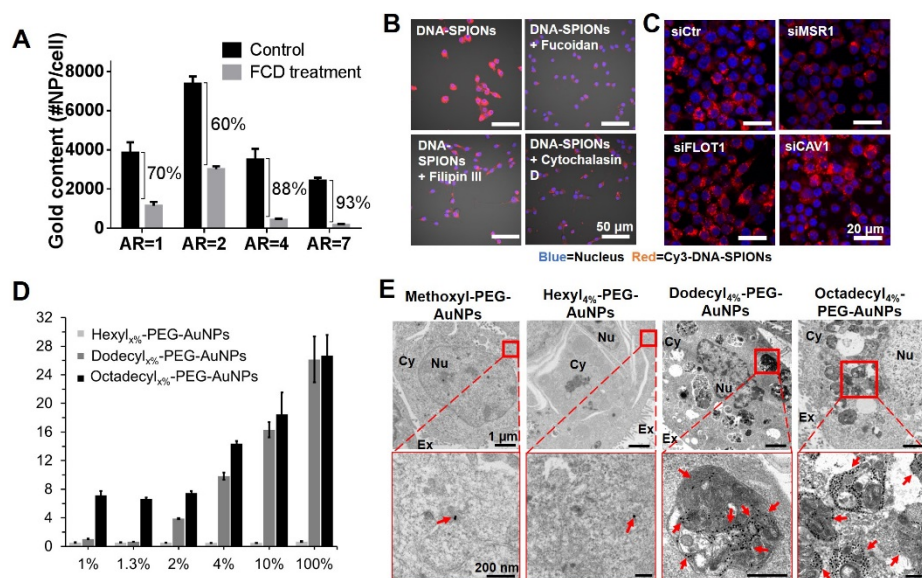


Figure 1. Cellular uptake mechanism of various targeted NPs. (A) Cellular association of DNA-coated AuNPs of different aspect ratios (AR=1, 2, 4 and 7) with and without fucoidan (FCD) treatment in C166 cells. Confocal imaging of RAW 264.7 cells incubated with Cy3-labeled DNA-SPIONs (red) pre-treated with (B) fucoidan, filipin III, and cytochalasin D, or transfected with (C) siMSR1, siFLOT1 and siCAV1, respectively. Cells transfected with non-targeting siRNA (siCtr) serve as negative control. (D) Cellular uptake of alkylx%-

PEG-AuNPs containing different mole ratios of hexyl, dodecyl, or octadecyl groups in the PEG coating by Kera-308 cells (mouse keratinocytes). (E) Representative TEM images of cells. Dodecyl<sub>4%</sub>-PEG-AuNPs and octadecyl<sub>4%</sub>-PEG-AuNPs can enter the cell more pronouncedly than methoxy-PEG-AuNPs and hexyl<sub>4%</sub>-PEG-AuNPs, mostly accumulating inside organelles (red arrows). The bottom row shows the enlargement of the boxed area of the top row. (Legend: Nu = nucleus; Cy = cytosol; and Ex = extracellular space.)

## Monitoring the uptake of DNA (poly(A))- and PDA- coated AuNPs in a non-contact *in vitro* BBB model

Monomeric adenosine is reported as the activating agent of  $A_{2A}$  AR on the extracellular surface of brain endothelial cells of BBB. Therefore, poly(A) oligonucleotides (A30) either in linear or hairpin shape are designed to be coated onto the NP surface. The hairpin shape was suggested to increase the specificity of the fluorescently-labeled poly (A) on targeting  $A_{2A}$  AR. We chose the overall NPs to be 30 to 35 nm in diameter for the following reasons: 1) Our previous work demonstrated that NPs of diameter under 40 nm accumulate for longer time in blood circulation system; 2) The most effective size for NPs bind to Neuro 2A (mouse neuroblast) is around 45 nm in diameter. Therefore, the whole nanostructure consists of gold core of 10 nm in diameter, PDA shell of 10 nm in thickness, and poly(A) strands immobilized on the periphery. After incubating the bEnd.3 cells with as-prepared NPs, we observed by fluorescence microscopy that only NPs immobilized with either hairpin or linear poly(A) oligonucleotides and EDTA, which deactivates membrane proteins (positive control), can create holes in the endothelial cell layer (Figure 3A), indicating that

polyA-PDA-AuNPs (both linear and hairpin DNA) disrupt the tightly packed endothelial cells. In contrast, PEG-coated AuNPs and PDA-coated barely open any junctions. Strikingly, the hairpin and linear poly(A) strands do not show significant difference in effectiveness of opening the tight junctions.

The non-contact *in vitro* BBB model (Transwell assay, Figure 2B) consists of one monolayer of bEnd.3 cells (brain endothelial) in the apical chamber and one monolayer of Neuro2A cells (neuroblast) in the basal chamber. The transendothelial permeability is reflected by transendothelial cell electrical resistance (TEER) value. Since the endothelial cell monolayer acts like an electric insulator, the endothelial membrane electrical potential remains high if the cells keep tightly packed. Once opening pores between endothelial cells are created, aqueous solutes and water will be able to cross the monolayer, resulting in decrease of TEER. We employed TEER recorder to measure the TEER value of blank chambers. From the relative TEER values in Figure 3C, we found that only the brain endothelial cells treated with polyA-PDA-AuNPs and EDTA (positive control) induce significant decrease in relative TEER value (membrane potential difference) after 24 hours, while PEG-coated and PDA-coated counterparts only show modest decrease. The result suggests that tight junctions of BBB are successfully disrupted and the permeability of BBB increases. In addition, we observed that the relative TEER values of the samples treated with polyA-PDA-AuNPs can rebound to ~80% of the original value after removing NPs for 1 hour, and totally recover after 6 hours, demonstrating the self-recovery of tight junctions. In contrast, cells treated with EDTA cannot (even after 24 hours) due to high cytotoxicity of EDTA to cells. In conclusion, our PolyA-PDA-AuNPs can facilitate the opening of tight junctions between adjacent brain endothelial cells of BBB layer and increase in the permeability of the *in vitro* BBB model.

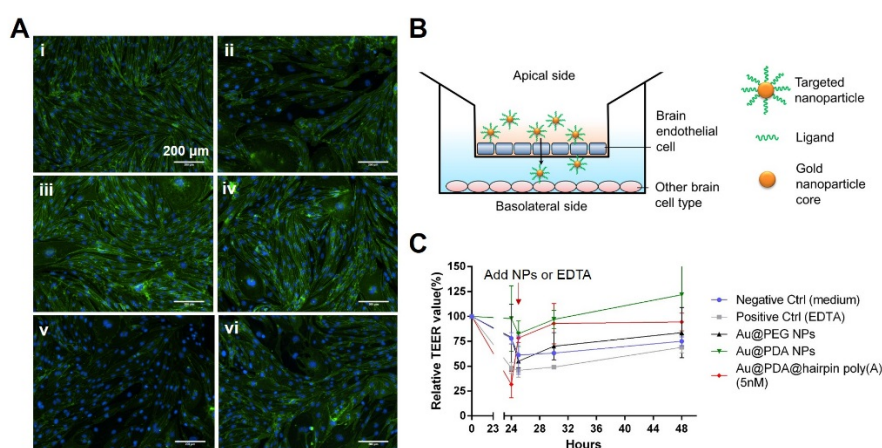


Figure 2. Poly(A)-PDA-AuNPs successfully increase the permeability of the *in vitro* BBB model. (A) Fluorescent images of bEnd.3 cells treated with (i) medium only (negative control), (ii) EDTA (positive control), (iii) PEG-AuNPs, (iv) PDA-AuNPs, (v) linear-poly(A)-PDA-AuNPs, (vi) hairpin-poly(A)-PDA-AuNPs. Green= Claudin-5 (tight junction protein), Blue=Nuclei

(B) Schematic illustration of the non-contact *in vitro* culture model (Transwell assay). (C) Regulation of BBB permeability via hairpin-poly(A)-PDA-AuNPs. TEER values were measured immediately before and after 1 h, 6 h, 24 h of addition of NPs.

### ***In vivo* organ-level distribution of DNA-coated NPs**

We next investigated the *in vivo* properties of DNA-coated NPs. By injecting DNA-SPIONs into mice and continuously monitoring the iron content in blood for 24 hours, we first concluded that PEG-SPIONs ( $t_{1/2}=0.33$  h) show faster blood clearance than DNA-SPIONs ( $t_{1/2}=1.03$  h) (Figures 3A-B). By ICP measurements, we calculated the iron NP accumulation in different organs. Throughout the entire 24 h observation window, the liver and spleen show the highest NP accumulation for both PEG- and DNA- coated NPs. Particularly, DNA- coated SPIONs tend to accumulate more in spleen and pancreas (Figures 3C-D) *Ex vivo* near-infrared fluorescence (NIRF) imaging of intravenously (i.v.) injected with Cy5.5-tagged PEG-SPIONs and Cy5.5-tagged DNA-SPIONs largely confirms the different distribution patterns for the two

types of SPIONs (Figure 3E). Thanks to the support of SHIAE, our data shed light on the *in vivo* application of DNA-coated NPs. In the future, we will obtain the *in vivo* intracranial distribution of poly(A)-PDA-AuNPs in animal models.

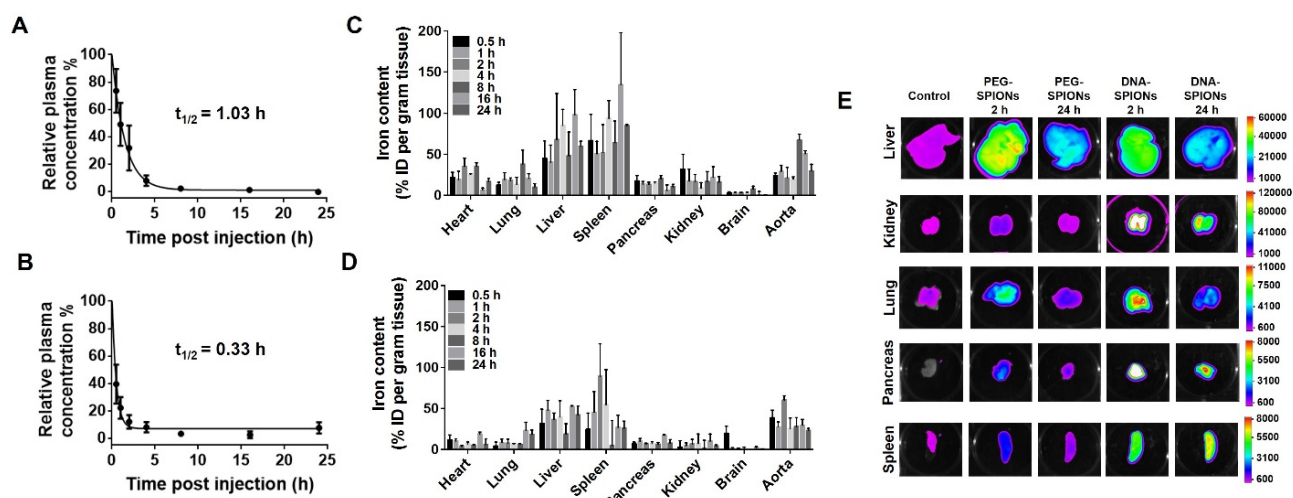


Figure 3. Blood pharmacokinetics and organ-level distribution of PEG-SPIONs and DNA-SPIONs in mice. By ICP measurements of the iron content in blood, (A) PEG-SPIONs show slower blood clearance than (B) DNA-SPIONs. By ICP-OES analysis, the liver and spleen show the highest iron contents for both (C) DNA-SPIONs and (D) PEG-SPIONs. (E) *Ex vivo* NIRF imaging of organs collected from the injected mice. The liver and kidneys show stronger Cy5.5 signals than other organs. 2 h post injection, the NIRF Cy5.5 signals in the kidneys, lung, and pancreas are strong, but become attenuated after 24 h of injection.

### ***In vivo* cellular-level distribution of DNA-coated NPs**

Besides organ-level distribution data, we also investigated the cellular-level distribution of the systemically injected DNA-coated NPs in mice by flow cytometry. Here, the PEG-coated NPs serve as negative control in the sense that they cannot target SR-A unlike the DNA-coated NPs. In conclusion, the same cell type located in different organs exhibit different degrees of cellular uptake *in vivo*. Notably, after 2 h of injection, DNA-coated NPs can enter M2 macrophages and dendritic cells inside both the aorta and spleen more than PEG-coated NPs. These results offer important fundamental insights into the use of DNA nanostructures for *in vivo* targeting.

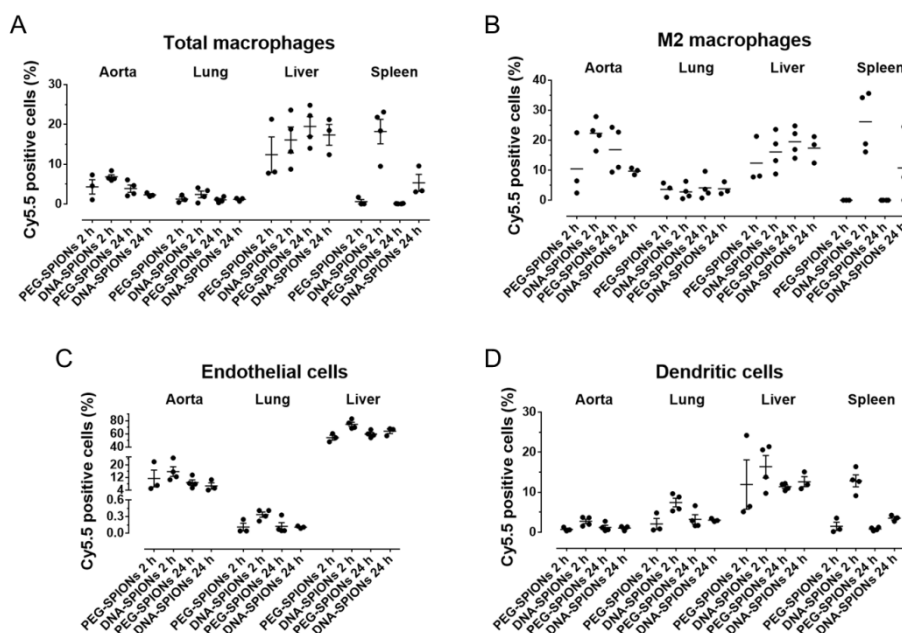


Figure 4: Cellular-level distribution of PEG-SPIONs and DNA-SPIONs in mice. 2 h and 24 h post injection of Cy5.5-labeled PEG-SPIONs or DNA-SPIONs, different cell types [including (A) total macrophages, (B) M2 macrophages, (C) endothelial cells, and (D) dendritic cells] collected from the aorta, lung, liver, and spleen were analyzed by flow cytometry, and the percentage of Cy5.5-positive cells ascertained. Error bar indicates the standard error resulting from at least 3 animals per group. Macrophages (especially M2 macrophages) in the aorta and spleen internalize DNA-SPIONs more readily than PEG-SPIONs 2 h post injection. Both endothelial cells and dendritic cells in the aorta, liver, and spleen internalize DNA-SPIONs more readily than PEG-SPIONs.

#### 4. PUBLICATIONS AND AWARDS

1. Ho LWC, Yung WY, Sy KHS, Li HY, Choi CKK, Leung KCF, Lee TWY, Choi CHJ\*. "Effect of alkylation on the cellular uptake of polyethylene glycol-coated gold nanoparticles". *ACS Nano*, **11**, 6, 6085-6101 (2017).
2. Yang H, Chen Z, Zhang L, Yung WY, Leung KCF, Chan HYE, Choi CHJ\*. "Mechanism for the cellular uptake of targeted gold nanorods of defined aspect ratios". *Small*, **12**, 37, 5178-5189 (2016).
3. Choi CKK, Li J, Wei K, Xu YJ, Ho LWC, Zhu M, To KWK, Choi CHJ\*, Bian L\*. A gold@polydopamine core-shell nanoprobe for long-term intracellular detection of microRNAs in differentiating stem cells. *J. Am. Chem. Soc.*, **137**, 23, 7337-7346 (2015).

Croucher Innovation Award 2016: Site-specific delivery of nanoparticles: From basic investigations to biomedical applications (PI: Prof. CHOI Chung Hang Jonathan)

# DEVELOPMENT OF THE NEXT GENERATION NEUROSURGICAL ASSISTANT SYSTEM BASED ON FUNCTIONAL BRAIN MAPPING

Principle Investigator: Professor Defeng WANG <sup>(1,4)</sup>  
*Department of Imaging and Interventional Radiology, CUHK*

Co-Investigator: Winnie Chiu-wing CHU <sup>(1)</sup>, Kwok Chu WONG <sup>(2)</sup>, Lin SHI <sup>(1,3)</sup>  
 Research Team Members: LIU Kai, PhD Student <sup>(1,4)</sup>, SUN Xiaofei, MPhil Student <sup>(1,4)</sup>

<sup>(1)</sup> Dept. of Imaging and Interventional Radiology, CUHK

<sup>(2)</sup> Dept. of Neurosurgery, CUHK

<sup>(3)</sup> Dept. of Medicine and Therapeutics, CUHK

<sup>(4)</sup> Dept. of Biomedical Engineering and Shun Hing Institute of Advanced Engineering, CUHK



Project Start Date: 1 July 2013

Completion Date: 30 June 2015

## ABSTRACT

The aim of the project was to develop a new generation of neurosurgical assistant system based on functional brain mapping. Many existing methods were developed for adults, not suitable for children with altered functional connectivity across different developmental age. The proposed navigation system was able to perform on multiple age groups with the functional network templates and pediatric brain atlas based on Chinese population constructed in this project. Several techniques to improve image quality and data processing were investigated included image de-noising, parallel computing and data normalization. The brain activity, background network efficiency, topological organization, default mode network and functional connectivity were studied on patients with neurodegenerative or neuro-disordered diseases. Testing data and results of functional mapping were integrated and implemented into the navigation system with the electromagnetic tracking device for neurosurgical planning. The proposed system could help to enhance surgical planning and navigation to improve the efficiency and safety of the clinical neurosurgery to decrease the risk of functional deficits after neurosurgery. Techniques and testing results were presented in public conferences and peer-reviewed journal articles. Video demonstration and tutorial of the system were recorded and available for clinical personnel.

## 1. OBJECTIVES AND SIGNIFICANCE

- [1] To identify the functional areas before neurosurgical removal of brain lesion to prevent risk of functional deficits
- [2] To determine the correlated functional regions with advanced sparse representation model
- [3] To develop a functional network templates and atlas in multiple age groups
- [4] To perform data acquisition and preprocessing procedure for young children
- [5] To determine the functional correlated regions from high dimensional rsfMRI
- [6] To develop a computational system based on functional brain mapping to guide neurosurgical planning and provide a precise navigation in clinical neurosurgery
- [7] To increase the accuracy in removing brain lesion and avoid unnecessary removal to retain the maximum brain function as much as possible

## 2. RESEARCH METHODOLOGY

The proposed project included data acquisition and preprocessing, detection of correlated regions, network templates construction, automatic identification of functional networks, development of navigation system, system validation and testing. Pediatric brain templates and atlas were developed for the purpose of mapping functional brain areas. They were able to provide accurate brain mapping for children who underwent functional MRI. The aim of creating the templates and atlas was to identify the functional areas of the brain before neurosurgery to avoid potential damage to be done on important cortical areas. Besides the structure, brain activity, network efficiency, topological organization, default mode network and functional connectivity were also studied to provide more accurate data for the navigation system for neurosurgical planning. The navigation system was developed mainly by C++, based on the obtained data from brain atlas, functional brain mapping, connectivity, network efficiency etc.

### 2.1 Data acquisition and preprocessing

The resting state functional magnetic imaging (rsfMRI) was conducted at the Huashan Hospital in Shanghai and the Prince of Wales Hospital in Hong Kong. Images were acquired using a 3 Tesla MRI scanner (Achieva TX, Philips Medical System, Best, the Netherlands) with an eight-channel SENSE head coil. A 3D high resolution T1-weighted anatomical image was obtained for each participant with the following parameters: repetition time (TR)=7.4 ms, echo time (TE)=3.4 ms, flip angle=80, voxel size=1.04 x 1.04 x 0.6 mm<sup>3</sup>. Four runs of fMRI images during the working memory task were acquired with a T2-weighted gradient echo-planar imaging (EPI) sequence: TR=3000 ms, TE=35 ms, flip angle=90, field of view=230 x 230 mm<sup>2</sup>, matrix=96 x 96, 40 slices, voxel size=2.4 x 2.4 x 3 mm<sup>3</sup>. A total of 128 volumes were obtained for each of the four runs. Before the participants performing the working memory task, a 4- minute resting state fMRI images with eyes open were also collected (80 volumes). Image preprocessing was done by SPM8, a freeware available online ([www.fol.ion.ucl.ac.uk/spm](http://www.fol.ion.ucl.ac.uk/spm)). Image alignment was performed for head motion correction to enable subsequent voxel-wise data analysis and smoothing was done on the rsfMRI data to remove random noises due to its low signal-to-noise ratio. Some studies in the proposed project used specific cohorts of patients to investigate the brain functional changes, network or connectivity which the imaging protocol would be slightly different according to the requirement from the clinical perspective.

### 2.2 Detection of functional correlated regions

Detection of functional correlated regions was conducted from high dimensional rsfMRI dataset by incorporating the prior knowledge of the brain function of young children. Several detection models were proposed to identify the correlated regions. The seed ROI model and the commonly used independent component analysis (ICA) method were adopted.

### 2.3 Development of brain atlas based on Chinese pediatric

Brain atlas is useful for intra- and interpopulation comparison. A new MRI brain atlas was developed using intensity and sulci landmark combined group-wise registration method to align the population of images. The images were preprocessed using N4ITK bias field correction and the non-local mean filtering. After preprocessing, group-wise registration was used to bring the group of images into the common space followed by calculating the group mean image to serve as the atlas image. Non-linear registration was performed using the symmetric image normalization (SyN) algorithm in ANTS software (<http://www.picsl.upenn.edu/ANTS/>). The local image average and variance were estimated by cross-correlation (CC) as intensity similarity metric. To match the cortical folding patterns, BrainVISA (<http://brainvisa.info/>) was adopted to combine both intensity and cortical folds matching which helped to extract the sulci automatically for each brain. The extracted sulcal labels were used as landmarks in registration to match different sulci in different brains. Landmarks were incorporated into SyN, and the intensity metric and landmarks metric were weighted evenly. Optimization was completed over three levels

of resolution with a maximum of fifty iterations at the first two coarse levels and ten iterations at the full resolution level. The atlas was computed based on Euclidean mean and the group-wise registration stopped until convergence, which the final group mean image would be served as the representative atlas of the population (1). As demonstrated in experiments, the newly constructed atlas could better represent the size and shape of brains of Chinese pediatric population, and show better performance in Chinese pediatric brain image analysis compared with other standard atlases.

## 2.4 Network templates construction

Default-mode network (DMN) is a prominent network among all large-scale brain networks which can be derived from the resting-state fMRI (rs-fMRI) data. Several studies demonstrated that DMN has been altered in patients with neuro-degenerative or neuro-disordered related diseases. A probabilistic DMN template from a group of fifty healthy subjects was generated based on independent component analysis (ICA). The image preprocessing was done on SPM8 ([www.fil.ion.ucl.ac.uk/spm](http://www.fil.ion.ucl.ac.uk/spm)). An anatomical brain template was created initially using the transformed T1W images by averaging and spatially blurring with a 6-mm Gaussian full-width half-maximum filter. Then the initial DMN template was obtained by group-level ICA analysis using the FSL Melodic software (<http://www.fmrib.ox.ac.uk/fsl/index.html>). Then the similarity measurement was conducted between DMN components. Similarity between the independent components and the template was defined as the absolute value between their z maps derived from the melodic as follows:

$$s(z_i, z_t) = \left| \frac{1}{M} \sum_{m=1}^M \left[ \left( \frac{z_i(m) - \bar{z}_i}{\delta_{z_i}} \right) \left( \frac{z_t(m) - \bar{z}_t}{\delta_{z_t}} \right) \right] \right|$$

where  $z_i$  and  $z_t$  are the z-values of M voxels in the common mask of the z-value maps of the  $i$ th component and the initial template,  $\bar{z}_i$  and  $\bar{z}_t$  are the mean values of the  $z_i$  and  $z_t$ , respectively, and  $\delta_{z_i}$  and  $\delta_{z_t}$  are the corresponding standard deviations. The final template was completed after a series of iterative procedure and stopped until the similarity measurement was more than 95% between the current and the previous generated template. The proposed probabilistic DMN template and the proposed similarity matching mechanism were demonstrated to be effective in automatic selection of independent components from the ICA analysis results (2).

## 2.5 Improvement on imaging quality and processing

MRI data obtained from subjects could be affected by many kinds of artifacts due to motions, breathing, field gradient etc. Image noise was one of the most common types of problem that researchers work on MRI had to be dealt with. In this project, several techniques were developed to improve the image quality included de-noising algorithm, data normalization technique and parallel computing to accelerate the processing speed. Two de-noising methods were proposed which one of them was based on nonlocal feature-preserving method. As image noise were mostly modeled by Rician distribution, a nonlocal total variation (NLTV)-based feature-preserving MRI Rician denoising model was developed to take full advantage of high degree of self-similarity and redundancy within MR images. A two-step optimization approach was used to solve the resulting convex denoising model and the proposed method was tested using sets of synthetic and clinical MRI data together with one diffusion tensor MRI (DTI) data set. Extensive experiments are conducted to compare the proposed method with several other commonly used de-noising methods (3). Another de-noising method was developed based on a two-step wavelet-domain estimation followed by Bayesian modeling approach. To further improve the de-noising performance, the spatially adaptive regularization parameters were calculated by a local variance estimator. It took full advantage of the global MR image prior and local image features (4). Besides de-noising, a parallel accelerating technique and a data normalization technique were proposed to enhance image processing speed and to improve the data compatibility respectively (5,6).

## *2.6 Understand the function and structure of the brain*

Besides the technical works such as template development and image quality improvement, the functional activity, connectivity, topological organization and structural network of the brain were also investigated in the project (7-10). These studies were conducted more from the clinical perspective to measure the change of brain in patients with different diseases. Obtained results provided a more comprehensive understanding of the human brain for us to design the navigation system.

## *2.7 Development of navigation system*

With the proposed brain atlas and templated developed from the previous steps, components were integrated to build an efficient navigation system. The surgical navigation system was developed to assist surgeons to enhance accuracy and precision during medical intervention such as tumor biopsy and resection. The proposed surgical navigation system was implemented by using open-source, cross-platform toolkit, including Visualization Toolkit (VTK), Insight Segmentation and Registration Toolkit (ITK), Fast Light Toolkit (FLTK) and Image-Guided Surgery Toolkit (IGSTK) and tested on a notebook (Windows 8, 2.5GHz Intel(R) Core(TM) i7-4710, 8Gb Memory). DICOM images were first input into the system. Marching cube algorithm was utilized to segment the skin followed by marking several landmark points in the images by practitioner. After configuration of navigation tracker, those points were registered one-by-one with the real position on the patient. Landmark-based registration was computed and measured registration error in root mean square. The navigation system could be implemented and played an assisting role in surgical planning and helped surgeons during operations.

## **3. RESULTS ACHIEVED**

Fourteen peer-reviewed journal and 2 conference articles were published. New techniques to enhance MR image quality and processing efficiency were carried out along with several others studies regarding the altered brain function or structure in patients with different diseases. A brain atlas based on Chinese pediatric population and a DMN template were created and implemented into the navigation system. Representative brain atlas and template help to accurately register neuro images for surgical planning before surgery.

A high quality representative brain atlas based on Chinese pediatric population using Intensity and sulci landmark was developed. It was important in medical image analysis and could be useful for image guide surgeries. The proposed brain atlas in this project better represented the size and shape of brains in Chinese pediatric population (1). We also constructed a probabilistic atlas of default mode network (DMN) from resting-state fMRI (2). This DMN atlas helped to determine whether patients had abnormal DMN by comparing with the healthy subjects. Also, a brain template based on Chinese children and adolescent was developed [C1].

Magnetic resonance imaging (MRI) was an outstanding medical imaging modality. Improving the signal to noise ratio was a great challenge due to images suffer from noise pollution during image acquisition and transmission. A new technique was proposed to enhance image quality using feature-preserving de-noising method. Most existing MRI de-noising methods did not simultaneously take the global image prior and local image features into account. The de-noising method in this publication was developed based on an assumption of spatially varying Rician noise map and utilized the global MR image prior and local image features. Numerous experiments were conducted on synthetic and real MR data sets to compare the efficacy of the model with other well popular de-noising methods (3). Another approach of image de-noising was based on global hyper-Laplacian prior and Rician noise assumption using Bayesian modeling approach. It was a generalized total variation-based MRI de-noising model. The proposed model had the properties of backward diffusion in local normal directions and forward diffusion in local tangent directions. To further improve the de-noising performance, a local variance estimator-based method was introduced to calculate the spatially adaptive regularization parameters related to local image features and spatially varying noise map

(4). The experimental results demonstrated the superior performance of the proposed model in terms of quantitative and qualitative image quality evaluations.

Image registration played an important role in brain morphometric analysis. Existing registration algorithms such as FSL's FLIRT (FMRIB's linear image registration tool) and ANTs (Advanced Normalization Tools) were commonly used by domain experts. In this project, a side work on image processing acceleration was done based on GPU implementation of FLIRT with the correlation ratio (CR) as the similarity metric and a GPU accelerated correlation coefficient (CC) calculation for the symmetric diffeomorphic registration of ANTs. Results demonstrated that the proposed algorithm outperformed the original algorithm in terms of computational efficiency. This technique helped to accelerate the process of image registration in the navigation system (5). Another important step of MR image preprocessing on brain analysis was to normalize the intensity of obtained data. A histogram-based MRI intensity normalization method was developed to normalize scanning data acquired from different MRI machines. This technique helped to improve the performance on image analysis to create high quality brain template and analysis data acquired from different scanners (6). DTI scanning was one of the most reliable scanning to reveal the white matter fiber tracks and spinal cord. Results from previous studies demonstrated that some diseases such as adolescent idiopathic scoliosis (AIS) affected the spinal cord, and the connectivity and morphology of the brain included cerebellum. To further study the physiology, morphology, and connectivity of the fiber track in human brain and spinal cord, a new technique to improve the performance of DTI segmentation was developed. To overcome the disadvantages of requiring adequate prior knowledge and tuning parameters in other techniques, our new method automatically learnt an adaptive distance metric by a graph based semi-supervised learning model (11).

Besides all technical works, new experiments were carried out to understand the performance of brain in terms of connectivity, network, fibers integrity, functional and morphological changes in patients with different diseases including AIS, MCI, developmental dyslexia, obstructive sleep apnea and schizotypal personality disorder. Previous studies demonstrated that the tonsil level in patients with AIS was lower than that in normal and the somatosensory evoked potentials (SSEP) was disturbed above vertebral C5-6 level. Our recent publication verified the decreased fractional anisotropy (FA) values and increased MD values at the medulla oblongata and C1-2, C2-3, C3-4, and C4-5 segments in patients with AIS (12). The occurrence of cerebral hyperperfusion syndrome (CHS) was studied using pre- and post-operative change in cerebral blood flow (CBF) on patients with Moyamoya disease after surgery [C2]. Brain activity in MCI was investigated to enhance our knowledge in patients with neuro-degenerative diseases. Experimental results indicated the impaired encoding and recognition functions in aMCI and implied the specific role of visual area in aMCI during the visuospatial working memory task. The impaired working memory function in aMCI was demonstrated and the study results provided a new perspective to study the compensatory mechanism in aMCI (7). Besides, the topological organization of the brain structural network in Chinese dyslexic (8) and the morphometric correlation network in patients with childhood obstructive sleep apnea (OSA) were studied (9). Results revealed an altered topological organization of brain structural network in Chinese dyslexic and the altered topological property of gray matter volume structural network was presented in OSA.

The brain templates, atlas, and techniques for image improvement have been implemented into the neurosurgical assistant system proposed in this project. The navigation system is based on C++ computing language and it has been tested on phantom models. The system has been demonstrated to surgeons in both internal and public conferences. Video tutorial is available for medical personnel to learn and be familiar with the system.

#### **4. PUBLICATION AND AWARDS**

Peer-reviewed journal articles:(1-14)

1. Luo Y, Shi L, Weng J, He H, Chu WC, Chen F, Wang D. Intensity and sulci landmark combined brain atlas construction for Chinese pediatric population. *Human brain mapping* 2014;35(8):3880-3892.

2. Wang D, Kong Y, Chu WC, Tam CW, Lam LC, Wang Y, Northoff G, Mok VC, Shi L. Generation of the probabilistic template of default mode network derived from resting-state fMRI. *IEEE transactions on bio-medical engineering* 2014;61(10):2550-2555.
3. Liu RW, Shi L, Yu SC, Wang D. A two-step optimization approach for nonlocal total variation-based Rician noise reduction in magnetic resonance images. *Medical physics* 2015;42(9):5167-5187.
4. Liu RW, Shi L, Huang W, Xu J, Yu SC, Wang D. Generalized total variation-based MRI Rician denoising model with spatially adaptive regularization parameters. *Magnetic resonance imaging* 2014;32(6):702-720.
5. Luo YG, Liu P, Shi L, Luo Y, Yi L, Li A, Qin J, Heng PA, Wang D. Accelerating Neuroimage Registration through Parallel Computation of Similarity Metric. *PloS one* 2015;10(9):e0136718.
6. Sun X, Shi L, Luo Y, Yang W, Li H, Liang P, Li K, Mok VC, Chu WC, Wang D. Histogram-based normalization technique on human brain magnetic resonance images from different acquisitions. *Biomedical engineering online* 2015;14:73.
7. Lou W, Shi L, Wang D, Tam CW, Chu WC, Mok VC, Cheng ST, Lam LC. Decreased activity with increased background network efficiency in amnesic MCI during a visuospatial working memory task. *Human brain mapping* 2015;36(9):3387-3403.
8. Liu K, Shi L, Chen F, Waye MM, Lim CK, Cheng PW, Luk SS, Mok VC, Chu WC, Wang D. Altered topological organization of brain structural network in Chinese children with developmental dyslexia. *Neuroscience letters* 2015;589:169-175.
9. Luo YG, Wang D, Liu K, Weng J, Guan Y, Chan KC, Chu WC, Shi L. Brain Structure Network Analysis in Patients with Obstructive Sleep Apnea. *PloS one* 2015;10(9):e0139055.
10. Zhang Q, Shen J, Wu J, Yu X, Lou W, Fan H, Shi L, Wang D. Altered default mode network functional connectivity in schizotypal personality disorder. *Schizophrenia research* 2014;160(1-3):51-56.
11. Kong Y, Wang D, Shi L, Hui SC, Chu WC. Adaptive distance metric learning for diffusion tensor image segmentation. *PloS one* 2014;9(3):e92069.
12. Kong Y, Shi L, Hui SC, Wang D, Deng M, Chu WC, Cheng JC. Variation in anisotropy and diffusivity along the medulla oblongata and the whole spinal cord in adolescent idiopathic scoliosis: a pilot study using diffusion tensor imaging. *AJNR American journal of neuroradiology* 2014;35(8):1621-1627.
13. Luo YG, Ko JK, Shi L, Guan Y, Li L, Qin J, Heng PA, Chu WC, Wang D. Myocardial Iron Loading Assessment by Automatic Left Ventricle Segmentation with Morphological Operations and Geodesic Active Contour on T2\* images. *Scientific reports* 2015;5:12438.
14. Wang D, Zhu F, Fung KM, Zhu W, Luo Y, Chu WC, Mok VC, Wu J, Shi L, Ahuja AT, Mao Y. Predicting Cerebral Hyperperfusion Syndrome Following Superficial Temporal Artery to *Middle Cerebral Artery Bypass based on Intraoperative Perfusion-Weighted Magnetic Resonance Imaging*. *Scientific reports* 2015;5:14140.

*Conference articles:*

[C1] Wong Kok Cheung, Luo Yishan, Shi Lin, Chen Feiyan and Wang Defeng, "Template Building For Chinese Children And Adolescent And Comparison With Western Standard Template", *The Conjoint Congress of 18th Convention of Academia Eurasiana Neurochirurgica (AEN) 11th Asia Pacific Multidisciplinary Meeting for Nervous System Diseases (Brain Symposium)*, Hong Kong, Mar 5-8, 2014

[C2] Defeng Wang, Ka Ming Fung, Lin Shi, Fengping Zhu, Ying Mao. *Evaluation of Surgical Outcome of Moyamoya Disease Patients after Revascularization using Atlas-based Magnetic Resonance Brain Perfusion Analysis*. *European Congress of Radiology*. Mar. 6-10, 2014. Vienna Austria. DOI: 10.1594/ecr2014/C-0192

# BIOMIMETIC SCAFFOLD FOR STEM CELL BASED CARTILAGE REGENERATION AND DRUG DELIVERY

---

---

Principal Investigator: Professor BIAN Liming <sup>(1)</sup>  
*Department of Mechanical & Automation Engineering, CUHK*

Co-Investigator:

Prof. Arthur MAK <sup>(2)</sup>

Research Team Members:

Dr. WEI Kongchang, Dr. LI Jinming <sup>(1)</sup>

<sup>(1)</sup> Dept. of Mechanical & Automation Engineering, CUHK

<sup>(2)</sup> Dept. of Biomedical Engineering, CUHK

Project Start Date: 1 July 2013

Completion Date: 30 June 2015



## ABSTRACT

Osteoarthritis (OA) is symptomized as progressive degeneration of articular cartilage in human diarthrodial joints. A recent study in Hong Kong found that about 10% of the Hong Kong population aged 50 years and older can be diagnosed with knee osteoarthritis [1]. This showed that osteoarthritis is one of the major causes of disability among the Hong Kong population just as in the rest of the world. Current treatments including arthroplasty and mosaicplasty have various major limitations such as limited life span, lack of donor tissue, etc.

hMSCs (human mesenchymal stem cells) have gained increasing popularity as a cell source for cartilage repair, due to their multipotency and easy availability. However, after firstly differentiating (chondrogenesis) into chondrocytes (cartilage cells) like cells, hMSCs continue to differentiate toward a hypertrophic phenotype, resulting in extensive mineralization of the neocartilage formed, which should be free of mineralization. This problem, which motivates this proposed work, is now being recognized as a major obstacle to the widespread adoption of hMSCs as a clinically viable cell source for cartilage repair.

Glycosaminoglycan (GAG) is a key component of the cartilage extracellular matrix (ECM). Sulfated glycosaminoglycans have been shown to maintain the activity of growth factors. Sulfated glycosaminoglycans also attract cations including calcium ions with their negative charges, thereby changing the calcium concentration in the intercellular tissue environment and potentially influencing tissue mineralization. The project proposes to chemically incorporate the sulfate groups into biomaterial scaffold to emulate the biochemical properties of the native cartilage cellular microenvironment. This will allow us to investigate the role of sulfation in regulating hMSC chondrogenesis and subsequent hypertrophic tissue mineralization.

The results of the project will not only help the development of new stem cell therapies for cartilage repair, but will also guide the design of novel scaffold materials for repairing defects in interfacial regions including ligament/tendon to bone insertions and cartilage to bone interfaces.

## 1. OBJECTIVES AND SIGNIFICANCE

**Objective 1:** synthesize crosslinkable sulfated glycosaminoglycan biopolymers for the fabrication of hydrogel scaffold.

**Objective 2:** investigate the effect of sulfated hydrogel scaffolds made of sulfated glycosaminoglycan on the retention of chondrogenic growth factors.

**Objective 3:** examine the effect of sulfated hydrogel scaffolds made of sulfated glycosaminoglycan on chondrogenic differentiation of hMSCs.

**Objective 4:** examine the effect of sulfated hydrogel scaffolds made of sulfated glycosaminoglycan on hypertrophic differentiation of hMSCs and resulting matrix mineralization.

### **Impact and novelty**

The findings from this study will shed light on the influence of scaffold sulfation on drug delivery from biomaterial scaffold. Furthermore, it will also provide guidance on the design of biomaterial scaffold to better control hMSC differentiation and cartilage mineralization. Moreover, mineralization is found in many other connective tissues including bone, menisci and intervertebral discs either as a required developmental process or as a pathological condition. Therefore, the findings from this study will not only enhance hMSC-based cartilage repair but will also be instrumental in developing stem cell based therapies to regenerate or repair other musculoskeletal tissues including bone, menisci and intervertebral discs.

The novelty of this work lies in three aspects. Firstly, the retention and stability of chondrogenic growth factors in sulfated hydrogels has not been thoroughly investigated before; secondly, few previous studies have examined the effects of sulfation of hyaluronic acid on chondrogenesis. Lastly, no prior studies have studied the effect of hydrogel sulfation on hMSC hypertrophy and matrix mineralization following chondrogenesis.

## **2. RESEARCH METHODOLOGY**

### **Objective 1**

#### *Methacrylation of hyaluronic acid (HA)*

Methacrylated hyaluronic acid (molecular weight 70kD) (MeHA) will be synthesized as previously reported [1-4] (**Figure 1**). Briefly, methacrylic anhydride (methacrylic anhydride, Sigma) is added to a solution of 1 wt% HA or CS in deionized water, adjusted to a pH of 8 with NaOH, and left to react on ice for 24 hours. The macromer solution will be purified via dialysis (MW cutoff 6–8kD) against deionized water for a minimum of 48 hours with repeated changes of water. The final product will be obtained by lyophilization and stored at -20 °C prior to use. The degree of methacrylation of final macromer products will be evaluated by <sup>1</sup>H NMR.

#### *Preparation of MeHA Sulfates (S-MeHA)*

Since chondroitin sulfate is a sulfated glycosaminoglycan, no additional sulfation of CS is needed. The sulfation of MeHA (HA is a nonsulfated glycosaminoglycan) will be carried out based on an adapted protocol describe previously. Briefly, MeHA will be dissolved in deionized water to produce 1% w/v solution. The solution will be stirred with 3 gram of Dowex-100 ion exchanger added for each gram of MeHA (tetrabutylammonium-form) for 8 hours. After filtration, the polymer solution will be lyophilized and dissolved in DMF at 1% w/v under N<sub>2</sub>. Sulfur trioxide/dimethylformamide complex (SO<sub>3</sub>-DMF) dissolved in DMF will be added to the TBA-MeHA solution in DMF (molar polymer/SO<sub>3</sub> ratio 1:20) under N<sub>2</sub> at room temperature. The reaction solution will stirred for 60 min. The sulfated products will be purified by precipitation into acetone and neutralized using ethanolic NaOH solution. The formed S-MeHA will be washed several times with acetone and purified by dialysis against distilled water, followed by lyophilization. The degree of sulfation of the S-MeHA will be determined using an automatic elemental analyzer.

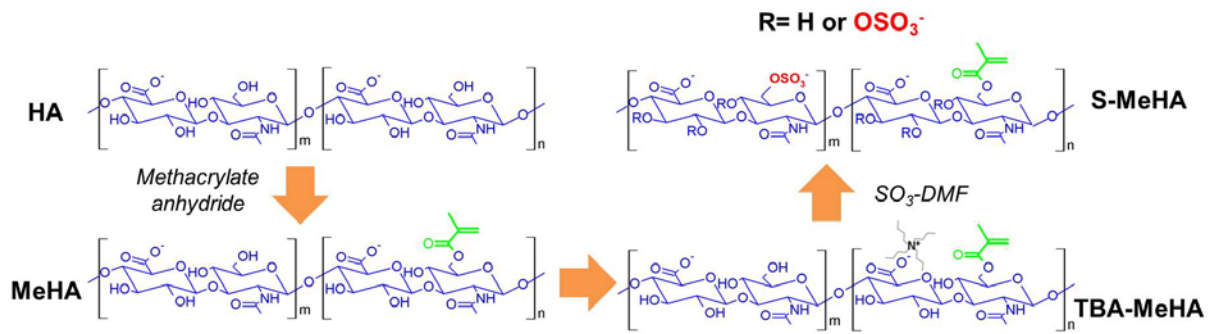
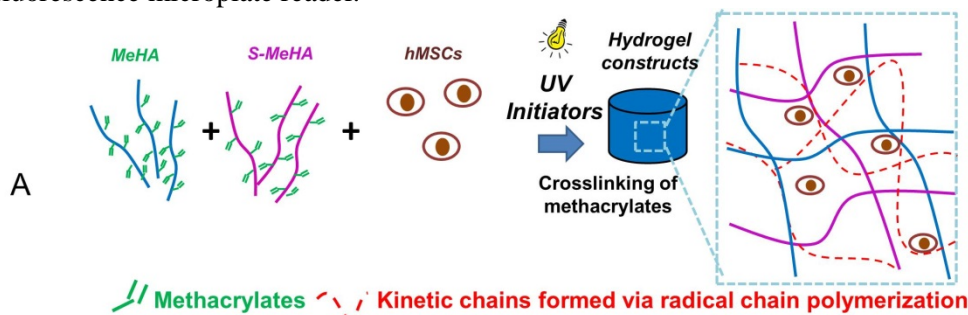


Figure 1. Synthesis of MeHA and S-MeHA

## Objective 2

### Quantification of the release of encapsulated molecules form hydrogels

Acellular hydrogels will be fabricated by photopolymerization of precursor solutions comprised of MeHA, S-MeHA dissolved in phosphate buffered saline (PBS) containing 0.05 wt% of the photoinitiator I2959 (2-methyl-1-[4-(hydroxyethoxy) phenyl]-2-methyl-1-propanone, Ciba) to allow for UV-mediated polymerization (**Figure 2 A without cells**). The precursor solutions will be exposed to ultra-violet light (UV time: 12 minutes, wavelength: 360nm; intensity: 1.2mW/cm<sup>2</sup>) for gelation. Gelation will be assessed by monitoring the storage (G') and loss (G'') modulus using a rheometer in a cone and plate geometry. Standard protein molecules used in release studies including bovine serum albumin (BSA, FITC tagged) will be mixed with the precursor solutions and subsequently encapsulated in the hydrogel upon gelation. The hydrogels samples will be incubated in PBS at 37 ° C. The release of the fluorescently tagged BSA will be quantified by a fluorescence microplate reader.



Preliminary formulations of ECM hydrogels	Concentration of ECM molecules (% w/v)		
	MeHA (%)	S-MeHA (%)	Total ECM conc. (% w/v)
1	2	0	2
2	1	1	2
3	0.5	1.5	2
4	0	2	2

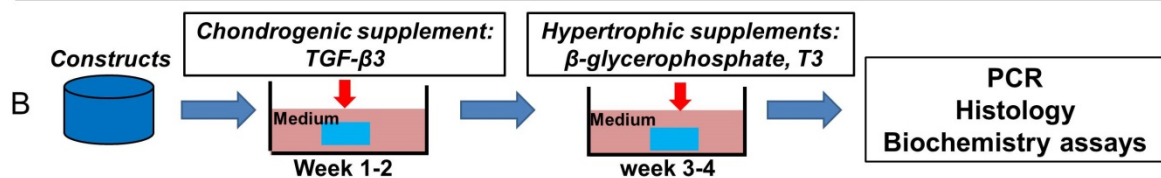


Figure 2. (A) Fabrication of sulfated ECM hydrogels via photocrosslinking. (B) *in vitro* culture of hMSC-seeded hydrogels for chondrogenic and hypertrophic differentiation.

## Objective 3 & 4

### hMSC encapsulation in hydrogels and chondrogenic and hypertrophic induction

Human MSCs (Lonza) will be expanded to passage 3 in a growth media consisting of  $\alpha$ -MEM with 16.7% RESEARCH REPORT IN BME

FBS (fetal bovine serum). MSCs (20 million/ml) will be encapsulated in hydrogel disk constructs as described above ( $\varnothing$ 5mm, 2.6 mm thickness) (**Figure 2 A**). Formed constructs will be cultured in chondrogenic media (DMEM, 1% ITS+Premix, 50  $\mu$ g/ml L-proline, 0.1  $\mu$ M dexamethasone, 50 $\mu$ g/ml ascorbate, antibiotics) supplemented with transforming growth factor (TGF- $\beta$ 3, 10ng/ml)(**Figure 2 B**)[5]. To evaluate hypertrophy and resulting mineralization by hMSC, a previously established *in vitro* culture model will be employed. Briefly, constructs will be first cultured in chondrogenic media for 2 weeks. Media will be then switched to hypertrophic induction media (1nM dexamethasone, 1nM triiodothyronine/T3 and 10mM  $\beta$ -glycerophosphate/ $\beta$ -gly) from week 3 through week 4 (**Figure 2 B**)[6].

#### *Gene expression analysis*

Gene expression of chondrogenic (type II collagen, Aggrecan, Sox9) and hypertrophic markers (type X collagen, MMP13, ALP/alkaline phosphatase) at selected time points will be analyzed by real time PCR. Sequences of the primers and probes are listed in a previous publication [7]. The relative gene expression will be calculated using the  $\Delta\Delta C_T$  method, where the fold difference will be calculated using the expression  $2^{\Delta\Delta C_T}$ . Each sample will be internally normalized to GAPDH and the expression levels of MSCs at the time of encapsulation.

#### *Biochemical analysis*

The PicoGreen assay (Invitrogen) will be used to quantify the DNA content of the constructs. The GAG content will be measured using the dimethylmethylene blue (DMMB) dye-binding assay. The overall collagen content will be assessed by measuring the orthohydroxyproline content via the dimethylaminobenzaldehyde and chloramine T assay. Calcium content will be quantified using a commercial kit (BioVision).

#### *Histological analysis*

Constructs will be fixed in 4% formalin, embedded in paraffin, and processed using standard histological procedures. Immunohistochemical staining will be performed on histological sections (8  $\mu$ m thick) for targets of interest using the Vectastain ABC kit and the DAB Substrate kit for peroxidase (Vector Labs).

#### *Statistical and power analysis*

Statistica (Statsoft) will be used to perform statistical analyses using two-way ANOVA, followed by Tukey's HSD post hoc testing to allow for comparison between groups. Statistical significance will be set at  $p < 0.05$ . A statistical power analysis indicates that  $n=8$  samples per group should be sufficient for obtaining a study power of 0.85 with significance set at  $p < 0.05$ .

### **3. RESULTS ACHIEVED**

Please state the project achievement in this part and (if any) please state the patent application and/or product commercialisation plan.

**Objective 1, 2, 3, and 4 are all achieved. Detailed data are presented below.**

Native hyaluronic acid was first grafted with varying level of sulfate groups. A quantitative element analysis demonstrates the absence of sulfur in the native unmodified HA, and the sulfur content is 1.61% (w/w) and 2.86% (w/w) for the low sulfated hyaluronic acid (LS-HA) and high sulfated hyaluronic acid (HS-HA) macromeres, respectively (Figure 1a). The methacrylated hyaluronic acid (MeHA) was also sulfated in order to incorporate the sulfated HA into the HA hydrogels. The methacrylate modification degree of the (MeHA is estimated to be 17% based on the  $^1H$  NMR spectra (Figure 2c). The prepared MeHA was then modified with low (LS-MeHA) and high (HS-MeHA) level of sulfate groups, respectively. The  $^1H$  NMR spectra of both low and high-sulfated MeHA exhibit a shift of the proton peaks of HA backbone hydroxyls because of the sulfate substitutions, thereby confirming the successful sulfation of HA (Figure 2c-e). The methacrylated degree of LS-MeHA and HS-MeHA remains the same as that of the nonsulfated MeHA, indicating that sulfation has no negative effect on the grafted methacrylate groups. LS-MeHA and HS-MeHA

also has the similar sulfur content as that of LS-HA and HS-HA. To visualize the incorporation of sulfate groups into the HA-based hydrogels, the MeHA hydrogels (3% MeHA), LS-MeHA hydrogels (2.5% MeHA and 0.5% LS-MeHA), and HS-MeHA hydrogels (2.5% MeHA and 0.5% HS-MeHA) were incubated with dimethylmethylene blue (DMMB) solution for one day. Both the LS-MeHA and HS-MeHA hydrogels exhibit purple color compared to the blue MeHA hydrogels (Figure 1b), demonstrating the presence of sulfate groups in the LS-MeHA and HS-MeHA hydrogels.

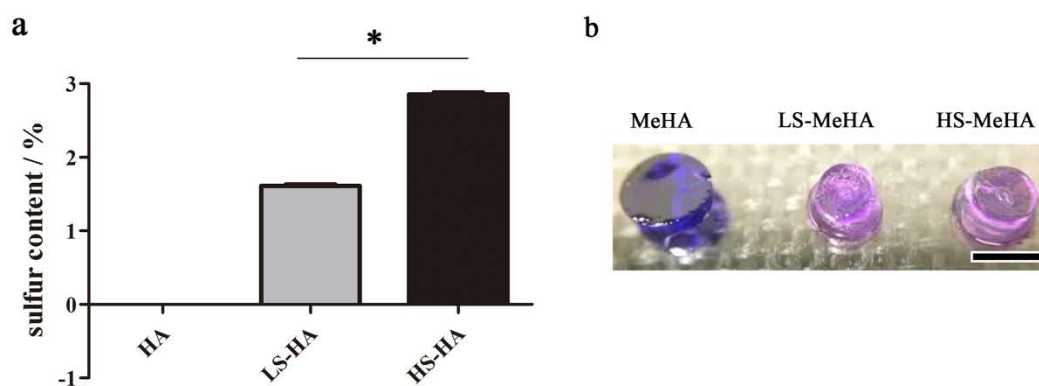


**Figure 1.** Sulfation degree of HA. (a) Sulfur content of HA, LS-HA, and HS-HA determined by elemental analyzer. (b) DMMB staining of the MeHA, LS-MeHA, and HS-MeHA hydrogels. Scale bar: 5 mm (b). \* $p < 0.001$ .

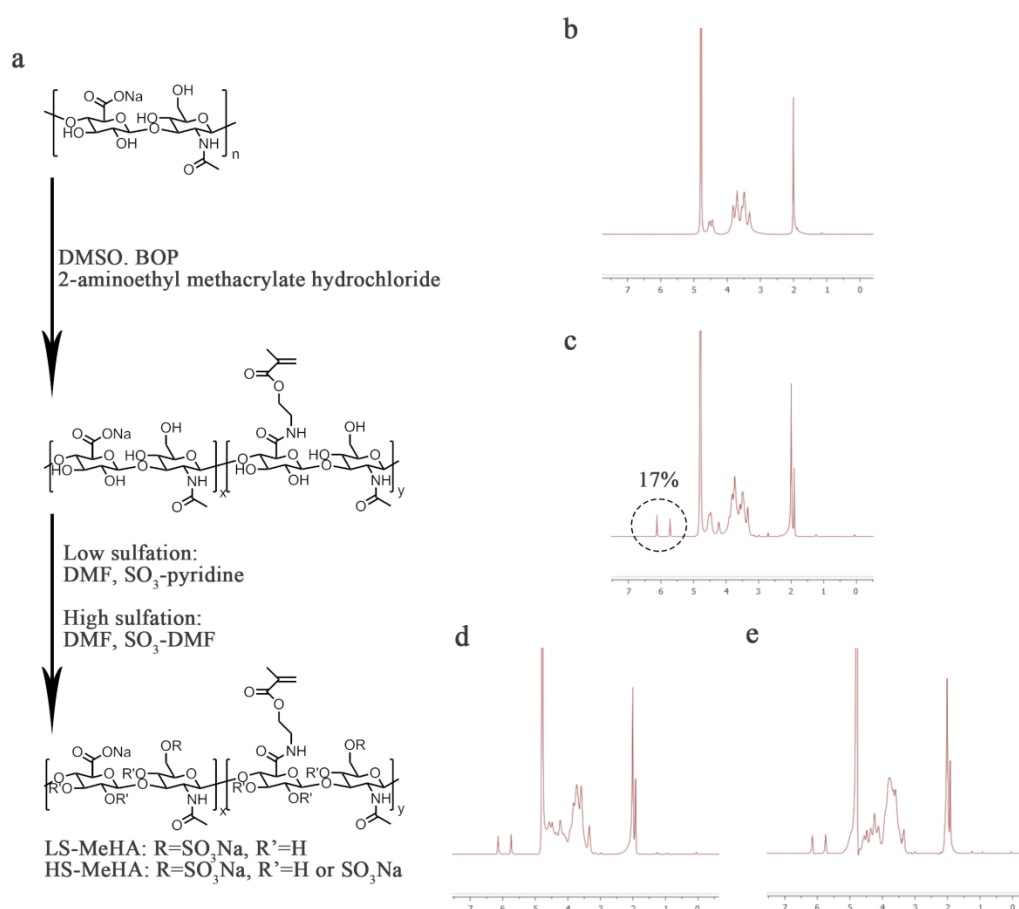


**Figure 2.** Synthesis route of the sulfated MeHA. (a) Native HA was converted to MeHA first and then reacted with  $\text{SO}_3$ -pyridine or  $\text{SO}_3$ -DMF to obtain LS-MeHA or HS-MeHA, respectively.  $^1\text{H}$  NMR spectra of (b) HA, (c) MeHA, (d) LS-MeHA, and (e) HS-MeHA.

To study the effect of sulfation on the degradation rate of HA, 1.5 mL 5 % (w/v) PBS solution of HA, LS-HA, and HS-HA were mixed with 0.03 mg hyaluronidases, and then the mixture was incubated at 37 °C for 28 days. The molecular weight (Mw) of HA before degradation and of HA, LS-HA, and HS-HA after the enzymatic digestion was determined by GPC. Figure 3a illustrates that after the digestion HS-HA has the shortest elution time comparable to that of the undigested HA, whereas the unmodified HA has the longest elution time after the digestion. This indicates that among these three groups, a higher sulfation degree of HA has the highest Mw after 28 days of enzymatic digestion. This result suggests that the higher sulfation degree leads to a lower degradation rate of HA in the presence of hyaluronidase. We postulate that the sulfate groups on the LS-HA and HS-HA backbone reduce the available unmodified HA octasaccharide substrate required for the effective hyaluronidase action. We believe that the incorporation of the sulfated MeHA macromers to hydrogels delays the degradation of the HA hydrogels *in vitro* and *in vivo*, allowing hydrogels to protect and facilitate the growth and differentiation of the encapsulated hMSCs for a longer time.

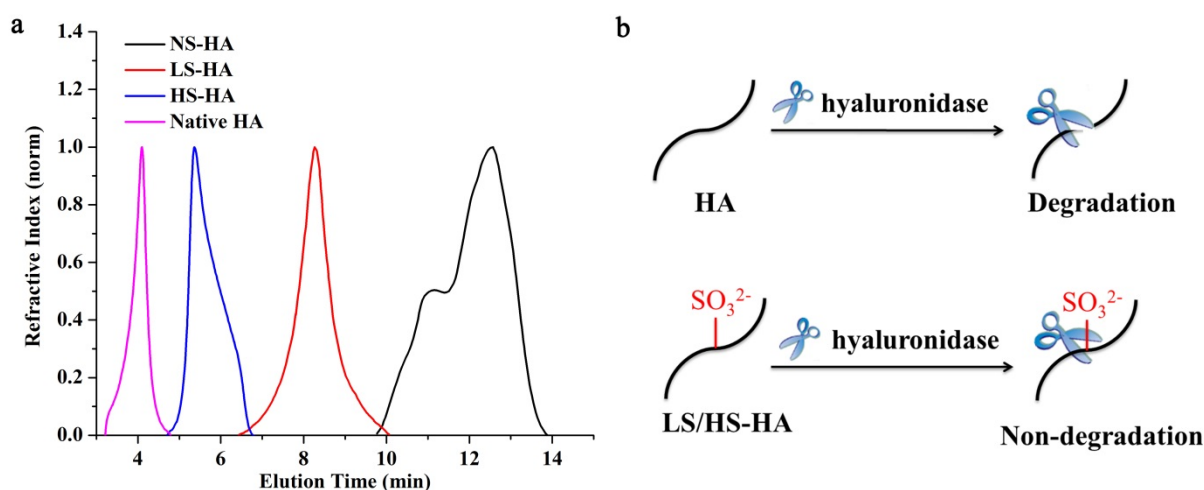


**Figure 3.** Degradation properties of HA and sulfated HA. (a) GPC results for native HA before enzymatic digestion, and native HA, LS-HA, and HS-HA after hyaluronidase digestion. (b) Schematic illustration of the effect of sulfation on the degradation of HA.

In addition to the degradation rate of the hydrogels, the retention of inductive growth factors in the hydrogels is also vital to the growth and differentiation of the encapsulated hMSCs.[8, 9] For stem cell-based cartilage regeneration, it is desirable to retain the transforming growth factor- $\beta$ 1 (TGF- $\beta$ 1), which promotes the chondrogenesis and suppresses the hypertrophy of hMSCs, in the hMSCs-laden hydrogels for an extended period.[10, 11] However, native HA, the only nonsulfated GAG, has negligible protein binding capability.[12, 13] Studies have revealed that in the sulfated GAGs, such as heparin, sequester and stabilize the proteinaceous cytokines in the ECM through electrostatic interactions between the negatively charged sulfate groups on GAGs and the positively charged amino acid residues of cytokines.[14, 15] Another study has shown that the sulfated HA hydrogels can efficiently bind stromal cell-derived factor-1 (SDF-1), a proteinous growth factor. Therefore, we speculate that addition of sulfated groups into HA-based hydrogels can aid the sequestration of TGF (Figure 4a), and the release rates of TGF in the LS-MeHA and HS-MeHA hydrogels are 40% and 50% lower than that of the nonsulfated MeHA hydrogels, respectively. We believe that the improved binding efficiency of TGF in the sulfated HA hydrogels is likely due to the electrostatic interaction between the negatively charged sulfate groups and the positively charged amino acid residues of TGF (figure 4b).

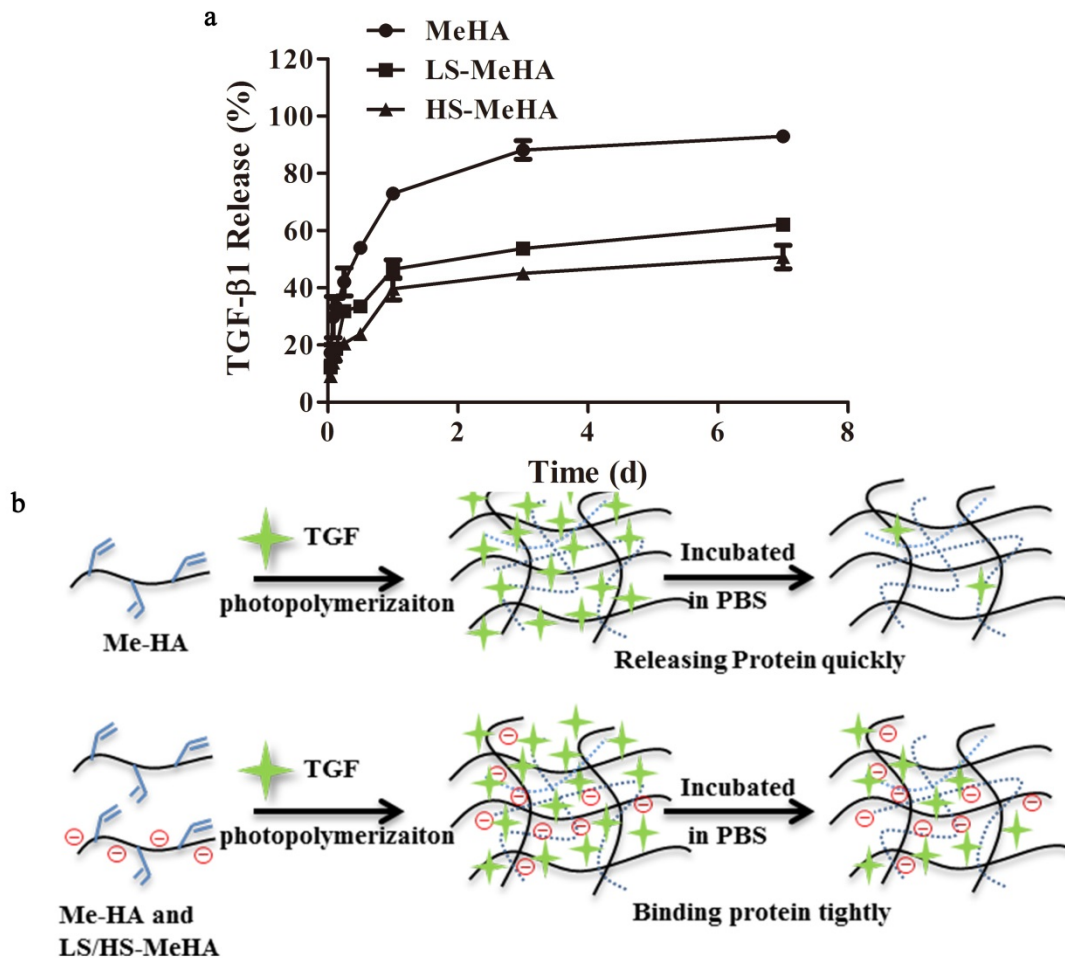


**Figure 4.** TGF release from the HA hydrogels. (a) Kinetics of TGF release from the MeHA, LS-HA, and HS-HA hydrogels. (b) Schematics of the TGF release from the nonsulfated and sulfated HA hydrogels.

We further investigate whether the improved growth factor-binding due to the sulfate groups is favorable to the chondrogenic differentiation of hMSCs encapsulated in the HA-based hydrogels. As shown in the previous studies, chondrogenically induced hMSCs tend to further differentiate toward a hypertrophic phenotype, leading to the extensive calcification of the neocartilage, which is the major hurdle for the use of MSCs in cartilage regeneration [16, 17]. In this study, an *in vitro* hypertrophy model (hMSCs-laden hydrogels were cultured in chondrogenic medium for 14 days and subsequently cultured in hypertrophic medium for 14 days) was used to evaluate the hMSCs hypertrophy after chondrogenic induction. Live/dead staining indicates that the majority (> 95 %) of the encapsulated hMSCs are alive in both the non-sulfated and sulfated MeHA hydrogels after 28 days of culture (Figure 5a), and this indicates that the sulfation does not affect the viability of hMSCs. The real-time PCR results show that under the chondrogenic culture condition, the mRNA expression of chondrogenic markers (type II collagen and aggrecan) in the LS-MeHA and HS-MeHA hydrogels, particularly the HS-MeHA group, is considerably higher than the expression in the MeHA hydrogels (Figure 5b). Under the hypertrophic culture condition, the hMSCs in the LS-MeHA and HS-MeHA hydrogels still maintain a higher expression of Aggrecan and a lower expression of type X collagen, MMP-13, and ALP compared to the hMSCs in the non-sulfated MeHA hydrogels (Figure 5b). Consistent with the gene expression data, the content of GAGs, a crucial cartilaginous matrix component, is the sulfated HA hydrogels (LS-MeHA, HS-MeHA) compared with the non-sulfated MeHA hydrogels under both the chondrogenic and hypertrophic culture (Figure 5c). Furthermore, the sulfated HA hydrogels (LS-MeHA, HS-MeHA) contain

significantly lower content of calcium, a crucial marker for cartilage hypertrophy, compared with the MeHA hydrogels under the hypertrophic culture (Figure 5c). The Alcian blue (against GAGs)-Picrosirius red (against collagens) staining and the immunohistochemistry staining (against type II collagen and chondroitin sulfate) demonstrate more uniform deposition of cartilage matrix in the LS-MeHA and HS-MeHA groups than that in the MeHA groups (Figure 6). The Von Kossa-Fast Red staining indicates negligible calcification in all groups after chondrogenic culture. However, after hypertrophic culture, calcification increases greatly in the MeHA group but not in the LS-MeHA and HS-MeHA groups (Figure 6).

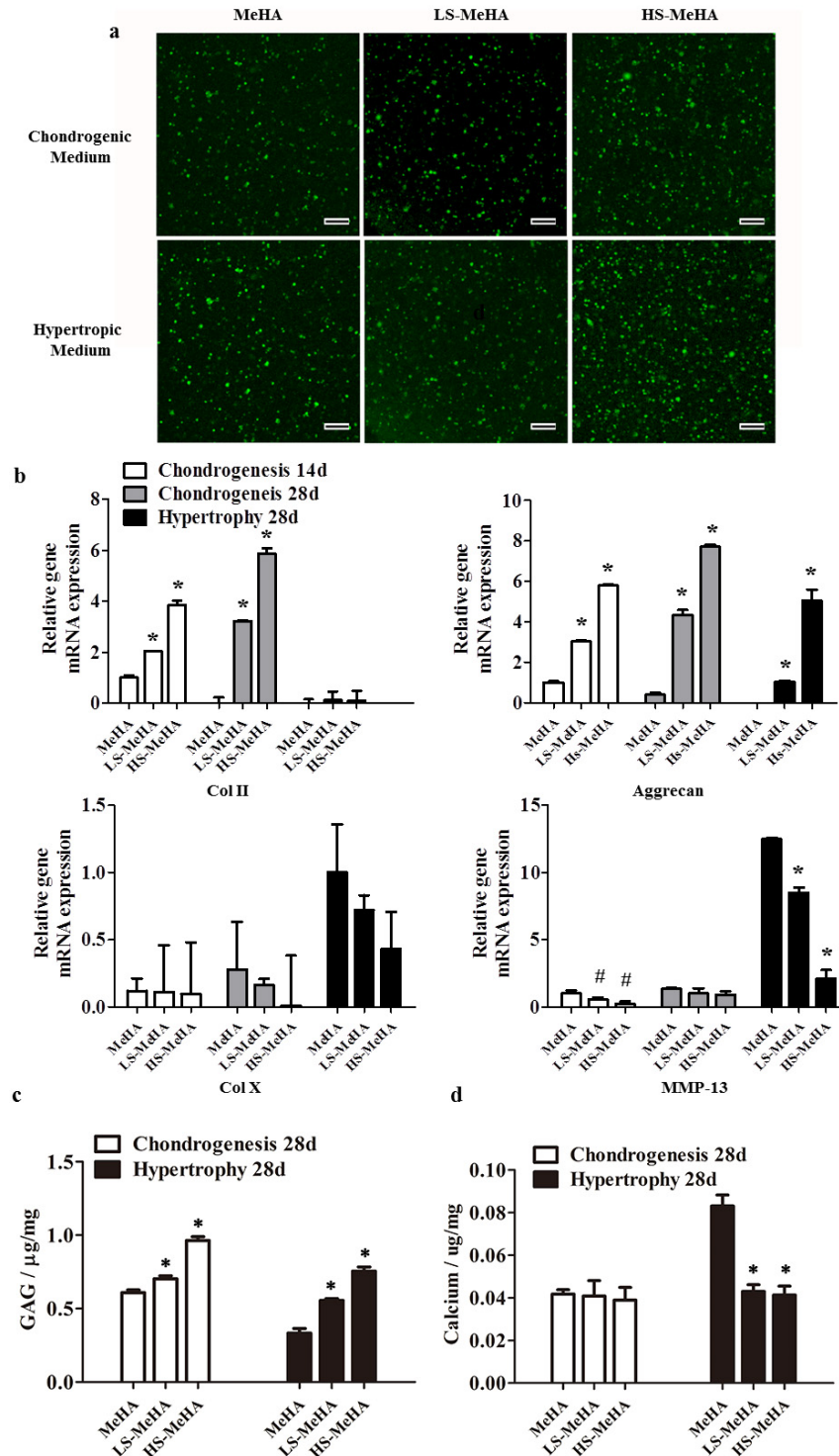


**Figure 5.** The chondrogenesis and hypertrophy of hMSC encapsulated in the HA hydrogel *in vitro*. (a) Cell viability staining of the hMSCs-laden MeHA, LS-MeHA, and HS-MeHA hydrogels after 28 days of culture. (b) Gene expression (normalized to GAPDH) of the selected chondrogenic markers (type II collagen (Col II) and aggrecan) and hypertrophic markers (type X collagen (Col X), MMP-13). (c) GAG content (normalized to the weight of samples) and (d) Calcium content (normalized to the wet weight of samples) of the hMSC-laden hydrogels after 28 days of culture. Scale bar: 100  $\mu\text{m}$  (a) 0.01 vs. MeHA.

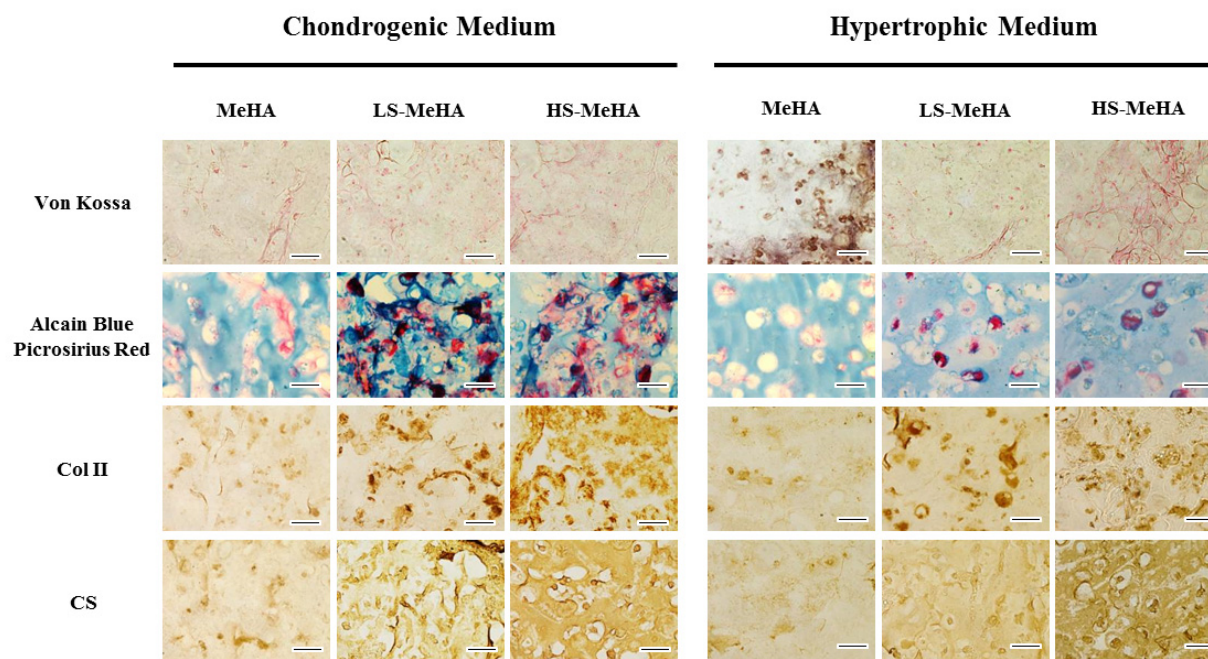


**Figure 6.** Von Kossa staining, alcain blue-picrosirius red staining, and immunohistochemical staining for type II collagen (Col II) and chondroitin sulfate (CS) of hMSCs-laden MeHA, LS-MeHA, and HS-MeHA hydrogel constructs after 28 days of *in vitro* culture. Scale bar: 50  $\mu\text{m}$ .

To further investigate the effect of sulfation on hMSCs hypertrophy after chondrogenic induction *in vivo*, we inserted hMSCs-laden MeHA, LS-MeHA, and HS-MeHA hydrogels into the subcutaneous pockets of nude mice after 14 days of chondrogenic culture *in vitro*. The images of the harvested hydrogels after 28 days of implantation demonstrate that all hydrogels remain largely intact (Figure 7). As expected, the Von Kossa-Fast Red staining shows more calcification in the MeHA hydrogels than in the sulfated MeHA hydrogels, and the Alcain blue-Picrosirius red staining as well as the type II collagen and CS immunohistochemical staining reveal more cartilage matrix deposition in the sulfated MeHA hydrogels than that in the MeHA hydrogels.

These data show that the sulfation of HA hydrogels not only promotes the chondrogenesis of hMSCs but also suppresses hypertrophic differentiation of the chondrogenically induced hMSCs *in vitro* and *in vivo*. We hypothesized that the sulfated HA hydrogels better retain TGF- $\beta$ 1 by the binding of the negative sulfate groups. In addition, the negatively charged sulfate groups in the sulfated HA hydrogels may repel negatively charged phosphate donors, which are required for calcification, thus leading to the reduced hypertrophic calcification.

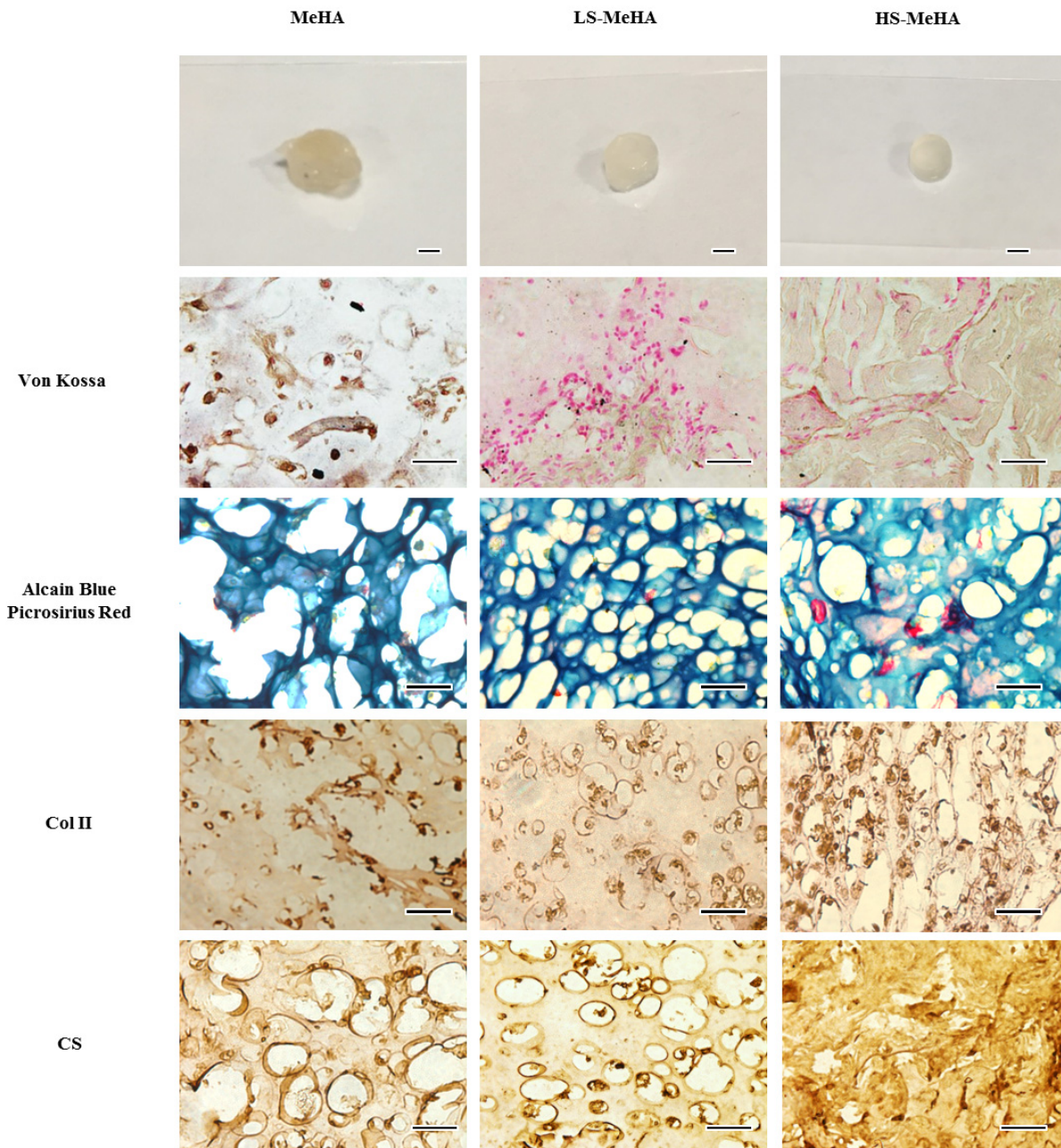


**Figure 7.** Stereoscopic pictures, Von Kossa staining, alcain blue-picrosirius red staining, and immunohistochemical staining of the harvested hydrogels after 14 days of chondrogenic culture *in vitro* followed by 28 days of subcutaneous implantation in nude mice. Scale bar: 50  $\mu$ m, except 2mm for hydrogel images.

#### 4. PUBLICATION AND AWARDS

##### *Journal papers*

1. +Feng, Q.; +Zhu, M.; Wei, K.; \*Bian, L. Cell-mediated degradation regulates human mesenchymal stem Cell chondrogenesis and hypertrophy in MMP-sensitive hyaluronic acid hydrogels. PLoS ONE, 2014 Jun 9;9(6) (+ Equal contribution)

2. +Zhu, M.; +Feng, Q.; \*Bian, L. Differential effect of hypoxia on human mesenchymal stem cell chondrogenesis and hypertrophy in hyaluronic acid hydrogels. *Acta Biomaterialia* (+ Equal contribution) 2014 Mar;10(3):1333-40.PMID: 24342044
3. Choi, C.K.; Xu, Y.; Wang, B.; Zhu, M.; Zhang, L.; \*Bian, L. Substrate coupling strength of integrin-binding ligands modulates adhesion, spreading, and differentiation of Human mesenchymal stem cells. *Nano Letters*, 2015 Oct 14;15(10):6592-600.
4. Feng, Q.; Lin, S.; Dong, C.; Huang, H.; Wu, T.; Yan, X.; Zhang, L.; Li, G.; Bian, L. Effect of hyaluronic acid sulfation on enzymatic degradation, growth factor retention, and hMSC chondrogenesis and hypertrophy. In preparation

### ***Patent***

US provisional patent: A bioadhesive and injectable hydrogel. Inventors: Feng, Q.; Wei, K.; Lin, S.; Li, G.; Bian, L. US non-provisional patent is being filed.

### ***Awards***

5<sup>th</sup> Asian Biomaterial Congress Young Investigator Award.

### **References:**

- [1] Smeds KA, Pfister-Serres A, Miki D, Dastgheib K, Inoue M, Hatchell DL, et al. Photocrosslinkable polysaccharides for in situ hydrogel formation. *J Biomed Mater Res*. 2001;54:115-21.
- [2] Bryant SJ, Arthur JA, Anseth KS. Incorporation of tissue-specific molecules alters chondrocyte metabolism and gene expression in photocrosslinked hydrogels. *Acta Biomater*. 2005;1:243-52.
- [3] Guo Y, Yuan T, Xiao Z, Tang P, Xiao Y, Fan Y, et al. Hydrogels of collagen/chondroitin sulfate/hyaluronan interpenetrating polymer network for cartilage tissue engineering. *J Mater Sci Mater Med*. 2012;23:2267-79.
- [4] Li Q, Williams CG, Sun DD, Wang J, Leong K, Elisseeff JH. Photocrosslinkable polysaccharides based on chondroitin sulfate. *J Biomed Mater Res A*. 2004;68:28-33.
- [5] Byers BA, Mauck RL, Chiang IE, Tuan RS. Transient exposure to transforming growth factor beta 3 under serum-free conditions enhances the biomechanical and biochemical maturation of tissue-engineered cartilage. *Tissue Eng Part A*. 2008;14:1821-34.
- [6] Mueller MB, Tuan RS. Functional characterization of hypertrophy in chondrogenesis of human mesenchymal stem cells. *Arthritis Rheum*. 2008;58:1377-88.
- [7] Bian L, Hou C, Tous E, R. R, Mauck RL, Burdick JA. The Influence of Hyaluronic Acid Hydrogel Crosslinking Density and Macromolecular Diffusivity on Human MSC Chondrogenesis and Hypertrophy. *Biomaterials*. 2012;in press.
- [8] Akar B, Jiang B, Somo SI, Appel AA, Larson JC, Tichauer KM, et al. Biomaterials with persistent growth factor gradients in vivo accelerate vascularized tissue formation. *Biomaterials*. 2015;72:61-73.
- [9] Albro MB, Nims RJ, Durney KM, Cigan AD, Shim JJ, Vunjak-Novakovic G, et al. Heterogeneous engineered cartilage growth results from gradients of media-supplemented active TGF-beta and is ameliorated by the alternative supplementation of latent TGF-beta. *Biomaterials*. 2015;77:173-85.
- [10] Wu C, Jiao H, Lai Y, Zheng W, Chen K, Qu H, et al. Kindlin-2 controls TGF-beta signalling and Sox9 expression to regulate chondrogenesis. *Nature communications*. 2015;6:7531.
- [11] Yamashita A, Morioka M, Yahara Y, Okada M, Kobayashi T, Kuriyama S, et al. Generation of scaffoldless hyaline cartilaginous tissue from human iPSCs. *Stem cell reports*. 2015;4:404-18.

- [12] Robinson DE, Buttle DJ, Short RD, McArthur SL, Steele DA, Whittle JD. Glycosaminoglycan (GAG) binding surfaces for characterizing GAG-protein interactions. *Biomaterials*. 2012;33:1007-16.
- [13] Xu X, Jha AK, Duncan RL, Jia X. Heparin-decorated, hyaluronic acid-based hydrogel particles for the controlled release of bone morphogenetic protein 2. *Acta biomaterialia*. 2011;7:3050-9.
- [14] Du F, Wang H, Zhao W, Li D, Kong D, Yang J, et al. Gradient nanofibrous chitosan/poly varepsilon-caprolactone scaffolds as extracellular microenvironments for vascular tissue engineering. *Biomaterials*. 2012;33:762-70.
- [15] Lee SS, Huang BJ, Kaltz SR, Sur S, Newcomb CJ, Stock SR, et al. Bone regeneration with low dose BMP-2 amplified by biomimetic supramolecular nanofibers within collagen scaffolds. *Biomaterials*. 2013;34:452-9.
- [16] Feng Q, Zhu M, Wei K, Bian L. Cell-mediated degradation regulates human mesenchymal stem cell chondrogenesis and hypertrophy in MMP-sensitive hyaluronic acid hydrogels. *PloS one*. 2014;9:e99587.
- [17] Zhu M, Feng Q, Bian L. Differential effect of hypoxia on human mesenchymal stem cell chondrogenesis and hypertrophy in hyaluronic acid hydrogels. *Acta biomaterialia*. 2014;10:1333-40.

## *Multimedia Technologies Track*

# Research Reports In Multimedia Technologies

### **Newly Funded Project**

(2017 - 2017)

\* Achieving Simultaneous Spectral-Spatial Super-Resolution via Reconstruction from Multispectral and Hyperspectral Images

### **Completed Project**

(2014 - 2016)

\* Managing and Analyzing Big Graph Data

---

The following reports are enclosed in “Research Highlights” printed in June 2015

### **Completed Project**

(2012)

\* Face Recognition Across Ages Through Binary Tree Learning

---

The following reports are enclosed in “Research Highlights” printed in June 2014

### **Completed Projects**

(2011)

\* Semantic Analysis for Image Resizing

\* Time Critical Applications over a Shared Network

\* Amplify-and-forward Schemes for Wireless Communications

---

The following reports are enclosed in “Research Highlights” printed in 2013

**Completed Projects**

- |        |   |
|--------|---|
| (2010) | * FADE: Secure Cloud Storage with File Assured Deletion                                   |
|        | * Security and Detection Protocols for P2P-Live Streaming Systems                         |
| (2009) | * An Opportunistic Approach to Capacity Enhancement in Wireless Multimedia Networks       |
|        | * Computer-Aided Second Language Learning through Speech-based Human-Computer Interaction |
- 

The following reports are enclosed in “General Report and Research Highlights 2009-2011” printed in October 2011.

**Completed Projects**

- |        |  |
|--------|--|
| (2008) | * Pattern Computation for Compression and Performance Garment                              |
| (2007) | * Real-time Transmission of High Definition (HD) 3D Video and HD Audio in Gigabit-LAN      |
|        | * High Dynamic Range Image Compression and Display   |
|        | * Multimedia Content Distribution over Hybrid Satellite-Terrestrial Communication Networks |
| (2006) | * Automatic Video Segmentation and Tracking for Real Time Multimedia Services              |
|        | * Information Retrieval from Mixed-Language Spoken Documents                               |
|        | * Wireless Networks and Its Potential for Multimedia Applications                          |
- 

The following reports are enclosed in “Research Highlights 2005-2007” printed in January 2008.

**Completed Projects**

- |        |  |
|--------|--|
| (2005) | * Mobile Wireless Multimedia Communication   |
|        | * An Automatic Multi-layer Video Content Classification Framework  |
|        | * Automatic Multimedia Fission, Categorization and Fusion for Personalized Visualization in Multimedia Information Retrieval |

*(Funded Year)*

## MANAGING AND ANALYZING BIG GRAPH DATA

---

---

Principal Investigator: Professor Ken MA  
*Department of Electronic Engineering, CUHK*

**Project Start Date: 1 July 2017**



### ABSTRACT

Hyperspectral super-resolution (HSR), a recently emerged image processing technique that aims to reconstruct a spectral-spatial super-resolution image from images with either lower spectral resolution or lower spatial resolution, is expected to become a key technology soon. HSR can significantly enhance applications in areas such as computer vision, art conservation, food safety, geoscience and remote sensing, offering an imaging solution that can identify objects that are hard to see by human eyes and with fine resolutions. It holds great potential and we expect the topic will see substantial growth. The goal of this project is to investigate key fundamental problems that arise in this timely topic. Specifically, the PI will study perfect reconstruction conditions of HSR—which is an open theoretical question that none of the existing literature has been able to answer. Addressing this question satisfactorily will lead to guidelines on how to build provably correct HSR solutions, rather than relying on empirical experience which is currently the case. Furthermore, the PI will study a unified optimization framework for HSR, which is important in establishing a computationally efficient algorithmic toolset in this context.

### INNOVATION AND PRACTICAL SIGNIFICANCE:

This project aims to develop a theoretical framework for hyperspectral resolution, addressing why recovery of a hyperspectral super-resolution image from low resolution images can be possible in theory and further understanding how we can build better systems. While current developments in this context have shown successful results by empirical means, they are practice or intuition-driven and are unable to answer the question of why hyperspectral super-resolution works from a fundamental research viewpoint. The innovative part of this project is that the PI will depart from the standard path of the current research trends (which are somehow bottom-up) and endeavor to tackle much more challenging theoretical problems arising from this relatively new research topic (which is top-down with an emphasis on asking why, and not just how). The impacts are expected to be significant as it will lead to theoretical guidelines on designing provably good hyperspectral super-resolution algorithms and cameras, which is presently unavailable in the literature.

Moreover, the PI should emphasize that hyperspectral super-resolution is currently a rapidly emerging topic with great potential and many possibilities in applications such as computer vision, medical imaging, art conservation, to name a few. The PI sees that now is the great opportunity to investigate this timely topic, seeing the substantial impacts a theoretical framework can reshape the topic and the far-reaching implications in many applications.

## **PROJECT OBJECTIVES:**

1. to analyze conditions under which perfect recovery of a super-resolution image is guaranteed, and to identify good low-rank models and provably correct formulations under such analyses
2. to establish a unified optimization framework for low-rank matrix factorization in HSR

The first objective of this project is particularly innovative. All the current developments in HSR demonstrate feasibility via empirical experiences, and the designs are intuition-driven. A theoretical framework that pins down whether and how super-resolution is possible is still missing—and the PI intends to challenge that piece of uncharted water. The outcomes, if satisfactory, will provide theory-guided designs for HSR, which has much significance from a fundamental research viewpoint and will reshape how practical researchers think when designing an HSR algorithm. The second objective is important in bringing new and computationally efficient tools for practical implementations.



# MANAGING AND ANALYZING BIG GRAPH DATA

---

---

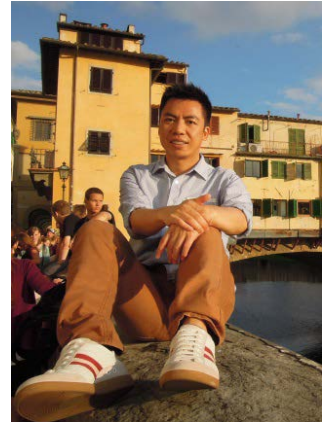
Principal Investigator: Professor James CHENG  
*Department of Computer Science and Engineering, CUHK*

Research Team Members:

- Shang Fanhua, Postdoctoral Fellow <sup>(1)</sup>
- Lu Yi, M.Phil. Student <sup>(1)</sup>
- Huang Yuzhen, Research Assistant (August 2014 to May 2015),  
Ph.D. Student (starting from August 2015) <sup>(1)</sup>

<sup>(1)</sup> Dept. of Computer Science and Engineering, CUHK

**Project Start Date: 1 July 2014**  
**Completion Date: 31 June 2016**



## ABSTRACT

This project aims to develop effective and scalable techniques for managing and analyzing big graph data, and to apply them for searching and analyzing multimedia data, especially data from online social networks (e.g., Facebook, Twitter, Google+, LinkedIn) and online shopping platforms (e.g., eBay, Amazon, Taobao). Graph is widely used to model online social network structures, as well as many complicated data types such as images and pictures, videos, and other interactivity contents, etc. We propose to study fundamental issues of big graph data research, including the study of elementary substructures and important properties of massive graphs, the modeling of these graphs for prediction and extrapolation studies, and the applications of big graph data in areas that may create impacts in both industry and academia. The key to big graph data management and analysis is to develop a robust distributed system that provides a general programming framework for implementing all kinds of distributed graph algorithms. Such a system is very useful to many companies for analyzing their data; in particular, we will work with our industrial collaborators such as Taobao to explore the application of our research to manage and analyze massive data collected from their online shopping platform.

## 1. OBJECTIVES AND SIGNIFICANCE

**Objective:** The project aims to develop an efficient and scalable system for managing and analyzing big graph data, in particular, massive network data from online social networks and online shopping platforms.

**Significance:**

1. Impact on academia: The proposed research is a timely study on one of the most important topics in the areas of database and data mining research. The success of this project can significantly advance research in the field of graph data management and graph mining. Techniques developed in this research will also benefit cross-disciplinary research including sociology, physics, biology, ecology, economics, finance, etc., because of the prevalence of graph and network data in their respective domains.
2. Impact on industry: The results obtained in this project will provide deeper insights about the patterns of real-world networks and the behaviors of their users including the communications and relationships among them. Such knowledge can be used by industry such as online social networking companies (e.g., Facebook, Twitter) and telecom operators (e.g., China Mobile, CSL) to better understand user behaviors and their interaction patterns, online auction and shopping platforms (e.g.,

eBay, Amazon, Taobao) to analyze shopping trends, airlines and other transportation companies for better logistic and itinerary planning.

## 2. RESEARCH METHODOLOGY

The first step is to collect massive graphs from various domains including social networks, phone communication networks, web graphs, RDF graphs, and so on. We also use graphs to model multimedia data such as pictures and videos. The graphs in our current collection have up to billions of vertices and edges, which are the largest ones that are publicly available. Some of these graphs are associated with rich attribute information as well as temporal information, which pose significant new challenges as standard techniques cannot be applied.

The proposed research consists of the following four main aspects.

**Study of graph structures.** Graph structures can reveal many important properties of a graph. However, most graph structures are expensive to compute. For today's big graphs, it is infeasible to even load a graph based on a single-machine setting. Thus, distributed computing becomes necessary. One key challenge of applying distributed computing to solving graph problems is that distributed graph algorithms are often very complicated to design and implement, not to mention complicated issues in a distributed environment such as fault tolerance.

To address the above-mentioned issues, we first propose to develop a general-purpose distributed graph-computing system that provides a user-friendly programming framework for implementing distributed graph algorithms. The system is built on a share-nothing distributed cluster consisting of ordinary PCs or workstations. We adopt Pregel's vertex-centric programming model and users design their algorithms by "thinking like a vertex", while the system automatically handles all complicated issues of distributed computing such as job distribution and scheduling and fault tolerance.

With the general-purpose distributed graph-computing system, we can then develop efficient and scalable distributed algorithms for computing different types of graph structures. We categorize graph structures into two levels: the micro level and the macro level. At the micro level, small elementary substructures of a graph, such as paths, cycles, triangles, cliques, etc., will be studied. At the macro level, larger components of a graph, such as k-cores, k-trusses, dense subgraphs, clusters, etc., will be studied.

We will develop algorithms for storing, maintaining, searching, querying, and analyzing various types of micro-level and macro-level structures in massive graphs. In particular, we define a class of algorithms, to be developed based on our general-purpose distributed graph-computing system, with the following properties:

Let  $n$  be the total number of vertices in the input graph,  $d(v)$  be the number of neighbors of a vertex  $v$  in the graph, and  $p$  be the number of computing nodes available.

1. *Linear space usage:* each vertex  $v$  uses  $O(d(v))$  space of storage and each computing node keeps  $(n/p)$  vertices.
2. *Linear computation cost:* the amount of work done for processing each vertex  $v$  is  $O(d(v))$ .
3. *Linear communication cost:* the algorithm processes in rounds and at each round, the size of the messages sent/received by each vertex  $v$  is  $O(d(v))$ .
4. *At most logarithmic number of rounds:* the algorithm terminates after  $O(\log n)$  rounds.

Properties 1-3 offer good load balancing and linear cost at each round of the parallel computation, while Property 4 controls the total running time. We have identified a long list of fundamental graph problems including breadth-first search, spanning tree, Euler tour, pre/post-order traversals, connected components, bi-connected components, strongly connected components, single-source shortest paths, PageRank, etc., for

which there exists a parallel algorithm that satisfies the above defined four properties.

In addition, we will investigate the semantics of various graph structures both individually and collectively, and hence their functions on the evolution of a graph (e.g., a social network) and their correlation with various graph properties. In particular, we are interested in studying the temporal properties of paths in time-varying graphs, for which we define four types of paths, collectively we call them minimum temporal paths, as they give the minimum value for different measures:

1. *Earliest-arrival path*: a path that gives earliest arrival time starting from a source  $s$  to a target  $t$ .
2. *Latest-departure path*: a path that gives latest departure time starting from  $s$  in order to reach  $t$  by a given time.
3. *Fastest path*: the fastest path to go from  $s$  to  $t$ .
4. *Shortest path*: the shortest path from  $s$  to  $t$ .

Both efficient distributed algorithms and scalable indexes will be developed to compute these paths and answer temporal distance queries in real time.

**Study of graph properties.** We propose to conduct a comprehensive study on the correlation between a series of well-known graph properties such as density, size, diameter, centrality, connectivity, sustainability, etc., as well as to explore new graph properties that may give new insights into the understanding of graphs. We will develop efficient and scalable methods to compute and analyze these properties for big graphs, to categorize them, and to identify their strengths and limitations in various contexts.

**Study of graph models.** Based on the graph structures and properties, we propose to further explore more accurate models for real-world graphs. Existing models often capture only the more general patterns of a class of graphs while neglecting specific patterns in these graphs. We will study a wide spectrum of real-world graphs, analyze the properties and patterns possessed by these graphs, and propose more specific and accurate graph models. Efficient graph generators will also be developed to generate big graph data for running simulation and extrapolation studies, and for evaluating the performance and scalability of new graph algorithms.

**Applications of graphs to multimedia data analysis.** We propose to apply the results of our studies to graph structures, graph properties, and graph models to managing and analyzing massive multimedia data on the Web, especially in various online social networks (e.g., Facebook, Twitter, Google+, LinkedIn) and online auction and shopping platforms (e.g., eBay, Amazon, Taobao).

### 3. RESULTS ACHIEVED

The key to this project is the development of a distributed graph-computing system. A new general-purpose, distributed graph-computing system, called Pregel+, has been developed to process different types of graphs and implement different graph algorithms. The results of the research have been accepted and published in Proceedings of the 24th International World Wide Web Conference (WWW 2015), which is the best conference in the area of Web data management.

Pregel+ extends Pregel by supporting two effective message reduction techniques: (1) vertex mirroring and (2) a request-respond paradigm. These techniques not only reduce the total number of messages exchanged through the network, but also bound the number of messages sent/received by any vertex, especially for processing power-law graphs and (relatively) dense graphs. Compared with existing Pregel-like systems, Pregel+ provides simpler programming interface and yet achieves higher computational efficiency.

In another parallel work, we conducted an extensive performance study to evaluate the performance of Pregel+ comparing with the state-of-the-art graph-computing systems. Our results show that Pregel+ is significantly more efficient and more scalable than the most popular system, Apache Giraph, CMU's

GraphLab (which includes PowerGraph), and Stanford’s GPS, with respect to various graph characteristics, algorithm categories, and various optimization techniques. The results of the research have been accepted and published in PVLDB 2015, which is the best conference in the area of database systems. The details of the Pregel+ system are documented in Pregel+’s webpage: <http://www.cse.cuhk.edu.hk/pregelplus/>.

In a subsequent work, we also developed another general-purpose distributed graph-computing system, Blogel, which was published in PVLDB 2014. Blogel supports a block-centric programming model, which naturally addresses three adverse graph characteristics that lead to performance bottlenecks in existing graph computing systems such as Pregel: (1) skewed degree distribution, (2) (relatively) high density, and (3) large diameter. Blogel can be even from a few times to an order of magnitude faster than Pregel+. The details of the Blogel system are documented in Blogel’s webpage: <http://www.cse.cuhk.edu.hk/blogel/>.

We have also studied the application of Pregel+ to develop graph algorithms in a systematic way. We first identified a set of desirable properties of an efficient Pregel algorithm, such as *linear space*, *communication and computation cost per iteration*, and *logarithmic number of iterations*. We defined such an algorithm as a *practical Pregel algorithm (PPA)*. We then proposed PPAs for computing *connected components (CCs)*, *biconnected components (BCCs)*, and *strongly connected components (SCCs)*. The PPAs for computing BCCs and SCCs use the PPAs of many fundamental graph problems as building blocks, which are of interest by themselves.

In addition, we also applied the principle of PPA to develop Pregel algorithms that satisfy strict performance guarantees. In particular, we developed a set of useful building blocks that are the PPAs of fundamental graph problems such as *breadth-first search*, *list ranking*, *spanning tree*, *Euler tour*, and *pre/post-order traversal*. As fundamental graph problems, their PPA solutions can also be applied to numerous other graph problems besides BCCs and SCCs considered in our work. Extensive experiments over large real graphs verified that our algorithms have good performance in shared-nothing parallel computing platforms. The results of the research have been accepted and published in PVLDB 2014, which is the best conference in the area of database systems.

We have also applied our systems to study temporal networks. We developed efficient distributed algorithms for core decomposition in a large temporal graph. Core decomposition has been applied widely in the visualization and analysis of massive networks. However, existing studies of core decomposition were only limited to non-temporal graphs, while many real-world graphs can be naturally modeled as temporal graphs (e.g., the interaction between users at different time in online social networks, the phone call or messaging records between friends over time, etc.). We formally defined the problem of core decomposition in a temporal graph, proposed efficient distributed algorithms to compute the cores in massive temporal graphs, and applied our technique for temporal graph analysis.

To support fast query processing in a large temporal graph, we also developed efficient and scalable indexes. We proposed a novel efficient labeling scheme, called TopChain, which employs the properties of a temporal graph for answering temporal reachability queries and time-based path queries. TopChain has a linear index construction time and linear index size, which makes the method scalable. TopChain significantly outperforms the state-of-the-art indexes and supports efficient dynamic update. As temporal graphs can be used to model many networks with time-ordered activities, TopChain is a useful tool for analyzing these graphs.

#### 4. PUBLICATION AND AWARDS

[1] Y. Liu, F. Shang, W. Fan, J. Cheng, and H. Cheng, “Generalized Higher-Order Orthogonal Iteration for Tensor Decomposition and Completion,” *Proceedings of the 27th Annual Conference on Neural Information Processing Systems*, Pages 1763-1771, 2014.

- [2] Y. Lu, J. Cheng, D. Yan, and H. Wu, "Large-Scale Distributed Graph Computing Systems: An Experimental Evaluation," *PVLDB*, Volume 8, Number 3, Pages 281-292, 2014.
- [3] F. Shang, Y. Liu, J. Cheng, and H. Cheng, "Recovering Low-Rank and Sparse Matrices via Robust Bilateral Factorization," *Proceedings of the 14th IEEE International Conference on Data Mining*, Pages 965-970, 2014.
- [4] F. Shang, Y. Liu, J. Cheng, and H. Cheng, "Robust Principal Component Analysis with Missing Data," *Proceedings of the 23rd ACM International Conference on Information and Knowledge Management*, Pages 1149-1158, 2014.
- [5] D. Yan, J. Cheng, Y. Lu, and W. Ng, "Blogel: A Block-Centric Framework for Distributed Computation on Real-World Graphs," *PVLDB*, Volume 7, Number 14, Pages 1981-1992, 2014.
- [6] D. Yan, J. Cheng, K. Xing, Y. Lu, W. Ng, and Y. Bu, "Pregel Algorithms for Graph Connectivity Problems with Performance Guarantees," *PVLDB*, Volume 7, Number 14, Pages 1821-1832, 2014.
- [7] D. Yan, J. Cheng, Y. Lu, and W. Ng, "Effective Techniques for Message Reduction and Load Balancing in Distributed Graph Computation," *Proceedings of the 24th International World Wide Web Conference*, Pages 1307-1317, 2015.
- [8] F. Shang, Y. Liu, H. Tong, J. Cheng, and H. Cheng, "Robust Bilinear Factorization with Missing and Grossly Corrupted Observations," *Information Sciences*, Volume 307, Pages 53-72, 2015.
- [9] H. Wu, J. Cheng, Y. Lu, Y. Ke, Y. Huang, D. Yan, and H. Wu, "Core Decomposition in Large Temporal Graphs," *Proceedings of the 2015 IEEE International Conference on Big Data*, Pages 649-658, 2015.
- [10] Y. Liu, F. Shang, W. Fan, J. Cheng, and H. Cheng, "Generalized Higher-Order Orthogonal Iteration for Tensor Learning and Decomposition," *IEEE Transactions on Neural Networks and Learning Systems*, Volume 27, Number 12, Pages 2551-2563, 2016.
- [11] F. Shang, Y. Liu, and J. Cheng, "Scalable Algorithms for Tractable Schatten Quasi-Norm Minimization," *Proceedings of the 30th AAAI Conference on Artificial Intelligence*, Pages 2016-2022, 2016.
- [12] H. Wu, Y. Huang, J. Cheng, J. Li, and Y. Ke, "Reachability and Time-Based Path Queries in Temporal Graphs," *Proceedings of the 32nd IEEE International Conference on Data Engineering*, Pages 145-156, 2016.



# Shun Hing Distinguished Lecture Series

To achieve the Institute's mission to promote appreciation of engineering in society through education programs, the Institute has organized a Shun Hing Distinguished Lecture Series. So far, **thirty-nine** distinguished lectures have been presented by renowned scholars. These lectures all were very well received and we will continue to line up and invite outstanding researchers to visit CUHK and to deliver distinguished lectures for the Institute. Here to show the five distinguished lectures between 2015 and June 2017.

# CNN as Guided Multi-layer RECOS Transform

by Professor C.-C. Jay Kuo

*University of Southern California  
USA*

Date: 16 June 2017 (Friday)

## Abstracts

There is a resurging interest in developing a neural-network-based solution to supervised machine learning in the last 5 years. In this talk, I will provide a theoretical foundation to the working principle of the convolutional neural network (CNN) from a signal processing viewpoint. To begin with, the RECOS transform is introduced as a basic building block for CNNs. The term "RECOs" is an acronym for "REctified-CORrelations on a Sphere". It consists of two main concepts: data clustering on a sphere and rectification. Then, a CNN is interpreted as a network that implements the guided multi-layer RECOS transform. Along this line, we first compare the traditional single-layer and modern multi-layer signal analysis approaches. Then, we discuss how guidance is provided by data labels through backpropagation in the training with an attempt to offer a smooth transition from weakly to heavily supervised learning. Several future research directions are pointed out at the end.



# Learning From Hidden Traits: Joint Factor Analysis and Latent Clustering

by **Professor Nikos Sidiropoulos**

*Dept. of Electrical & Computer Engineering  
& Digital Technology Center  
University of Minnesota  
USA*



Date: 17 March 2016 (Thursday)

## Abstracts

Many real-life datasets exhibit structure in the form of physically meaningful clusters - e.g., news documents can be categorized as sports, politics, entertainment, and so on. Taking these clusters into account together with low-rank structure may yield parsimonious matrix and tensor factorization models and more powerful data analytics. In this talk, we will explore joint low-rank factorization and latent-domain clustering; that is, in clustering the latent reduced-dimension representations of the observed entities. To exemplify this idea, we provide three formulations: joint nonnegative matrix/tensor factorization (NMF/NTF) and K-means clustering; joint volume-minimization matrix factorization and K-means clustering; and joint NMF and subspace clustering. A unified algorithmic framework is proposed, and detailed algorithms are fleshed out for the examples considered. Numerical results obtained from synthetic and real-world document and image datasets show that the proposed approach can significantly improve both factor analysis and clustering accuracy.



# A Deep Learning Approach to Speech Enhancement and Source Separation

by Professor Chin-Hui Lee

*School of Electrical and Computer Engineering  
Georgia Institute of Technology  
USA*

Date: 9 November 2015 (Monday)

## Abstracts

In contrast to conventional theory-based signal processing, we formulate a novel deep learning framework as finding a regression function between an observed signal and a corresponding set of desired targets. Monte Carlo and big data techniques are often required to generate a large collection of input and output pairs in order to learn the often-complicated structure of the mapping functions. In this talk, we present recent advances in our lab on speech enhancement and source separation. Other related issues in speech recognition, speech synthesis, voice conversion, voice activity detection, speech dereverberation and bandwidth expansion will also be highlighted. Leveraging upon the recently emerging big data paradigm, many classical signal processing problems can now be cast in machine learning frameworks with deep neural networks (DNNs) capable of joint training of both continuous speech parameters, such as ideal binary mask in enhancement, log power spectrum in separation, and categorical information, such as voicing, phonation position and phone identity in synthesis. We believe a combination of deep learning and big data offers vast opportunities for R&D professionals to explore many ideas that are not easily accomplished in the past and pioneer new grounds that are still wide open in the future.



# OnTEn – An Online Tutor for Engineering Students

---

by **Professor Sanjit K. Mitra**

*Research Professor of Electrical &  
Computer Engineering  
University of California, Santa Barbara  
USA*

Date: 28 August 2015 (Friday)



## Abstracts

OnTEn is a web-service platform being developed to contain student-friendly, easy-to-navigate review modules for undergraduate students in engineering. These modules aim to assist regular courses being offered by universities. One of the main goals of this website is to provide a set of review modules on topics that are taught in earlier courses. In this way, our plan is provide a very flexible learning platform that students can use before and after the actual lecture. Each module includes a short explanation of the topic along with worked-out examples, drill problems with answers, and provides feedback on student performance for a better understanding of the relevant topic. Furthermore, this web service strives to serve as a companion platform for students to review concepts on their own time outside class.

# Robotic Systems for Cell Surgery and Nanomanufacturing

by **Professor Yu SUN**

*Department of Mechanical and Industrial Engineering  
University of Toronto  
Canada*



Date: 24 July 2015 (Friday)

## Abstracts

Rapid advances in biology and nanotechnology require the development of technologies for automated manipulation of cells and nanomaterials. Tasks such as single-cell surgery and the manoeuvring of individual nanowires pose interesting research challenges in micro-nanorobotic manipulation. For instance, relevant forces of object interactions (e.g., van der Waals force; electrostatic force) occurring in micro-nanomanipulation must be carefully characterized. Three-dimensional position information must be accurately obtained from two-dimensional image feedback of optical and electron microscopy. New visual servo control approaches are required to tackle nonlinearity and imprecisely modeled kinematics of micro-nanomanipulators.

In this talk, I will first introduce our robotic cell manipulation technologies. Hardware platforms and techniques such as cell immobilization, vision-based contact detection, and visual servo control will be discussed. System performance and applications to molecule testing and clinical cell surgery will be presented. I will then move from microrobotic manipulation to nanomanipulation under scanning electron microscopes (SEM). Through the development of novel systems/devices and nanorobotic manipulation techniques, we are in process of realizing a multi-functional ‘nano-factory’ for tackling a portfolio of problems, such as manipulation and characterization of individual nanomaterials; probing and characterization of nanoelectronic structures; manufacturing of nano-scaled devices; and manipulation of sub-cellular structures.



信興高等工程研究所

Shun Hing Institute of Advanced Engineering